THE UNIVERSITY OF HULL

FINE-SCALE MODELLING OF RAIN FIELDS FOR RADIO NETWORK SIMULATION

being a Thesis submitted for the Degree of

Doctor of Philosophy in Electronic Engineering

in the University of Hull

by

Xiaobei ZHANG

(MSc.)

(BEng. Beijing Institute of Technology)

July 10th, 2008

ACKNOWLEDGEMENTS

First I wish to express my gratitude to Dr. Kevin S. Paulson, my supervisor, for providing me the opportunity to do this project and directing me to find the right way to finish this work. Thank you for his inspiration, patience, encouragement and warmth. I am also grateful to my other supervisors, Dr. Sarah Callaghan, Mr. N. G. Riley and appreciate the support and help from the department. I consider myself fortunate to work in this friendly environment. I am grateful to the researchers at Chilbolton Observatory for acquiring much of the data this thesis is built on. Finally, I would like to express my sincere thanks to my parents for their encouragement during my study.

ABSTRACT

Electromagnetic waves at microwave frequencies are strongly scattered by rain. Rain fade is the mechanism that limits the performance of terrestrial microwave telecommunication systems. To predict the Quality of Service (QoS) at a node in heterogeneous networks of line-of-sight, terrestrial, microwave links; requires knowledge of the spatial and temporal statistics of rain over scales of a few meters to tens or hundreds of kilometres, and over temporal periods as short as one-second. Current internationally recognised models are not able to predict QoS, even for an individual link. This project aims to produce a radio network simulator that will predict the correct first and second order joint, rain fade statistics on heterogeneous networks of arbitrary geometry.

Meteorological radar databases provide rain rate maps over areas with a spatial resolution as fine as a few hundred meters and a sampling period of 2 to 15 minutes. Such two-dimensional, rain rate map time-series could be used to predict the QoS provided by arbitrary millimetre-wave radio networks, if the sampling period were considerably shorter i.e. of the order of 10 s or less. This work analyses the spatial and temporal rain rate variation by using data gathered as part of the Chilbolton Radar Interference Experiment (CRIE). Numerical algorithms have been developed to interpolate one, two and three dimensional (1D, 2D and 3D) rain rate fields to a finer sampling interval. A series of radar derived rain maps, with a 10 minute sample period, are interpolated to 10 seconds. Stochastic algorithms have been developed to preserve important statistics present in the CRIE data while introducing rain rates at new data points which preserve *a priori* statistics determined from other datasets. The resulting fine-scale spatial-temporal rain rate fields form the basis of a link simulation tool. The performance of several links is simulated and the simulation statistics are compared with international models and measured data.

CONTENTS

Acknowledgement i

Abstract ii

Contents iii

List of Figures and Tables I

Notation V

Glossary of Terms VIII

CHAPTER 1 INTRODUCTION 1

1.1 The General Network Rain Fade Simulator 2

1.2 Aims and Objectives of the Work 3

1.3 Report Outline 4

CHAPTER 2 RAIN EFFECTS ON MICROWAVE LINKS 6

2.1 Rain and Rain Attenuation Parameters 7

2.1.1 Raindrop Size Distribution 8

2.1.2 Rain Drop Shape and Canting Angles 11

2.2 Overview of Rain Field Parameters 13

2.2.1 Rain Rate Distribution 13

2.2.2 Rain Attenuation 15

2.2.3 The Specific Attenuation of Rain 17

2.2.4 The Number and Duration of Rain Fades 18

2.3 Summary 20

CHAPTER 3 RAIN MODELS FOR FADE PREDICTION 21

3.1 Rain Fade Models 21

3.1.1 Rec. ITU-R P.530 Model 23

3.1.2 Crane's Rain Attenuation Model 24

3.2 Second Order Statistics of Rain Fade 25

3.2.1 Spectral Model of Rain Fields 26

3.2.2 Rain Cell Models 30
3.3 Voss Algorithm 32
3.4 Time to Space Transformations of Rain Rate Statistics 33
3.5 Summary 33
CHAPTER 4 RAINFALL MEASUREMENTS 35
4.1 Rain Event Categorisation 35
4.2 Rain Gauges 36
4.3 RAL Rapid Response Drop-Counting Gauges 38
4.4 Weather Radar 39
4.5 Estimation of Rain Rate From Radar Data 41
4.6 The Chilbolton Advanced Weather Radar 43
4.7 The CRIE Database Description 44
4.8 Summary 47
CHAPTER 5 SPATIAL AND TEMPORAL RAIN RATE VARIATION 49
5.1 Introduction 49
5.1.1 Scales of Interest 49
5.1.2 Why Does Rain Rate Vary 50
5.1.3 Measurement of Horizontal Variation 51
5.1.4 Conclusions 51
5.2 Fractal and Rain Field Multi-fractal Analysis 52
5.3 Quantile Scaling and Existence of Moments 56
5.3.1 Existence of Temporal Moments 57
5.3.2 Calculation of Spatial Moments 59
5.3.3 Existence of Spatial Moments 61
5.3.4 Simple and Multi-Scaling 62
5.4 Multi-fractal Analysis 63
5.4.1 Spatial-Temporal Multi-fractal Analysis 63
5.4.2 Temporal Modeling 65
5.4.3 Temporal Analysis 66
5.4.4 Spatial Modeling 68

5.4.5 Spatial Analysis 69
5.5 Summary 73
CHAPTER 6 INTERPOLATION OF RAIN RATE FIELDS 75
6.1 Rain Rate Statistics 75
6.2 One-Dimensional Interpolation Scheme 76
6.3 Two-Dimensional Rain Rate Interpolation 78
6.3.1 Two-Dimensional Spatial-Temporal Interpolation 79
6.3.2 2D Interpolation Algorithm 80
6.3.3 Test of the 2D Algorithm on Brownian Data 81
6.3.4 Test of the 2D Algorithm on Radar Data 83
6.4 Three-Dimensional Interpolation of Radar Data 84
6.4.1 3D Interpolation Algorithm 86
6.4.2 Test 3D ARMD on Numerical Data 89
6.5 Summary 91
CHAPTER 7 DISAGGREGATION RAIN RATE FIELDS 92
7.1 Overview 92
7.2 Disaggregation Using Multiplicative Cascade 95
7.3 Summary 96
CHAPTER 8 DISAGGREGATION AND INTERPOLATION ON CRIE DATA 98
8.1 3D Intermittency and Censorship 98
8.1.1 Maximum Likelihood Estimation of the Marginal Distribution 99
8.1.2 Extrapolation into Low Rain Rate Regions 100
8.2 Advection 100
8.3 Disaggregation the CRIE Data 102
8.4 Disaggregation and Interpolation of Radar Data 105
8.5 Quantile function and Moment Scaling 107
8.5.1 Temporal Moment Scaling 107
8.5.2 Spatial Moment Scaling 108
8.6 Summary 110
CHAPTER 9 FADE MODELING 111

9.1 Fade Modeling Based on 2D Interpolation 111
9.1.1 Attenuation Statistics 112
9.1.2 Marginal Rain Rate Distribution 112
9.1.3 Marginal Rain Fade Distribution 112
9.1.4 Comparisons with Measured Real Link 114
9.1.5 Summary 118
9.2 Fade Modeling Based on 3D Interpolation 118
9.2.1 Attenuation Compared with Measured Real Link 119
9.2.2 Summary 122
CHAPTER 10 FADE DURATION STATISTICS 123
10.1 Average Fade Duration 124
10.2 Summary 127
CHAPTER 11 CONCLUSIONS AND FUTURE OUTLOOK 128
11.1 Summary of Conclusions 128
11.1.1 Rain Field Analysis 128
11.1.2 Downscaling of Rain Field 129
11.2 Recommendation for Further Work 131
11.2.1 Development of the Simulator 131
11.2.2 Automatic Transmit Power Control 133
11.2.3 Dynamic Modulation 134
11.2.4 Fade Durations 134
APPENDIX A 136
APPENDIX B 140
REFERENCES 143

List of Figures and Tables

Figure 2.1.1 Equal-volume raindrop models

Figure 2.2.1 Rainfall statistics from ITU-R Rec.837

Figure 2.2.2 The specific attenuation produced by 30mm/hr rain for frequencies across the millimetric range, for horizontally and vertically polarized radiation, as predicted by Rec. ITU-R P838-2

Figure 3.1.1 Brief rain attenuation prediction procedures (ITU-R)

Figure 5.3.1 Rain rate exceeded with probability $1-p$ for integration periods, from top to bottom, of 10 seconds, 1, 2, 3, 4, 5, 6 and 7 minutes

Figure 5.3.2 Accumulation of radar voxels to yield analysis voxels of similar size and shape

Figure 5.3.3 Rain rate exceeded with probability $1-p$ for spatial integration volumes

Figure 5.4.1 Moment scaling structure function for CRIE data and averaged 9 gauge-years rain gauge data (temporal modeling)

Figure 5.4.2 Moment scaling exponent as a function of moment order (temporal modeling)

Figure 5.4.3 Moment scaling structure function for CRIE data (spatial modeling)

Figure 5.4.4 Moment scaling structure function for CRIE data (spatial modeling, near radar area)

Figure 5.4.5 Moment scaling structure function for CRIE data (spatial modeling, far radar area)

Figure 5.4.6 The calculated moment scaling statistics of rain fields after interpolation onto a Cartesian grid (spatial modeling)

Figure 5.4.7 Moment scaling exponent as a function of moment order (calculated from the polar and Cartesian rain data) (spatial modeling)

Figure 6.2.1 Comparison of the percentage of time that abscissa rain rates are exceeded from the measured radar rain rate data and with 1D interpolated rain rate time-series and 9 gauge-years of rain rate data.

Figure 6.2.2 Average spectral density of log rain rate from interpolated radar rain rate compared with fractional Brownian $H = 1/3$ model (a power-law of –5/3)

Figure 6.2.3 Moment scaling structure function for interpolated CRIE data and averaged 9 gauge-years rain gauge data (temporal modeling)

Figure 6.3.1A An example of a 65 by 65 discrete fractional Brownian field with $H = 1/3$

Figure 6.3.1B The result of interpolation between the first and last columns

Figure 6.3.2A 2D spectral density of data illustrated in Fig 6.3.1 A

Figure 6.3.2B 2D spectral density of data illustrated in Fig 6.3.1 B

Figure 6.3.3 Comparison of the percentage of time that abscissa rain rates are exceeded from the measured and interpolated radar rain rate data

Figure 6.3.4A Averaged spectral density of spatial-temporal log rain rate

Figure 6.3.4B The spectral density as a function of spatial-temporal range assuming rotational symmetry compared to a power-law with exponent of -8/3

Figure 6.4.1 Relative positions of data points used for interpolation.

Figure 6.4.2A An example of one scan in a 65 by 65 by 65 array of synthetic log rain rate samples generated using the standard Voss's RMD algorithm

Figure 6.4.2B An example scan of an array formed by interpolation of the data on the top and bottom surface

Figure 6.4.3A Averaged spatial-temporal 2D spectral density of data illustrated in Fig 6.4.2A

Figure 6.4.3B Averaged spatial-temporal 2D spectral density of data illustrated in Fig 6.4.2B

Figure 6.4.4 Averaged radial spectral density of 3D log rain rate, averaged over several scans assuming rotational symmetry, compared with the fractional Brownian $H = 1/3$ model (a power-law of –11/3)

Figure8.2.1 Demonstration of 3D interpolation with advection removal

Figure 8.3.1 Comparison of measured spatial moment scaling exponents and best fit Deddia function.

Figure 8.3.2 Comparison of the percentage of time that abscissa rain rates are exceeded from the measured and disaggregated radar rain rate data
Figure 8.3.3 Spatial moment scaling structure function of measured radar data and disaggregated radar data
Figure 8.4.1 Comparison of the percentage of time that abscissa rain rates are exceeded from the measured radar rain rates (dot), the disaggregated rain rates (thick), the downscaled rain rates (solid) and 9 gauge years of gauge data (dash)
Figure 8.5.1 Simulated rain rates exceeded with probability $1-p$ for different integration periods
Figure 8.5.2 Moment scaling structure function for interpolated CRIE data and averaged 9 gauge-years rain gauge data (temporal modeling)
Figure 8.5.3 Simulated rain rates exceeded with probability $1-p$ for different spatial integration volumes
Figure 8.5.4 Moment scaling structure function for measured (dotted), disaggregated (dashed) and downscaled CRIE data (solid)
Figure 9.1.1 Figure 9.1.1 The one-minute radar rain rate exceedance distribution compared with the Rec. ITU-R P.837-5 prediction using $R_{0.01} = 30$ mm/hr
Figure 9.1.2 Examples of two terrestrial links superimposed on the PPI data
Figure 9.1.3 38 GHz attenuation statistics for 2 km and 10 km path lengths from radar simulation (solid) and ITU-R Rec. 530, using $R_{0.01} = 30$ mm/hr . Model confidence intervals are also plotted (dotted, dashed)
Figure 9.1.4 Measured, one-minute attenuation statistics for a 3 km, 38GHz link compared with predictions derived from 2D radar simulation and ITU-R Rec. P.530-12, using $R_{0.01} = 30$ mm/hr
Figure 9.1.5 Temporal autocovariance function for 1-minute accumulations of the measured real link attenuation (38 GHz, 3 km) compared to the result predicted by simulation
Figure 9.1.6 Ten-second attenuation statistics for a 5.5km, 38 GHz link compared with ITU-R Rec. P. 530-12 predicted one-minute statistics based on a 0.01%

exceeded rain rate of 30 mm/hr, and the prediction of the network simulator using a single scan line

Figure 9.1.7 Temporal autocovariance function for 10-second accumulations of the measured real link attenuation and 2D network simulation at the 5.5 km scales

Figure 9.2.1 Simulated attenuation statistics for 38 GHz links of length 1 km, 5 km and 10 km using CRIE data (dotted) and downscaled data (solid), compared with Rec. ITU-R P.530-12 using $R_{0.01} = 30$ mm/hr (dashed)

Figure 9.2.2 Measured 10-second, attenuation statistics for a 5.5 km, 38 GHz link (grey) compared with predictions derived from radar simulation (black) and ITU-R Rec. P.530-12, $R_{0.01} = 30$ mm/hr

Figure 9.2.3 Measured one-minute attenuation statistics for a 3 km, 38 GHz link (grey solid) compared with predictions derived from radar simulation (black solid) and ITU-R Rec. P.530-12

Figure 9.2.4 Temporal autocovariance function for 1-minute accumulations of the measured real, 38 GHz, 3 km link attenuation (dotted, dashed) and simulated radar attenuation (solid)

Figure 10.1.1 The RAL fade duration model predictions for a 38 GHz, 9 km link (solid) compared to the fade durations of a simulated link using downscaled radar data (dashed). The curves indicate number of events in an average year for attenuations of 8, 12, 16, 20, 24 and 28 dB, from top to bottom

Figure 10.1.2 The RAL fade duration model predictions for a 38 GHz, 5 km link (solid) compared to the fade durations of a simulated link using downscaled radar data (dashed). The curves indicate number of events in an average year for attenuations of 8, 12, 16, 20, 24 and 28 dB, from top to bottom

Figure 10.1.3 The RAL fade duration model predictions for a 38 GHz, 1 km link (solid) compared to the fade durations of a simulated link using downscaled radar data (dashed). The curves indicate number of events in an average year for attenuations of 8, 12, 16, 20, 24 and 28 dB, from top to bottom

Figure B.1 2D interpolation by using 16 points in the neighborhood of Y_i

Figure B.2 2D interpolation by using 16 points in the neighborhood of Y_i (with coefficients A, B and C)

Table 4.6.1 Basic Features of CAMRa (from www.chilbolton.rl.ac.uk)
Table 8.3.1 Results of the multi-fractal analysis on measured radar data set
Table B.1 Filter coefficients for 2D interpolation

Notation

A	Rain attenuation
A_e	Effective aperture of the antenna
A_{incell}	Rain attenuation across a rain-cell
A_p	Path attenuation exceeded for any time percentages
b/a	Ratio of major to minor rain drop axes (Axial ratio)
$B_L(\mathbf{x},\tau)$	Spatial-temporal second moment of log rain rate
C_{ext}	The total extinction cross section of the particle
C_λ	Stochastic scaling coefficient
d	Path length
D	Drop diameter
$D_m(A)$	The mean duration of the fades contributing to $T(A)$
E	Complex refractive index of the material of which the particles is composed
$E[*]$	The expected value
f	Spatial or temporal frequency
$f_\lambda^R(u)$	Probability density function
FN	Inverse normal CDF
$F_\lambda^R(r)$	Cumulative probability of rain rate R
G	Antenna gain
h	Pulse width
H	Hurst coefficient.
$i(x,y,t)$	Notional instantaneous rainfall intensity continuous in space and time
k and α	Frequency and polarization dependent coefficients
$L(\mathbf{x},t)$	Log rain rate over specified integration volume

$M_{\lambda}^{R}(q)$	qth moment of R_{λ}
n	Dimension of the rain field
N	The number of rain events per year
N_0	Drop concentration at $D = 0$
$N_{\tau}(A)$	Numbers of fades
$N(D)$	Drop size distribution
$N(R,\tau)$	The number of times in an average year when the point rain rate exceeded R for a period of at least τ
$N(\mu,\sigma^2)$	A Normal distribution with mean μ and variance σ^2
p	Probability
P	An integral measure of rainfall
$P(\bullet)$	Probability of
P_t	Transmitted power
$\overline{P_r}$	Average received power
q	Moment
$Q_{\lambda}^{R}(p)$	Quantile function of R_{λ}
r	Path reduction factor
R	Rain rate
$R_{0.01}$	Rain rate average of a period of 1 min and exceeded for 0.01 per cent of the time for the region of the link
R_{λ}	Rain rate process over integration volume with scale factor λ
$R_{\max}$	Maximal rain intensity within a rain cell
$R_{\min}$	Minimum rain rate defined by radar noise
$R(\mathbf{x},t)$	Rain rate over specified integration volume

$R(t)$	Rain rate field
$R(x)$	Rain rate at position x along the path
S	Smooth interpolation
$S_q(\lambda)$	qth order moment of rain rate averaged over volume of diameter λ
$S(\omega)$	Spectral density function
T	Rain gauge integration time
T_0	The longest integration time
$T(A)$	The total time for which an attenuation of A dB is exceeded
t_d	Rain event duration
$v(D)$	Terminal velocity of rain drop
$V(D)$	Fall speed of drops of diameter D
$V_H(t)$	Fractional Brownian motion
X	Homogeneous Gaussian random variable
Z_v	Radar reflectivity at vertical polarisation
Z_{DR}	Differential reflectivity
Z_H	Radar reflectivity at horizontal polarisation

$a_{i/j}, b_{i/j}, c_{i/j}, c_{\alpha/k}$ and $m_{\alpha/k}$

Coefficients in equations for polarization described in ITU-R P838-2

α , β , c	Scaling parameters
$\bar{*}$	Mean of
θ	Scattering angles
$\zeta(q)$	qth order scaling exponent

τ	Lag between random fields
γ	Power exponent
$\gamma_{0.01}$	Specific attenuation exceeded 0.01% of an average year
γ_R	Specific attenuation
Λ	Slope of the drop size distribution
λ	Dimensionless scale factor
σ^2	Variance of log rain rate
ς	Random variable being i.i.d. samples from a Gaussian distribution $\zeta \in N(0,\sigma^2)$
Δ_x, Δ_t	Spatial averaging diameter and temporal sampling interval
ε	Random noise process yielding Gaussian i.i.d. samples $\varepsilon \in N(0,\sigma_n^2)$
ε_Y	An i.i.d. standard Normal sample
w	Random variable

GLOSSARY OF TERMS

1D	-One Dimension
2D	- Two Dimension
3D	- Three Dimension
AF	- Adjustment Factor
AGC	- Automatic Gain Control
ARMD	- Asymmetric RMD
ATPC	- Adaptive Transmit Power Control
BER	-Bit Error Rate
CAMRa	- Chilbolton Advanced Meteorological Radar
CDF	-Cumulative Distribution Function
CRIE	- Chilbolton Radar Interference Experiment
dB	- Decibels
DM	- Dynamic Modulation
DSD	- Drop Size Distribution
FBf	- Fractional Brownian field
fBm	- fractional Brownian motion
FBn	- Fractional Brownian noise
FD	-Fade Duration
FFT	-Fast Fourier Transform
FIM	- Fredholm Integral Method
FIR	- Finite Impulse Response
FMT	- Fade Mitigation Techniques
GHz	- Giga Hertz
HYCELL	- Hybrid Cell Model
ITU	- International Telecommunication Union
LPF	-Low Pass Filter
LoS	- Line of Sight
M-PSK	-Multiple Phase Shift Keying

MSSF	- Moment Scaling Structure Function
PDF	- Probability Distribution Function
PPI	- Plan Position Indicator
QAM	-Quadrature Amplitude Modulation
QoS	- Quality of Service
RAL	- Rutherford Appleton laboratory
RHI	- Range Height Indicator
RMD	- Random Midpoint Displacement
SDF	- Spectral Density Function
SES	- Severely Errored Second
SES	- Spectrum Efficiency Scheme

CHAPTER 1 INTRODUCTION

Terrestrial, line-of-sight, microwave telecommunication links experience attenuation due to rain. At frequencies above 10 GHz this is the dominant fade mechanism and (with mechanical failure) is almost exclusively the cause of outage. Outage has a complex definition stemming from ITU-T recommendations G.826 (1999) and G.828 (2000) and the F recommendations that are derived from them (e.g. F.1491). Modern digital radio systems broadcast a bit stream divided into blocks e.g. a typical SDH STM-1 system might have 801 bits per block and transmit 192,000 blocks per second. If any bit within a block is transmitted incorrectly then the block is termed “errored”. A Severely Errored Second (SES) occurs in any second were 30% or more of the blocks were errored. An outage is defined as the period between the first of ten consecutive SES until the first of ten consecutive non-SES. Traditionally, links are specified to have an outage period caused by rain fading not exceeding some small percentage of an average year, usually 0.01% or 0.1% of time, and the rain fade margin is built into the link budget by estimating the rain attenuation exceeded for this time. Many models exist to calculate the fade margin e.g. COST210 (1991), COST235 (1996), Rec. ITU-R P.530-12 (2007) and Rec. ITU-R P.837-5 (2007). However, these models are based on available statistics of rain rate measured with a one-minute integration time. These models are adequate for fade-margin calculations for individual long links but probably under estimate the incidence of outage on links shorter than 1 km. They provide only limited guidance on the performance of networks e.g. Rec. ITU-R P.530-12 provides some guidance for more complex links such as multi-hop links and links utilising route diversity. Rec. ITU-R P.1410-2 (2003) also provides some guidance for point-to-multipoint cellular systems.

The Quality of Service (QoS) experienced by a node in a heterogeneous network of microwave links, at a minimum defined by the average annual outage, is currently impossible to predict as it depends upon joint time series of rain fade with a one-second integration time. The joint distribution of rain fade experience by links in an arbitrary network would be helpful in the estimation of QoS. However, currently no models exist to predict joint rain fade distribution. Rudimentary models of the duration of fades exist for individual links, but not for networks that are more complicated. The engineering of fade mitigation techniques such as route diversity or adaptive modulation, also require the knowledge of typical time-series of rain fade on heterogeneous networks of links.

The joint rain fade distribution is determined by the rain fields experienced by the link network and a large number of parameters describing network geometry and the communications system e.g. frequencies, antenna gain patterns, path elevation etc. these network and system parameters make the empirical determination of joint rain fade an intractable problem. However, if realistic rain rate field time-series are available, then joint rain fade can easily be calculated for arbitrary link networks. Currently no measured data set exists which spans the wide range of spatial and temporal scales necessary for general network simulation. For this reason, numerical methods to generate realistic rain field time-series would be of great interest and use to system designers, especially one that could be customised to mimic the behaviour of their climate region.

1.1 The General Network Rain Fade Simulator

The proposed General Network Rain Fade Simulator is based on three major operations:

1. Rain field generation;
2. Network simulation;
3. Analysis.

The rain field generation aims to produce a rain field time series that spans the network with sufficient resolution in both time and space to yield second by second rain fade time series on each of the network links. This is by far the most challenging component of the system. With these rain fields it is relatively straightforward to generate rain fade time series for each link by pseudo-integration of the derived specific attenuation field along the link paths. The final analysis operation extracts the required summary statistics from the joint rain fade time series. The detail of this operation depends upon the question being investigated.

As currently, no spatial-temporal rain rate dataset exists that spans the required range of scales, some synthetic enhancement of existing data is necessary. Meteorological radar data yields rain rate estimates over the large spatial scales necessary, and in some cases down to the fine scales necessary. However, to achieve fine spatial resolution, large radars are necessary and these, by their nature, are slow to physically scan and so yield relatively poor temporal sampling. One way to generate the rain fields necessary is to numerically augment rain fields measured by meteorological radar. If rain field data is available with the desired spatial sampling, then this amounts to numerically generating the rain fields that may have been measured between radar scans. This process requires *a priori* statistics to constrain the numerically generated rain fields.

1.2 Aims and Objectives of the Work

The aim of this project is to produce a radio network simulator that will predict the correct first and second order joint, rain fade statistics for heterogeneous networks of arbitrary geometry. An input to this simulator is a numerically generated, time-series of fine-scale rain fields. This time series will allow the simultaneous calculation of rain fade and rain scatter interference on links in an arbitrary radio network within the rain field. This fine-scale rain simulator should yield the correct statistics up to at least second order, and be valid over large ranges of spatial-temporal scales.

The major objectives of this project are:

1. To identify current challenges in microwave systems design and regulation

that cannot be addressed with existing rain fade models;

2. To identify the characteristics required of a new model to fully address these challenges;
3. To measure the statistical properties of spatial and temporal rain rate variation that impact on radio system engineering;
4. To design, build and test a system that generates rain rate field time-series with the necessary statistical properties;
5. To design, build and test a system to derived joint rain fade time-series from the rain field generator, for arbitrary networks of microwave links;
6. To apply the general network rain fade simulator to a current problem in radio engineering.

1.3 Report Outline

This thesis represents a review of research undertaken during three years of study. The aims and objectives of this report are described in the previous section. Chapter 2 expands on the background of the interaction between microwave links and rain. Chapter 3 looks at rain fade modeling including a critical analysis of existing ITU-R recommendations. This chapter continues looking at models of rain rate variation and considers their application to microwave system modeling.

Chapter 4 considers measurements of rain rate. The characteristics of measurement made by rain gauges and weather radars are examined. In particular, the Chilbolton Advanced Meteorological Radar (CAMRa) is described in detail, as data used in this project is derived from a two-year observation period (1987-1989) using this instrument.

Chapter 5 investigates the statistical properties of rain rate variation. The statistics important for predicting the performance of microwave systems are identified. In particular, the scaling properties of both spatial and temporal variation are defined and derived from rain gauge and CAMRa measurements.

In Chapters 6 to 8, methods are derived for the numerical interpolation of rain field time-series i.e. methods are developed to numerically generate the rain fields that may have been measured between those derived by meteorological radar measurements. The proposed methods are based on a disaggregation algorithm due to Deidda (2000) and a new interpolation algorithm loosely based on the Random Midpoint Displacement algorithm of Voss (1985) and the Local Average Subdivision algorithm of Fenton and Vanmarcke (1990). The interpolation method is described in Chapter 6 and the disaggregation method is presented in Chapter 7. In Chapter 8, the disaggregation and interpolation method is applied to measured data from CAMRa measurements.

In Chapter 9, the numerically generated fine-scale rain field time-series described in Chapter 6 and 8 has been used to simulate the time-series of rain fade on a range of 38 GHz links. The average annual, first and second order summary statistics have been generated and compared to ITU-R model predictions and some real link measurements.

Chapter 10 describes the General Network Rain Fade Simulator and uses the simulator to derive fade duration statistics for a range of links. These are compared to measured data and the ITU-R model.

Finally, Chapter 11 summarises the project and makes conclusions. Future areas of research based on the results of this project are proposed.

CHAPTER 2 RAIN EFFECTS ON MICROWAVE LINKS

Millimeter wave (30-300 GHz) links offer large bandwidth and hence high data-rates for integrated multimedia services. Such links are being developed as parts of new systems. They are quick to deploy, compared to cable and fiber connections. However, radio waves at high frequencies suffer high attenuation due to the rain. Raindrops are roughly the same size as the radio wavelengths at these frequencies and therefore have large scattering cross-sections; many raindrops have a diameter in the range 1 to 10 mm compared with a wavelength at 30 GHz of 10 mm. The effects of rain on radio wave propagation have been studied extensively for attenuation and depolarisation, both theoretically and experimentally.

Telecommunications engineers use average annual rain rate statistics to determine the fade margin necessary for a particular link to achieve the desired availability. Rain rate distributions can be estimated for any point on Earth from Rec. ITU-R P.837-5 (ITU-R, 2007). In particular, the one-minute averaged rain rate exceeded 0.01% of the time in an average year is an important parameter in rain fade models and the primary rain parameter used in the rain fade model e.g. Rec. ITU-R P.530-12 (ITU-R, 2007). The accurate estimation of this parameter requires ten years or more of rain data due to the large, natural year-to-year variation in rainfall. The estimation of the one-second rain rate exceeded 0.01% of the time would require considerably more data. Furthermore, it is debatable if this parameter is stable enough for measurement i.e. it may drift over the period necessary to estimate the average. The primary goal of a rain attenuation prediction method is to achieve acceptable estimates of the periods of attenuation incurred by the signal due to rain. Rec. ITU-R P.530-12 is a first point of reference for engineers designing terrestrial fixed links. However, the ITU only provides vague guidance on the joint performance of several links and on the duration of rain fades on a single link. Currently, the understanding of the spatial-temporal properties of the rain process is inadequate for the prediction of the performance of microwave systems.

To design a radio network simulator that will predict the correct first and second order joint, rain fade statistics for heterogeneous networks of arbitrary geometry, the fundamental concepts of radio wave propagation through rain and the parameters of rain fields will be reviewed in this chapter. The micro-physical elements, such as drop size distribution, drop shape and canting angles, which determine the rainfall rate and specific attenuation are defined and described.

2.1 Rain and Rain Attenuation Parameters

The effects of precipitation on radio-communications systems are dependent both on system parameters e.g. frequency and polarisation; network parameters e.g. geometry of links, length, elevation, network topology; and the type of precipitation parameters e.g. rain rate, drop size distribution etc. Rain attenuation is the dominant fade mechanism leading to outage at frequencies above 10 GHz. An increase in the rain incidence or intensity reduces the communication signal availability. Attenuation occurs due to absorption and scattering in rain. Models of fading due to rain have been derived from numerical implementation of scattering models or from empirical evidence from link monitoring exercises. These methods typically yield significantly different relationships between rain intensity and attenuation due to the difficulties that numerical methods have incorporating the variation of drop sizes, shapes and orientations. For linear polarisation, variation in the drop size distribution is the most important source of uncertainty. To understand variation in attenuation for different polarisations drop shape variation is important as well as drop orientation variation effects. The distribution of rain drop size contains a lot of information on the links between various rain parameters of interest including rain rate, radar reflectivity and microwave specific attenuation.

2.1.1 Raindrop Size Distribution

The rain drop size distribution (DSD), $N(D)$, describes the number density distribution function of raindrop sizes or reflects the volume distribution of the drop sizes i.e. $N(D)dD$ is the number of drops per unit volume in the diameter range D to $D+dD$. The DSD is linked to the rain rate by the drop fall-speed distribution. Many raindrop size distributions have been reported. The earliest paper on the size of raindrops was by Laws and Parsons, where the distribution is tabulated (J. O. Laws and D. A. Parsons, 1943). This distribution was used by Oguchi, Olsen and other researchers (T. Oguchi, 1960, 1964) (R. L. Olsen, D. V. Rogers and D. B. Hodge, 1978). Later, the exponential drop size distribution was empirically proposed by Marshall and Palmer (J. S. Marshall and W. McK. Palmer, 1948). The latter distribution is well accepted in the meteorological domain and in radar analysis. Later, a range of exponential forms linked to event type was proposed by Joss and Waldvogel (J. Joss, J. C. Thomas and A. Waldvogel, 1967). In this form, rain was divided into three types: drizzle (J-D), widespread (J-W), and thunderstorm (J-T). With the advent of instruments to measure DSD, concerns were raised as to the description of both the numbers of small drops and the large drop tail of the distribution. The gamma distribution was proposed as a raindrop size distribution by Ulbrich and Atlas (D. Atlas and C. W. Ulbrich, 1974). The exponential distribution is a special case of the gamma distribution. The third parameter allows the gamma distribution to describe cases with a large number or small number of small drops. The choice of the drop size distribution is crucial and affects the resultant specific attenuation.

The moments of the DSD yield different parameters of interest. Define the *n*th moment of the DSD to be:

$$M_n = k\int_0^\infty D^n N(D)dD \qquad (2.1.1)$$

Some moments of particular interest include:

$n = 0$ the total number of drops

$n = 3$ water volume per unit atmosphere volume

$n = 6$ radar reflectivity and specific attenuation

where k is a constant whose value depends on the units of measurement of the parameters.

The drop size and corresponding fall speeds, $v(D)$ gives the intensity of rainfall at any instant.

$$R = k\int_0^\infty D^3 N(D) v(D) dD \tag{2.1.2}$$

Marshall-Palmer Distribution and Laws-Parsons Distribution

In the case of Marshall-Palmer Distribution, the drop size distribution function $N(D)$ uses an exponential form (J. S. Marshall and W. McK. Palmer, 1945):

$$N(D) = N_0 \exp(-\Lambda D) \tag{2.1.3}$$

where N_0 is a parameter found to be around $8000\, mm^{-1} m^{-3}$ at the notional drop size of $D = 0$, and the value of $\Lambda\,(mm^{-1})$ is given by:

$$\Lambda = 4.1 R^{-0.21}, \tag{2.1.4}$$

where R is the rainfall rate in mm/hr.

DSD varies rapidly in time and space. However, it is generally assumed that DSDs become exponential when the sample volume is sufficiently large. Due to the large sample volumes defined by the first Fresnel zone of microwave links, the Marshall-Palmer distribution is generally satisfactory for statistical prediction of attenuation in the range of 10 GHz to 30 GHz, and recently up to 300 GHz (L. Barclay, 2003).

The Laws-Parsons Distribution is similar to the Marshall-Palmer form except that it has slightly fewer small drops. It is an empirically measured form for $N(D)$ that is tabulated numerically rather than expressed mathematically (J. O. Laws and D. A. Parsons, 1943).

Their study showed that N_0 could vary quite considerably even in one rain event and the shape of the distribution could also vary significantly. Thus a more suitable distribution function was required.

Gamma-type Distribution

A more general form of distribution is the gamma-type distribution, which can adequately describe many of the natural variations in the shape of the raindrop size distribution, in the following form (C.W. Ulbrich, 1983):

$$N(D) = N_0 D^m e^{-(3.67+m)^{D/D_0}} \tag{2.1.5}$$

It can be seen from this equation that compared with the exponential distribution, obtained when $m = 0$, the positive values of m reduce the numbers of drops at both the large and small ends of the size spectrum while negative values of m increase the numbers of drops at each end of the spectrum (L. Barclay, 2003).

It is generally believed that there is no single model for drop-size distributions at present which is accepted as representing physical reality, even as a statistical mean over many rain events. However, for particular modelling purposes, it is not essential that the assumed distribution represents physical truth at all drop sizes (L. Barclay, 2003).

Observations of radar reflectivity and microwave specific attenuation are very sensitive to the presence of large drops due to their dependence on the sixth moment of the DSD. Radar measurements suggest the presence of fewer very large drops than in an exponential distribution and measurements are well fitted using a gamma distribution with m between 3 and 5. This model incidentally lowers the assumed density of small drops, smaller than 1mm in diameter (L. Barclay, 2003). Other measurements of attenuation at 30 GHz to 300 GHz are more sensitive to small drops and make no strong implication about the presumed cut-off point for large drops, although work in the UK has suggested that a lognormal form of distribution would be appropriate for millimetric attenuation prediction (B. N. Harden, J. R. Norbury and W. J. K. White, 1978).

2.1.2 Rain Drop Shape and Canting Angles

Surface tension tends to make small rain drops spherical. However, drag from the air passing around a falling drop tends to distort the shape away from spherical. Rain drops in free fall are not spheroids, but are approximately oblate spheroids with a flattened base. As the drop diameter increases above 4 mm, the base becomes concave. This vertical-horizontal asymmetry leads to differential attenuation and phase shift of polarised radio waves propagating through a rain filled atmosphere (L. Barclay, 2003).

In scattering calculations, it is usual to model the rain shape as simple oblated spheroids, with the axis ratio b/a, where b and a are the semi-minor and the semi-major axis lengths respectively. A simple model for the axis ratio r based on the linear fit to wind tunnel data is given as (H. R. Pruppacher and K. V. Beard, 1970):

$$r = 1.03 - 0.062D\,; \quad 1 \le D \le 9\ \mathrm{mm} \tag{2.1.6}$$

The Pruppacher-and-Pitter model (P-P) is more realistic than oblated spheroids and well accepted by researchers for the calculation of microwave attenuation by rain.

The raindrop starts almost spherical, then becomes spheroidal and axisymmetric for midsize raindrops, and finally becomes distorted and non-axisymmetric (but still rotationally symmetric). This leads to the use of the P-P model in heavy rain climates due to the increased presence of larger raindrops. An equation was established by Pruppacher and Pitter to describe the shape of water drops falling at their terminal velocity in terms of the balance of the internal and external pressure at the surfaces of the drops (T. Oguchi, 1977 and 1981).

Figure 2.1.1 shows the raindrop of spherical, spheroidal and the Pruppacher-and-Pitter. All of these three models have the same volume.

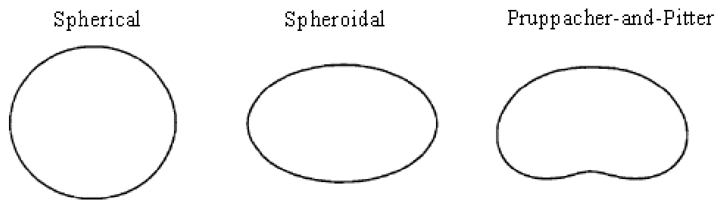

Figure 2.1.1 Equal-volume raindrop models

When the rain drop axis of symmetry is not vertical, the drop is said to be canting. When strong vertical wind shears are present, the population of drops will exhibit a similar canting angle. The effect on propagation is some transfer of energy between horizontally and vertically polarised waves. It is suggested from cross-polar measurements that a drop falls so that its symmetry axis is parallel to the velocity of air flow relative to the drop. Calculations show that terrestrial links within about 40 m of the ground could see canting angles up to about 5^0 (G. Brussaard, 1976).

At low frequencies, attenuation and phase shift will be greater for horizontal polarisation as drops are wider than they are tall. It is important to note that, although differential attenuation and phase below 18 GHz increases with frequency for a given rain event, they decrease for a given fade depth. This is partly because less deformed smaller drops make a greater relative contribution to the total attenuation as frequency is raised (L. Barclay, 2003).

2.2 Overview of Rain Field Parameters

2.2.1 Rain Rate Distribution

The starting point for estimating rain attenuation is the knowledge of the statistics of rainfall rate. The rainfall rate is one of key factors used to determine the amount of rain attenuation likely to be suffered in the propagation of wireless communications.

Link rain attenuation distributions are generally derived from point rain rate statistics. Direct measurements of rain attenuation are performed to test these models but tend not to be used directly due to the large number of link parameters, for example, frequency, polarisation, length elevation etc. It is generally accepted that at least five years of link rain fade data is needed to accurately estimate the 0.01% exceeded level. Attenuations that occur with lower probabilities require much longer monitoring times. The preferred option, and that sanctioned by the ITU, is to use locally derived statistics of rainfall rate with an integration time of 1 minute.

The fundamental distribution is the rain rate exceeded for a given percentage of an average year. The parameter $R_{0.01}$ is the notional point rain rate averaged over a period of 1 min and exceeded for 0.01 per cent of an average year in the region of the link. Rec. ITU-R P.837-5 provides annual statistics for the whole world, as a function of latitude and longitude, derived from numerical weather models.

Figure 2.2.1 plots the rain exceedance distribution for Chilbolton from ITU-R Rec. 837-5. According to the ITU-R world climate zones from the, now redundant, Rec. ITU-R P. 837-4, Climate F is the appropriate rain climate for Chilbolton. This yields a $R_{0.01} = 28$ mm/hr compared to measured values around 30 mm/hr.

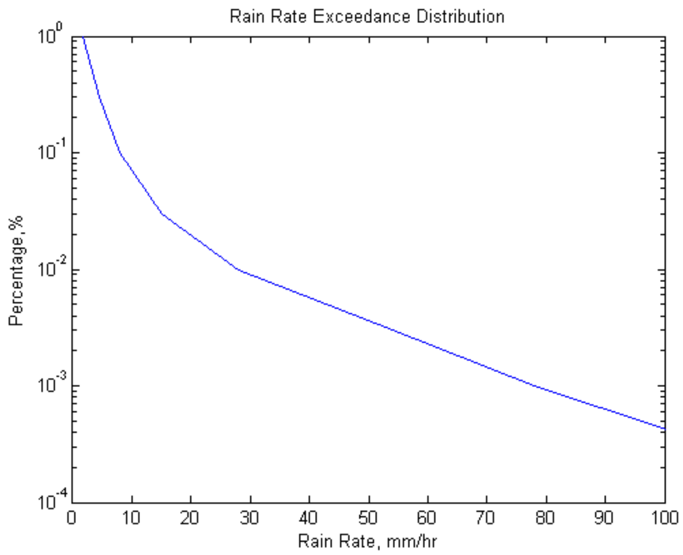

Figure 2.2.1 Rainfall statistics from ITU-R Rec.837

There are two methods to calculate the rainfall rate distribution experienced by a region. The empirical method is to use field measurements and recordings made over long time periods. Another way is to depend on models that have been developed, such as Rec. ITU-R 837 model and the Global Crane model (both derived from Numerical Weather Prediction simulations).

Both methods have their detractors. In general it can be said that there are significant differences between the results of the field measurements and several well-known models. Uncertainty stems from variations from year-to-year and location-to-location (W. Myers, 1999), from systematic errors in numerical weather models, and from variation at scales below the model resolution.

Research (Landsberg, 1981 and Jensen, 2000) suggests that the particular combination of effects such as sea breezes, topography and the urban heat islands has an influence on the initiation and development of rain storms. Urban surfaces are frequently made of glass, metal, asphalt, concrete, or stone. The reflection and absorption abilities of these surfaces exceed most natural surfaces resulting in higher day and night time temperatures than surrounding rural landscapes. In addition to horizontal surfaces, many cities have large vertical surfaces of different geometric shapes. These vertical surfaces function like canyons affecting radiation and wind patterns. The high consumption of fossil fuels in cities for heating and cooling of buildings and running of automobiles results in more heat being released than being received (Jensen, 2000). Furthermore, the high concentration of air particulates such as dust, pollutants, gases, and aerosols over a city creates a greenhouse condition where a heavy blanket of particulates absorbs the long-wave radiation coming from the city and reradiates it back down on the city. These blankets are called "dust domes" and every major city has such a dome. More water vapour forms around the increased particulates within these domes leading to more cloud cover over a city and the potential for increased precipitation (Landsberg, 1981 and Jensen, 2000).

2.2.2 Rain Attenuation

Rain attenuation (in dB) is defined as the reduction of the received signal power due to the rain as compared to the received signal power under clear weather conditions.

Rain attenuation is a function of many random time-varying parameters of the medium. These parameters include the number of rain drops in the path, the raindrop shapes, raindrop water temperature, the drop size distribution, the spatial variation of rain parameters, and indirect parameters such as wind velocity, the presence of up or down drafts, and other effects (S. Lin, 1973).

Although rain attenuation can be ignored at frequencies below about 5 GHz, it must be included in design calculations at higher frequencies, where its importance increases rapidly with frequency up to 100 GHz.

The total attenuation A along a very short path of length L experiencing rain may be calculated as the sum of the contributions of each individual drop and can be computed from:

$$A = 4.34L\int_0^\infty C_{ext}N(D)dD \tag{2.2.1}$$

where C_{ext} is the total extinction cross section of the particle and is given by:

$$C_{ext} = \lambda^2 / \pi \operatorname{Re}[S(0)] \tag{2.2.2}$$

where $S(\theta)$ is a dimensionless function of the scattering angles θ and $S(0)$ is the forward scatter cross-section (Hulst, 1981). The attenuation in dB per unit length of propagation path is known as the specific attenuation:

$$\gamma = \lim_{L \to 0} 10\log(A)/L \quad \text{dB/km.} \tag{2.2.3}$$

The total attenuation experienced by a propagation path is the path integral of the specific attenuation:

$$A = \int_0^L \gamma(\ell)d\ell \quad \text{dB} \tag{2.2.4}$$

However, it is very unusual for the specific attenuation to be known along the length of the path. Usually, the historical point rain rate distribution for the region is known and this may be transformed into the point specific attenuation distribution. However, the transformation of the point specific attenuation distribution to path integrated distribution is not trivial. ITU-R models allow for the spatial variation of rain intensity by introducing a factor to reduce the effective path length. This scaling factor r, depends on path length and rain rate (or time percentage), and is known as path reduction factor. According to ITU-R Rec. P.530-12,

$$r = 1/(1 + d / d_0), \tag{2.2.5}$$

where $d_0 = 35e^{-0.015R_{0.01}}$, $R_{0.01}$ is the rainfall rate with an integration time of 1 min that occurs for 0.01% time and d is the path length. Due to the relationship between the attenuation and the rain rate, the effective path length is simpler to estimate with the precipitation rate as a parameter. The path reduction factor is usually estimated using data bases of meteorological radar data. However, it is a simplistic fix that is only valid for average annual statistics (of rain fade and specific attenuation derived from point rain rates) made with specific integration volumes.

2.2.3 The Specific Attenuation of Rain

The Beer-Lambert-Bouguer law is a description of the exponential decline in intensity of a wave as it passes through a scattering medium. The exponential constant linking the rate of decline to the amount of scattering caused by the medium is known, at radio frequencies, as the specific attenuation. For an atmosphere containing rain, it is related to the number, sizes, shapes and refractive index (linked to temperature) of rain drops. In radio systems engineering it is usual to assume a power law linking rain rate to specific attenuation.

The internationally recognised model is provided by Rec. ITU-R P838-2 (ITU-R, 2003). Specific attenuation γ_R (dB/km) is obtained from the rain rate R (mm/hr) using the power-law relationship: $\gamma_R = kR^{\alpha}$; where k and α are frequency and polarisation dependent coefficients. They may be determined by the following equations. $a_{i/j}, b_{i/j}, c_{i/j}, c_{\alpha/k}$ and $m_{\alpha/k}$ are coefficients and are given by ITU-R P838-2.

$$\log k = \sum_{j=1}^{3}\left(a_j \exp\left[-\left(\frac{\log f - b_j}{c_j} \right)^2 \right] \right) + m_k \log f + c_k \tag{2.2.6}$$

$$\alpha = \sum_{i=1}^{4}\left(a_i \exp\left[-\left(\frac{\log f - b_i}{c_i} \right)^2 \right] \right) + m_\alpha \log f + c_\alpha \tag{2.2.7}$$

A plot for the specific attenuation produced by 30 mm/hr rain for frequencies across the millimetric range is illustrated in figure 2.2.2.

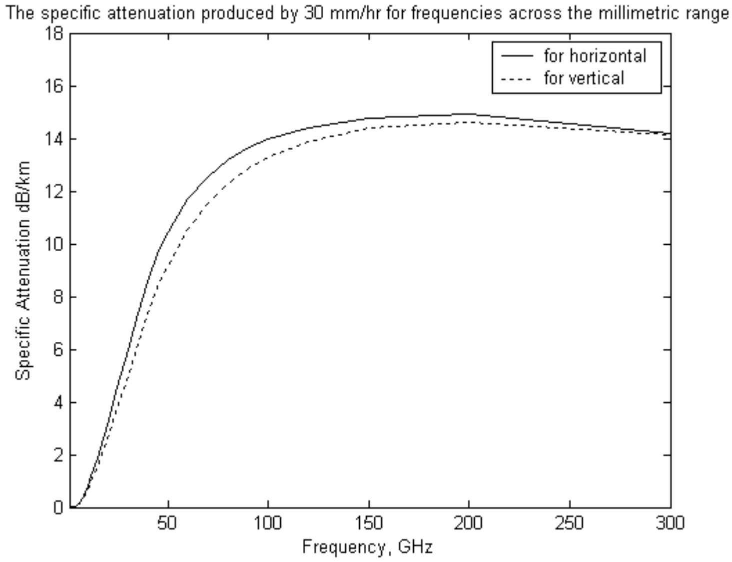

Figure 2.2.2 The specific attenuation produced by 30 mm/hr rain for frequencies across the millimetric range, for horizontally and vertically polarised radiation, as predicted by Rec. ITU-R P838-2

2.2.4 The Number and Duration of Rain Fades

Duration distributions describe the number (or proportion) of events in an average year where rain rate or rain fade exceed some threshold, in mm/hr or dB respectively, for some duration τ or longer i.e. $N(R,\tau)$ would be the number of times in an average year when the point rain rate exceeded R for a period of at least τ. The link between the rain and rain fade duration distributions is complicated and depends upon the specific attenuation – rain rate relationship and the spatial-temporal statistics of rain fields. If $T(A)$ is the total time for which an attenuation of A dB is exceeded and $D_m(A)$ is the mean duration of the fades contributing to this total time then: $D_m(A) = T(A)/N_\tau(A)$, where $N_\tau(A)$ is the number of fade. A large number of different forms have been suggested as good fits to empirically measured rain rate and rain fade duration curves. These include power-laws (Rec. ITU-R 838-2, 2003), log-Normal (S. H. Lin, 1973; B. J. Easterbrook and D. Turner, 1967; D. J. W. Turner and D. Turner, 1970; Gibbins and Paulson, 2000) and Weibull (Paulson, 2000).

The Rutherford Appleton Laboratory (RAL) database of rainfall rate measurements has been used to develop a model to describe the number of events of given durations with rainfall rates of specified thresholds. The database comprises rain rate measurements made over a three-year period using three rapid-response rain gauges of the drop-counting type, spaced 200 m apart. The measurements were made at Chilbolton, in Hampshire (ITU-R rain zone F), and the rain rates were sampled at 10 second intervals. The durations of events with rain rates exceeding levels between 5 mm/hr and 50 mm/hr were determined, with a minimum duration of 30 seconds, i.e. three consecutive samples with rain rates greater than the given threshold. For the data considered, a lognormal model curve was fitted to the CDF of durations:

$$N = 1.70 \cdot 10^4 R^{-1.76} \exp\left\{-\frac{(\ln t_d - 2)^2}{3.86 - 0.0409R}\right\} \tag{2.2.8}$$

The RAL rain duration distribution was then used to develop a rain fade distribution model. This involves two transformations. The threshold rain-fade was transformed into an equivalent rain rate. This has been achieved using the Rec. ITU-R 530 attenuation-rain rate relationship i.e. $A = \gamma(R)Lr(R)$, see Section 2.2.2; where both the specific attenuation and path reduction factor depend upon the rain rate R. This expression cannot be explicitly inverted for R and so needs to be solved numerically. Secondly, the duration of rain at a point needs to be transformed into an equivalent duration of a fade on a link. Typically, a rain event will cause a longer fade on a spatially extended link than the equivalent rain rate will be exceeded at a point. Therefore a dilated duration is needed and an empirical result was derived. After these transformations the fade duration model of equation 2.2.9 was derived. Here, N_A is the number of fades exceeding a depth of A dB and a duration of t_d seconds in an average year.

$$N_A = 1.7 \cdot 10^4 R_A^{-1.76} \exp\{-\frac{[\ln(273R_A^{0.39} + (0.166 + 0.0194R_A)t_d) - 2]^2}{3.86 - 0.0409R_A}\} \tag{2.2.9}$$

2.3 Summary

The rain attenuation experienced by a microwave link is determined by all the rain drops in the beam, often interpreted as the first Fresnel zone. Many assumptions are required to reduce the problem of predicting rain fade statistics to a tractable form. One of the most important parameters is the drop size distribution (DSD). Many of the important properties of rain can be derived from, or related, by the DSD e.g. rain rate, radar reflectivity and microwave specific attenuation. Typically DSDs vary within rain events and between rain events. This leads to some uncertainty in relationships between rain rate and scattering or attenuation parameters. Other rain parameters play a smaller but still significant role e.g. drop canting leads to cross-polar interference. Drop shape, temperature and amount of oscillation all have a small effect on the scattering characteristics of drops. To some extent, link attenuation averages out the spatial variation of all these rain parameters and in many cases it is justified to use mean values.

CHAPTER 3 RAIN MODELS FOR FADE PREDICTION

3.1 Rain Fade Models

Models of rain fade experienced by microwave links vary as to the ambitions of their outputs. The simplest aim is to produce distributions of rain fades, typically over a notional average year. A refinement of these yields monthly distributions or estimates of the worst-month performance. These models are primarily aimed at spectrum regulation and fade margin calculations. Databases of meteorological radar images may be transformed into specific attenuation fields and used to produce joint rain fade snap-shots for any terrestrial link network. From these, joint rain fade distributions can be calculated. Other models, generally based around simulations, yield time series of rain fade for one or more links. These models have much wider application but currently yield unrealistic join statistics due to the use of simplistic rain fields (L. Feral, J. Lemorton, L. Castanet and H. Sauvageot, 2003).

In general, rain attenuation models fall into two categories. The first category derives rain fade from measured or modelled rain fields while the second is empirically derived from fade measurements on many links at many locations. Empirical procedures have been most common but both methods are severely limited by lack of data.

There are two empirical rain fade models widely used in microwave system design. One is the Rec. ITU-R P.530-12, which is considered the standard in predicting the path attenuation, based on the Rec. ITU-R P.837-5 $R_{0.01}$ climate maps (or local measurements if available) and the Rec. ITU-R P.838-2 parameters for the specific attenuation. The second is the Crane attenuation prediction model (particularly of interest in North-America), based on the Crane climate model. This section briefly addresses some of the most important rain attenuation models presented by Crane and the ITU-R.

The ITU has recommended a calculation method for terrestrial systems, Rec. ITU-R P.530-12, and for space to earth links, Rec. ITU-R P.618-7. These models take into account a path-length reduction factor to account for the spatial variation of rain.

The attenuation exceeded for 0.01% of an average year is estimated from the specific attenuation exceeded for the same time percentage: $\gamma_{0.01}$. This is estimated from the 0.01% exceeded rain rate $R_{0.01}$ using the ITU-R P.838-2 (ITU-R, 2001) power law. The specific attenuation is scaled by the path length, L, to yield the attenuation that would result from uniform rain of this intensity along the path. However, for the high rain rates exceeded for small percentages of time, it is far more common for only a portion of the path to be spanned by the heavy rain event and so the attenuation $L\gamma_{0.01}$ overestimates the 0.01% exceeded attenuation. This overestimation is larger for longer links and for smaller time percentages. The over-estimation is rectified by a path-length reduction factor, r, yielding an expression for the 0.01% exceeded rain attenuation: $A_{0.01} = Lr\gamma_{0.01}$. Many forms for the path reduction factor have been proposed and used.

For the prediction of rain fade attenuation using the Rec. ITU P.530 standard, rain rate at the 0.01% exceeded level for the location of interest is required, frequency, path length and attenuation factors from Rec. ITU-R P.838-2 (ITU-R, 2001). Other percentages are calculated by using the 0.01% value.

The Crane models have been used for both space-earth and terrestrial links. There are three versions of Crane models. They are Global Crane model (developed in 1980), Two-Component model (developed in 1982) and Revised Two-Component model (developed in 1989). It can be said that in most cases the Crane models predict higher rain attenuation than the ITU model (W. Myers, 1999).

3.1.1 Rec. ITU-R P.530 Model

Rec. ITU-R P.530-12 presents a method for predicting the long-term statistics of rain attenuation. Prediction method is constructed with the rain rate as the primary parameter. There are several steps involved it (ITU-R, 2001).

Figure 3.1.1 shows overview rain attenuation prediction procedures based on method provided by Rec. ITU-R P.530-12.

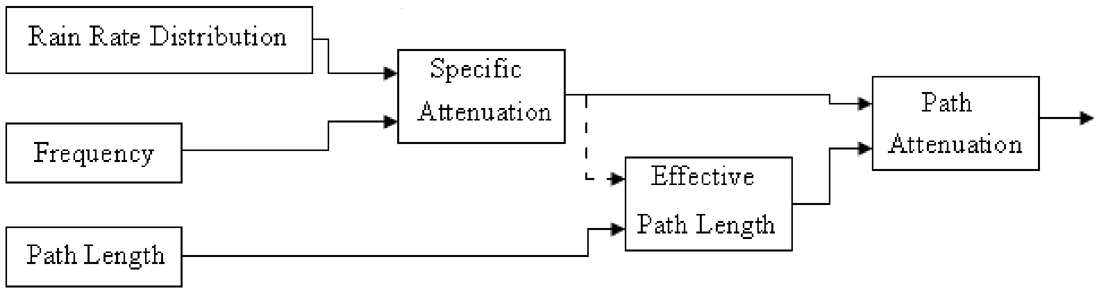

Figure 3.1.1 Overview of rain attenuation prediction procedures (ITU-R)

In the first place, if rain rate $R_{0.01}$ could not be obtained from long-term measurements carried out in the location of the link, an estimate can be obtained from rain rate maps given in Rec. ITU-R P.837-5.

Secondly, the effective path length is required to be calculated. The effective length is less than the actual path radio waves propagate in the link and reduces with increasing of value of rain rate $R_{0.01}$. The non-uniformity of the rain rate, particularly for rain rate above 20 mm/hr, along the radio path is taken into consideration in this step.

Thirdly, for a given rain rate $R_{0.01}$, an estimate of the path attenuation exceeded for 0.01 per cent of the time is calculated by multiplying the effective path length by the rain-specific attenuation. According to Rec. ITU-R P.838-2, the rain-attenuation in dB/km is a function of frequency, polarisation and rain rate.

In addition, two formulae are given for deriving the path attenuation exceeded for percentage times in the range 1 to 0.001 per cent from the 0.01 per cent value. One applies to links between 30^0 north and 30^0 south and the other applies to links outside this region.

Finally, rain attenuation statistics for an average worst month, which is often required in system planning, can be calculated from the average annual statistics using methods given in Rec. ITU-R P.841-1.

At frequencies where both rain attenuation and multi-path fading must be taken into account, the exceedance percentages for a given fade depth corresponding to each of these mechanisms can be added.

3.1.2 Crane's Rain Attenuation Model

Crane's rain attenuation model takes into account the variation of rain rates along a horizontal path. A path-averaged rain rate is calculated based on the point rain rate. The average rain rate is related to the point rain rate by (R. K. Crane, 1996):

$$\overline{R} = f_1(d)R^{1+f_2(d)} \tag{3.1.1}$$

where d is the path length, and $f_1(d)$ and $f_2(d)$ are empirically derived functions.

A theoretical prediction model was proposed by Crane. This model is summarised in the following equations.

$$A = aR^b\left[\frac{e^{ubd}-1}{ub}\right] \qquad (\text{for } 0 \le d \le D_0) \tag{3.1.2}$$

$$A = aR^b\left[\frac{e^{ubD_0}-1}{ub} - \frac{B^b e^{cb} D_0}{cb} + \frac{B^b e^{cbd}}{cb}\right] \qquad (\text{for } D_0 \le d \le 22.5 \text{ km}) \tag{3.1.3}$$

where

$$D_0 = 3.8 - 0.6\ln(R)\,[\text{km}] \tag{3.1.4}$$

$$B = 2.3R^{-0.17} \tag{3.1.5}$$

$$c = 0.026 - 0.03\ln(R) \tag{3.1.6}$$

$$u = \ln[Be^{cD_0}]/D_0 \tag{3.1.7}$$

and A is the rain attenuation in dB, R is point rain rate in mm/hr, and d is path distance in km. Multipliers a and b are rain attenuation coefficients, which are functions of frequency and polarisation. All the parameters are well tabulated for different global rain climate zones. The global geographic regions are divided into rain climate zones based on the rain rate statistics collected over several years. Point rain rate vs. time distribution has been tabulated for each rain climate region (R. K. Crane, 1996).

3.2 Second Order Statistics of Rain Fade

Currently, the ITU-R provides Rec. ITU-R P.837-5 for calculating the average annual, one-minute averaged, rain rate distribution for any point on earth. This may be used to calculate the average annual rain-fade distribution experienced by a terrestrial link. However, telecommunications operators are increasingly interested in the second order statistics of rain-fade i.e. statistics that depend upon pairs of attenuations experienced at different times or/and on different links. Such statistics include the temporal power spectrum, rain-fade duration statistics, rain-fade slope statistics and rain-fade covariance for pairs of links, or the same link at different times. These statistics are important for the design of fading countermeasures, such as time/path diversity, and for interference coordination. The second order statistics of rain-fade depend directly upon the second order statistics of rain rate variation.

3.2.1 Spectral Model of Rain Fields

The tradition of the mathematical modeling of spatial-temporal rainfall fields is quite long among the hydrologists but for radio propagation applications this is an emerging area of study (R. Deidda, 2000). Rain models for radio simulation need to be spatial-temporal as radio links have spatial extent and temporal statistics of attenuation are desired.

Rain fade time-series generators or channel models can be used to simulate the channel conditions in scenarios where adaptive fade countermeasures are employed and can be used to optimise and predict the benefits of fade countermeasures. Countermeasures can be tested in a wide range of conditions and for a range of link parameters, much faster and more economically than testing using real links.

The development of time series was initiated in the nineties by many teams working on propagation channels for satellite mobile systems at L and S bands. Channel models for fixed satellite systems at Ka band and above, are a more recent interest and are linked to the development of Fade Mitigation Techniques (COST 280, 2002).

The stochastic dynamic variations of rain fields can be modeled using pulse models, Markov chains or power spectral density models. These models are able to reproduce the first and second order statistics for a site and are useful as inputs to evaluate channel models and fade mitigation design for radio links.

Although there is a large number of pulse models describing rain rate variation, including the model by Capsoni *et al* (1987) designed for propagation studies, these models do not contain information on the high resolution stochastic variation of rain rate in time and space. The Synthetic Storm model of Matricciani (1996) does provide high resolution, temporal, rain fade variation but relies on transformation of rain rate time series measured by gauge using a Frozen Storm model, see Section 3.4 and 5.4.

It is not clear if the method is applicable to links orientated at an angle to the rain advection and so derived average annual results are suspect. Veneziano *et al* (1996) have postulated that log rain rate, while raining, may be modeled as a stationary, Gaussian stochastic process. Furthermore, theoretical models of rain as a passive tracer in a turbulent, two-dimensional flow, Kraichnan and Montgomery (1980) and Lovejoy and Schertzer (1995), predict that the temporal and spatial spectral density of log rain rate follows a segmented power-law form. These fluid dynamical models often lead to spectral density power-laws with exponents expressed as ratios of small integers (Paulson, 2002). Over ranges of scales where the spectral density follows a simple power-law, there is no special scale and the random variable exhibits self-similarity. Models of rain rate variation that assume power-law spectra are often termed "fractal models". Crane and Horng-Chung Shieh (1989) identify one-dimensional (1D) spatial log rain rate spectra with two power-law segments. Below the scale of energy injection, typically the size of a front, the power spectrum has the form $|f|^{-3}$, where f is spatial or temporal frequency, reflecting a direct entropy cascade towards larger wave numbers. Above the scale of energy injection an inverse energy cascade towards smaller wave numbers leads to spectra of the form $|f|^{-5/3}$. Based on the observation of eight storms, Veneziano *et al* suggest that spatial or temporal 1D log rain rate has a spectral density function with four power-law segments. The corner frequencies are associated with the scale of convective cells and cell clusters. A log-log plot of such a spectral density is segmented-linear with the gradient of each segment equal to the power-law exponent (Paulson, 2002).

Two-dimensional Fourier analysis of rain rate or log rain rate fields is quite common in the literature. Studies published include those by Olsson *et al* (1993), Tessier *et al* (1993), Marsan *et al* (1996), Harris *et al* (1996) and Purdy *et al* (2001). The actual values for the power spectral density varied from study to study (Callaghan, 2005). To some extent this variation is to be expected. The low frequency components are determined by the shape of the rain field and so events with strong linear structure, such as frontal rain and squall-lines, have highly asymmetric spectra. The analysis of log rain rate is further complicated by areas with no rain where the log is undetermined. Different investigators have set these areas to arbitrarily low rain rates or have tried to choose areas where every point is experiencing rain. Both these choices limit the validity of the spectra and make averaging across events more difficult.

Paulson (2002) has proposed a spectral model of spatial-temporal rain rate variation when raining. It is based on the assumption that log rain rate is an isotropic, homogeneous, Gaussian random field with a spectral density function following a specific power law. The log rain rate spectral density model when raining is given by:

$$S_X(\omega) = K\left(1 + \frac{|\omega|^2}{\omega_0^2}\right)^{-0.5(\frac{5}{3}+n)} \tag{3.2.1}$$

where ω is a vector of the n dimensional coordinates, $\omega_0 \approx 0.01$ km^{-1} and K is a normalising constant to ensure that $\sigma_x^2 = \int_{-\infty}^{\infty} S(\omega) d\omega$. $X(t)$ is the log rain rate random field, where t is a vector that denotes a combination of time and space units (x, y, t). Since X is a homogeneous Gaussian random variable, its mean and variance can be given by:

$$m(t) \equiv E[X(t)] = \mu_x \tag{3.2.2}$$

$$Var[X(t)] \equiv E[(X(t) - m(t))^2] = \sigma_X^2 \tag{3.2.3}$$

where $E[*]$ is the expected value. The auto-covariance function of $X(t)$ describes the relationship between values of the random field at two coordinates t_1 and t_2:

$$B_X(\mathbf{t}_1, \mathbf{t}_2) \equiv \mathrm{Cov}[X(\mathbf{t}_1), X(\mathbf{t}_2)] = E[X(\mathbf{t}_1)X(\mathbf{t}_2)] - m(\mathbf{t}_1)m(\mathbf{t}_2) \tag{3.2.4}$$

Since $X(\mathbf{t})$ is assumed to be homogeneous, the auto-covariance depends only on the lag $\tau = t_1 - t_2$. The spectral density is related to the auto-covariance by the

Smith-Kinchine relations,

$$B(\boldsymbol{\tau}) = \int_{-\infty}^{\infty} S(\boldsymbol{\omega}) e^{i\boldsymbol{\omega}\cdot\boldsymbol{\tau}} d\boldsymbol{\omega} \tag{3.2.5}$$

$$S(\boldsymbol{\omega}) = \frac{1}{(2\pi)^n} \int_{-\infty}^{\infty} B(\boldsymbol{\tau}) e^{-i\boldsymbol{\omega}\cdot\boldsymbol{\tau}} d\boldsymbol{\tau} \tag{3.2.6}$$

where the integral denotes integration over *n*-dimensions.

This is equivalent to assuming that log rain rate, where raining, is a fractional Brownian field with a Hurst coefficient of 1/3 (Paulson, 2002). The Hurst exponent H is related to the spectral density exponent of the measured rain fields, and is also related to the fractal dimension of the contour lines enclosing areas of equal rain rate. The spectral density function for a 2D isotropic random field is given by:

$$S(\omega) \propto \omega^{-2H-2} \tag{3.2.7}$$

Theoretical analysis and observation of rain rates from radars and rain gauges show that the slope of this power law is $-\frac{5}{3}$ for one-dimensional fields (R. K. Crane, 1990; Veneziano and Bras, 1996; Paulson 2001). The two-dimensional spatial variation of log rain rate, measured using meteorological radar, has been shown to have spectral density function with a $-\frac{8}{3}$ exponent (Paulson, 2002). A log rain rate, power-law spectral density with exponent $-(n+2/3)$, where n is the dimension of the random field, has been shown to be a good model of spatial and temporal rain rate variation in widespread, stratiform events.

Using such a model, temporal and spatial rain rate fields can be simulated at all scales of interest while such models of log rain rate are only valid in areas of non-zero rain rate (Paulson, 2003). The model is expected to be a good representation of variation over scales that are smaller than event size and larger than the raindrop-turbulence decoupling scale, estimated by Lovejoy (2007) to be 40 cm.

3.2.2 Rain Cell Models

Many studies have attempted to parameterise the shape of rain events. Rain events have been defined as regions where the rain rate exceeds some threshold. Recently Callaghan has shown that these regions have boundaries that are fractal and consistent with the spectral model of Paulson. However, historically rain cells have often been modeled as circular or elliptical. Attenuation models derived from rain cell statistics have either assumed rain rate variation within rain cells to be constant, a Gaussian profile or to decline exponentially from the centre. Several parameters are needed to specify a rain-cell profile i.e. radius of the rain cell, the maximal rain intensity $R_{\max}$ at the center of the rain-cell and one or more parameters to specify the rain cell profile (A. Paraboni, C. Capsoni and C. Riva, 2002).

The constant rain-cell profile is frequently used in hydrological modeling where rain accumulation is the parameter of interest. However, these models do not reproduce the second order statistics of rain fade. For example, the covariance of rain fade on two links is determined by whether the rain event spans the two links or not. Allowing smoother variation of rain rate within the cells is expected to yield better second order statistics. The exponential and Gaussian models have continuously variable rain intensity within the cell with the highest rain intensity values at the centre. The point rain intensity value R for different rain cell models can be derived from the rain-cell specification and the distance d from the center of the rain cell using the following relations:

In the case of the cylindrical rain cell model:

$$R = \text{constant}, \quad d < Radius \tag{3.2.8a}$$

In the case of the exponential rain-cell profile,

$$R = R_{\max} \cdot e^{\frac{4d}{Radius}}, \quad d < Radius \tag{3.2.8b}$$

In the case of the Gaussian rain cell profile,

$$R = R_{\max} \cdot e^{\frac{1}{2}\left(\frac{3d}{0.8Radius}\right)^2}, \quad d < Radius \qquad (3.2.8c)$$

Then the calculation of rain attenuation across a rain-cell can be computed by using following equation:

$$A_{incell} = \int_0^l k \cdot R^a(x)dx \quad [\text{dB}], \qquad (3.2.9)$$

where the values of k and a are the known frequency and polarisation dependent parameters, for example, Rec. ITU-R P. 838-2, $R(x)$ is the rain rate at position x along the path.

As part of a rain cell model, the choice of the physical model has to be carefully justified, for it has to account for the rain cell shape and for the rain rate horizontal distribution within the cell. A physical approach, HYCELL, has been proposed to model rain cells, relying on a hybrid distribution of the rain rate profile: a Gaussian distribution for the convective core and an exponential distribution for the stratiform part of the cell (L. Feral, F. Mesnard, H. Sauvageot, L. Castanet, J. Lemorton, 2000). This model produces annual fade distributions and is well suited for describing the spatial variability of rain rate at small scales up to some tens of kilometers. It cannot reproduce time-series, thus it is of little use for developing FMTs (Fade Mitigation Techniques).

For categorisation of spatial variation of rain rate within the cells, the rain cell population is usually divided into two groups: the stratiform cells, characterised by a slow decay of the rain rate from its maximum (which is usually chosen less than 10 mm/hr), and the convective cells, generating an area of heavy rain with intensities higher than 10 mm/hr. Often, convective cells are surrounded by a stratiform area where the rain rate is weaker.

3.3 Voss Algorithm

Voss (1985) devised several algorithms for the simulation of fractional fields to produce representations of clouds and landscape in computer graphics. Random Midpoint Displacement (RMD) is a recursive generating technique that is designed to generate fractional Brownian fields. RMD proceeds by iteratively interpolating to a finer scale and the addition of random Gaussian noise. At stage *n* with scaling ratio r, the random Gaussian noise will have a variance of $\sigma_n{}^2 \propto r^{2nH}$, $r = 1/2$ (R.F. Voss, 1985). Thus:

$$\sigma_{i+1}{}^2 = \left(\frac{1}{2}\right)^{2H} \sigma_i{}^2, \tag{3.3.1}$$

where H is the Hurst exponent.

RMD used for generating fractional Brownian fields (2D) in the algorithm proceeds in two stages. First the midpoints of each of the squares is calculated by smooth interpolation from its corners and shifted by a random element Δ. This determines a new square lattice at 45 degrees to the original and with lattice size $1/\sqrt{2}$. In the second stage, the midpoints of the new lattice receive a random contribution smaller by $1/(\sqrt{2})^H$ from the first stage. This produces the new square lattice with a scale $1/2$ the original. Thus, in each stage, the random Gaussian noise will have a variance of $\sigma_{i+1}{}^2 = \left(\sqrt{\frac{1}{2}}\right)^{2H} \sigma_i{}^2$. To generate N points requires only order N operations (Voss, 1985).

However, RMD method is unable to generate true long-term dependence, since, at each level of recursion in the algorithm; the midpoint calculations are all independent of each other. Also in fractional Brownian motion, all time spans of length Δt have the same variance, whereas in RMD simulations, this criterion can fail (Voss, 1985).

3.4 Time to Space Transformations of Rain Rate Statistics

The rain rate time series measured at a point is effected both by the advection of the rain field and its evolution. Over short periods, advection is the dominant effect. If the rain field is assumed to be a frozen pattern of rain rate, advecting with the ambient wind, the point rain rate time series is the same as rain rate measured instantaneously along a line through the rain field. This assumption is frequently used in the time-to-space transformation of rain statistics, and is known as the Frozen Storm or Synthetic Storm model (Usman, 2005).

A weaker assumption is that the evolution of the rain field is negligible compared to the point rain rate variation due to advection. This leads to Taylor's Hypothesis (Taylor 1938), which can be stated as the statistics of a point rain rate time series are the same as the statistics of the rain field restricted to lines parallel to the direction of advection. If $R(x,t)$ is the rain rate at point x at time t, then Taylor's Hypothesis can be written as:

$$R(x_0,t) == R(x_0+Vt,0) \tag{3.4.1}$$

where V is the advection vector and $==$ means "has the same statistics". Taylor's Hypothesis has been tested many times and has been shown to be valid for periods up to 40 minutes (Zawadzki 1973). The advection vector has been found to vary with rain type being larger for convective compared to stratiform rain (Matricciani and Pawlina 2000). The advection vector has been shown to be highly correlated with 700 mBar wind vector (Usman, 2005).

3.5 Summary

For the calculation of average annual fade distributions, the rain rates exceeded between 0.001%-1% of time are often used for the design of radio systems. Using the synthetic storm technique and methods such as Taylor's Hypothesis, rain rate spatial statistics such as correlation of rain rates and rain cell size diameters can be obtained from time series data. Recommendations on the average annual rain attenuation model in radio propagation applications, for locations around the world, have been provided by the ITU-R. Other prediction models in the literature for the estimation of cumulative yearly statistics have also been highlighted. Besides the average annual rain-fade distribution experienced by a terrestrial link, telecommunications operators are increasingly interested in the second order statistics of rain-fade, particularly for the development of fade mitigation techniques. For these applications, models are required that produce joint rain attenuation time series for networks of links. Some empirical methods can do this using time-series of rain radar images or by advecting rain fields derived from rain cell models. However, these methods lack the ability to produce time-series sampled sufficiently finely to develop FMTs. The Spectral Model describes fine-scale variation but is not valid at scales approaching event size and so will not reproduce joint statistics where more than one rain event is important.

CHAPTER 4 RAINFALL MEASUREMENTS

Generally, rain fade distributions have been estimated from point rain rate distributions. The transformation from point rain statistics to rain fade statistics depends upon the spatial variation of rain rate. Rain gauge networks have been used to give an indication of the spatial variation of the rain, though any fine structure of the rain field smaller than the distance between the gauges will be lost (Callaghan, 2004). Meteorological radars infer rain rate from near instantaneous measurements over arrays of voxels with diameters from hundreds of metres to tens of kilometers. Radar data has traditionally been used to calculate the transformation parameters from point to path integrated rain rates. However, radars infer rain rate from radar reflectivity. Both the measurement of radar reflectivity and the subsequent transformation to a rain rate can suffer from systematic and random errors.

In this chapter, rain rate measurement by gauge and radar is discussed. Specific datasets of rain rate measurements analysed later in the thesis are introduced. These include point rain rate time-series measured by RAL Rapid Response Drop Counting rain gauge (RRDCRG) and rain field time-series derived from the Chilbolton Advanced Meteorological Radar (CAMRa).

4.1 Rain Event Categorisation

Meteorologists classify rain events into convective, stratiform and frontal (K. C. Patra, 2001). Each class of rain events has important characteristics such as rain rate distribution, spatial statistics, the existence of vertical stratification etc.

Stratiform rain is usually widespread, with low rain intensity, and covers a large geographic area (Callaghan, 2004). It is also categorised by the existence of a "melting layer" due to ice crystals melting into rain drops as they fall through the zero-degree isotherm. The melting layer or "bright band" is easily observed in radar scans in a vertical plane (RHI: range-height indicator).

Convective rain is of the showery type usually encountered during the summer and autumn months. It is characterised by intense rain for relatively short periods of time. The radar echoes show that there is a great deal of turbulence inside the body of the convective cell, and the lack of a bright band (Callaghan, 2004).

Frontal rain occurs when a band of stratiform rain, often containing convective cells, is pushed across the area of interest by a strong wind (Callaghan, 2004). Fronts are linear events, often with large spatial extent (K. C. Patra, 2001).

Convective events are more spatially intermittent, with more turbulent boundaries and higher reflectivity, whereas stratiform rain tends to have smoother variation, lower reflectivity and can cover the area under investigation almost completely. Frontal rain combines aspects of the other two (K. C. Patra, 2001).

4.2 Rain Gauges

Rain gauges measure the amount of water falling through a small catchment area over a period of time. The catchment is usually determined by a funnel designed to catch falling raindrops and channel the water into a collection and measurement unit. Typical catchment areas are small fractions of a square metre and so rain gauge data are often treated as point measurements. In order to collect sufficient water to measure accurately, it is necessary to collect rain for some period of time. Historically, where the principal application has been hydrology, this period has often been one-day and, more recently, one-hour. For radio engineering applications much shorter integration periods are required. Specialist gauges for this application can have integration periods as short as ten seconds.

Rain gauges yield rain rate estimates with large systematic and random errors. Gauges disrupt the rain fields they are introduced to measure by changing the wind flow. A proportion of the rain that falls in the funnel either splashes out or evaporates before being measured. Similarly some water splashes into the funnel. The water takes some time to flow from the funnel to the measurement device. The measurement system and integration period may be optimised for light or heavy rain and yield systematic errors for other intensities. They are very difficult to site and expensive to operate and maintain. Sites must be sufficiently far from tall objects, e.g. buildings and trees, for the wind field not to be influenced. Ideally the gauge should be set in the ground with the funnel at surface level. Gauges also need to be secure from human and animal damage. These restrictions make gauges almost impossible to site in urban areas.

There are many kinds of rain gauges available in the market, such as the tipping bucket type, weighing bucket type or syphon (float) type gauge (K. C. Patra, 2001). Other gauges measure water volume capacitively or by producing and counting equi-sized drops. Acoustic gauges infer rain rate indirectly from the sound of drops impacting on solid or liquid surfaces.

The tipping bucket rain gauge has been the standard for the Environment Agency and water companies for decades. This type of gauge collects rain water into small containers that tip at a given collection volume. The time of tips is recorded, generally to the nearest second. The gauge can be installed in remote areas and the data transmitted to a central data store or recorded locally for periodic collection. These gauges can have very fine rain-height resolution but the one-second temporal discretisation leads to uncertainty in low rain rates. The physical tipping mechanism leads to systematic errors in the measurement in intense rain.

A weighing gauge measures water content by the change in water accumulation weight. This has the advantage that solid and liquid hydrometeors are treated identically, once in the weighing container. The weighing container requires periodic emptying and this must occur outside raining periods or a break in data record will occur.

For a tilting-siphon rain gauge, the rainwater in a collector displaces a float so that a marking pen attached to the float makes a continuous trace on the paper. The tilting-syphon gauge yields accumulated rain heights as a function of time and so rain rate is a derivative parameter. This is the reverse of tipping bucket gauges. The mechanical action of the float and pen leads to systematic errors in rain records.

A single rain gauge provides a record of the rainfall rate at a point, with some, possibly small, integration time. This is useful for studying the temporal statistics of rain, while the length of the observation time has to be taken into account. The data sets with very long observation times, in the region of decades, often have very low temporal resolution, such as daily and hourly rainfall accumulations (K. C. Patra, 2001).

In order to obtain an indication of the spatial distribution of rain, networks of rain gauges can be used, such as the one in Barcelona e.g. Vilar (1986). However, the spacing between the gauges is crucial; any fine scale structure that appears on lengths smaller than the distance between the gauges is lost (Callaghan, 2004).

A single radar can yield rain rate time-series over areas that would require tens of thousands of rain gauges. Radars typically derive rain rate estimates from radar reflectivity averaged over three-dimensional spatial volumes of diameters ranging from tens of metres to hundreds of kilometres. Often measurements can be treated as instantaneous. The different spatial-temporal integration volumes, measurement locations, systematic and random errors make radar and gauge data very difficult to compare.

4.3 RAL Rapid Response Drop-Counting Gauges

In this project, three complete years of data from three Rutherford Appleton laboratory (RAL) Rapid Response Drop-Counting Gauges (www.chilbolton.rl.ac.uk/raingauge.htm) are used to estimate rain rates over 10 s intervals. Two gauges are located at Chilbolton Observatory (51.1445^{o}N, 358.563^{o}E), one is situated on the flat roof of a one-story building while another is sited on the ground a short distance away. The third gauge is situated on the flat roof of a two-story building, 9 km away at Sparsholt (51.0847^{o}N, 358.607^{o}E). Where averages over 9 gauge-years are discussed the average is over data from three gauges over three years. Rainwater collected in the 150 cm^2 gauge funnel passes through a sump to a device that produces equally sized drops. These drops are detected optically as they fall to a drain. The gauges record the number of drops in each 10 s interval, where each drop corresponds to a rain rate of 1.43 mm/hr. A rain gauge measurement can be thought of as rain rate averaged over the funnel collection area and an interval of time. Alternatively it can be treated as a spatial average over a cylinder of height $V(D)T$, where $V(D)$ is the fall speed of drops of diameter D and T is the gauge integration time (Kevin, 2002).

4.4 Weather Radar

Measurement of rainfall by weather radar is based on the principle that both the amount of power reflected from a volume of atmosphere containing rain and the rain rate are determined by the drop size distribution (DSD). The radar equation is given by:

$$P_r = \frac{P_t G^2 \lambda^2 \sigma}{(4\pi)^3 r^4}, \qquad (4.4.1)$$

where P_t is the transmitted power, P_r is the average received power, σ is the backscattering cross section of the target, G is the antenna gain, r is the range to target, λ is the wave length.

For meteorological radars, the radar pulse volume contains not one target but an ensemble of targets such as rain drops. The total power received from such a pulse volume consists of the vector contributions of the individual reflected powers from the falling hydrometeors. It randomly varies from one reflected pulse to the next due to movement of the precipitation within the volume, but over a period of the order of 10 ms, it is independent (Marshall and Hitschfield, 1953). Hence a requirement of radar is that a number of independent samples must be averaged to achieve a reliable echo estimate from each volume. For a given radar, all the terms of the radar equation are constant which can be combined together to give a coefficient C. It shows that the received power from a volume of precipitation has a $1/r^2$ dependence (Patra, 2001). The radar equation reduces to the following form:

$$\overline{P_r} = \frac{C \cdot Z}{r^2} \tag{4.4.2}$$

$\overline{P_r}$ is the averaged power for precipitation illuminated by an antenna. Z is the radar reflectivity. An empirical formula relating $\sum D^6$ and rain rate R is given by (Marshall and Palmer, 1973, Patra, 2001):

$$Z = \frac{1}{\Delta V}\sum_{\Delta v} D^6 = aR^b = 200\,R^{1.6} \tag{4.4.3}$$

where ΔV represents the volume illuminated at any instant and is given approximately by:

$$\Delta V = \pi\frac{h}{2}(r\frac{\theta}{2})(r\frac{\phi}{2}) \tag{4.4.4}$$

where θ and ϕ are the horizontal and vertical antenna beam widths respectively, h is the pulse length.

The symbol D represents diameter of the rain drop and Z is proportional to $\sum D^6$. The unit of D^6 is mm^6 and the unit of R is mm/hr. Z is in standard units mm^{6}m^{-3} but usually expressed in term of dBZ, dBZ $\equiv 10\log(Z)$.

It is seen from the above radar equation that the relationship between Z and rain rate is crucial when this radar equation is used. Note also that the rain drops in a sample volume yield the same reflectivity whether or not they are falling. The assumed drop fall speed is intrinsic to the transformation of reflectivity to rain rate and is likely to lead to significant errors in the presence of vertical air movements. Also, a range of DSDs, each with an associated rain rate, will yield the same radar reflectivity.

Meteorological radar data gives near continuous coverage over a region of interest at some resolution. The time required to physically move a large radar antenna leads to delays between measures across a scan.

Access to accurate, distributed precipitation data is the most significant factor that affects the ability to optimise radio network design. Thus, it is important to find the right way to combine data from weather radar, rain gauges and disdrometers, while covering large areas at high spatial and temporal resolution (K. C. Patra, 2001).

4.5 Estimation of Rain Rate From Radar Data

A large proportion of meteorological radars are designed to estimate rain rate. The result of this estimation is usually compared with other sources, such as local rain gauge measurements, to obtain verification and also to detect any deviations in calibration of the radar measurements. Measurements of drop size distribution (DSD) from distrometers may also be used in verifications.

Earlier conventional radars are only able to obtain one measurement from the precipitation field. This is reflectivity factor. In general, radar reflectivity is converted to rain rate using a power-law $Z-R$ relationship:

$$Z = aR^b \tag{4.5.1}$$

Many $Z-R$ relationships exist for different rain types and radars. It has been shown that the use of a simple $Z = aR^b$ relationship will lead to estimation errors up to

100% (Usman, 2005, Uijlenhoet, 2007).

The use of dual polarisation can provide a two-parameter estimate of the DSD and hence reduce errors in rain rate estimate by a factor of two (Usman, 2005). Dual polarisation agility radar has the ability to change the transmitted polarisation state between two orthogonal components, e.g. linear horizontal and vertical polarisation on a pulse-to-pulse basis. Dual polarisation diversity radar has the ability to receive alternate orthogonal polarisation. Such a system transmits only a single elliptical or circular polarisation and then can receive co-polar (e.g. horizontal transmit and horizontal receive) and cross-polar (e.g. horizontal transmit and vertical receive) components with dual receivers (Usman, 2005).

A dual polarisation radar takes advantages of the fact that rain drops have a degree of oblateness that is directly proportional to their sizes. The field of drops will have a larger cross-section of water in the horizontal compared to the vertical. A horizontally polarised radar pulse will therefore be backscattered more in this field of drops than a vertically polarised pulse resulting in more radar return for the horizontal pulse than the vertical pulse (Usman, 2005). This leads to the measurement of differential reflectivity defined in decibels as,

$$Z_{DR} = 10\log\left(\frac{Z_H}{Z_V}\right) \qquad (4.5.2)$$

Z_{DR} values for meteorological echoes typically range between -2 to +5dB. Values of Z_{DR} well above zero indicate the hydrometeors in the volume are horizontally oriented, with the larger values of Z_{DR} indicating more heavy rain. Values of Z_{DR} well below zero indicate the hydrometeors in the volume are vertically oriented. Values of Z_{DR} near zero indicate the hydrometeors in the volume have a nearly spherical shape, and mostly occur in light rain or drizzle (Usman, 2005).

One of the popular $Z_H - Z_{DR}$ relations is given by (C. W. Ulbrich, 1986):

$$R = CZ_H^{\alpha} 10^{\beta z_{DR}} \tag{4.5.3}$$

where Z_H is in standard units (mm^{6}m^{-3} or dBZ) and Z_{DR} is in dB. $Z_H - Z_{DR}$ derived rain rate estimates can still suffer from errors due to non-liquid hydrometeors, air movement and inadequate radar calibration.

4.6 The Chilbolton Advanced Weather Radar

The Chilbolton Advanced Meteorological Radar (CAMRa) is a dual-polarisation, Doppler radar, sited at Chilbolton in Hampshire, and operated by Rutherford Appleton Laboratory. It is the largest, fully steerable, meteorological radar in the world and yields the finest-scale, spatial, rain rate fields available.

The CAMRa operates at 3 GHz (propagation effects are generally small and so can be neglected) and produces images of rain, snow and hail that are used to develop and test propagation models for terrestrial and satellite communications. CAMRa is able to distinguish between rains which cause significant losses to telecommunication signals, and ice, whose effects can be negligible (Chilbolton Radar website, 2005).

CAMRa is able to characterise the structure of precipitation both horizontally and vertically. It can measure differential reflectivity as well as conventional radar reflectivity because CAMRa can achieve fast polarisation switching between horizontally and vertically polarised signals.

The linear depolarisation ratio can also be measured by CAMRa. It responds to canting of the particles in the radar pulse volume and is useful for identifying the asymmetrical melting of snow and ice because linear depolarisation ratio is sensitive to particle shape, dielectric constant and orientation with respect to the plane of radar polarisation (Chilbolton Radar website, 2005).

The basic features of CAMRa are listed in Table 4.6.1.

Frequency	3.0765 GHz
Power	560 kW
Pulse width	0.5 microseconds
Repetition rate	610 Hz
System noise figure	1.3 dB
Antenna diameter	25 m
Maximum scanning rate	1 degree/second
Beam width at 3 GHz	0.25 degrees
Maximum range resolution	75 metres
Cross-polar isolation limit	-34 dB
Maximum digitised range	160 km
Noise at 1 km	-36.7 dBZ
Reflectivity quantisation	0.25 dB
Differential reflectivity quantisation	0.125 dB
Cross polar quantisation	1 dB
Doppler unambiguous velocity	±15 m/s

Table 4.6.1 Basic Features of CAMRa (from www.chilbolton.rl.ac.uk)

In this project, the initial, coarse-scale rain field data is from the Chilbolton Radar Interference Experiment (CRIE), described in detail in the next section. These data provide a detailed, large and unbiased sample of the rain events experienced in the Southern UK from 1987 to 1989 (two years). The data was acquired in an 9 days on and 18 days off duty cycle, during which CAMRa scanned both horizontally (PPI) and vertically (RHI) every 10 minutes over a 50 degree sector with up to a 160 km range.

4.7 The CRIE Database Description

The Chilbolton Radar Interference Experiment (CRIE) was a two year rain measurement campaign between 1987 to 1989, designed primarily for development and testing of rain scatter interference models as part of the COST 210 project (COST210, 1991). During this period the CAMRa was operated in a predetermined mode in order to measure an unbiased sample of the rain experienced in the region.

The campaign provides a database of dual-polar radar reflectivity data measured at 10 minute time intervals, and with a spatial resolution of at least 300 m. Set horizontal PPI (Plan Position Indicator) and vertical RHI (Range Height Indicator) scan patterns were recorded in a ten-minute cycle for 9 out of 28 days. Each day was defined to start at 1200 GMT, lasting through to 1200 GMT the next day. The first 5 days of a period began at 1200 GMT on Monday, and continued through to 1200 GMT on the following Saturday. The final four days started at 1200 GMT on the next Monday and ended at 1200 GMT on the following Friday. If more than 24 hours were lost, then extra time was allocated at the end of the period. In this way, all weather conditions during the campaign period should have been sampled with equal probability (Usman, 2005).

For the PPI scans, each scan, at an elevation of 1.5^o, covered an area approximately 50^o in azimuth due southwest of the radar. It takes approximately 1 minute to complete a scan (the radar has a maximum angular velocity of 1 degree per second). Therefore, the scan duration is well within the 20 to 30 minutes duration for the lifetime of rain event (Zawadzki, 1973) and each scan represents a good snapshot of the rain field before any significant structural change has taken place.

The radar operated the duty cycle for two-years. The aim was to produce a statistically unbiased sample of the rain fields experienced in an average year. The resulting database contains 3199 scan sets, and 30590 records of no-rain. It has been used for radio system engineering studies; see Goddard and Thurai (1996&1997) and Tan and Pedersen (2000). Assuming the total collection period is an adequate representation of a whole year, the statistics can be presented as average annual statistics. Thus the rain sampling strategy involved in the radar measurements was not biased and data can be used statistically (Chilbolton Radar website, 2005).

The resulting raw measurements from the CRIE campaign are contained within a total of 117 files. Gated records of Z_H and Z_{DR} along a ray, for multiple azimuths are stored within a raster of block size 4092 bytes. Radar calibration of Z_H and Z_{DR} was done at specified periods during the campaign and the values are contained within the file format.

The calibrated and corrected, dual polar, reflectivity data were transformed into rain rates by Usman (2005). Rain rates were estimated by comparing measured and FIM (Fredholm Integral Method) derived Z_H and Z_{DR} values within a lookup table using a functional relationship in which Z_H scales with R for a constant Z_{DR}, $\frac{Z_H}{R} = f(Z_{DR})$ (Illingworth, 1989; 2003). The function of $f(Z_{DR})$ is well approximated by a third order polynomial. Anomalous reflections, not consistent with rain, were identified and removed.

The statistical properties of rain rate fields have been investigated on the 3199 PPI radar scans containing rain, acquired by CRIE dataset over a two-year period. Data were collected between the ranges of 4.8 km and 158 km from the radar and averaged over 300 m intervals. For this project, only the data between 10 km and 70 km are used. This is to avoid sample volumes being within the freezing level and to limit differences in volume averaging due to beam spreading. This yields 181 reflectivity measurements along each ray. The beam width is 0.25^{o} yielding 210 rays in each scan. At 9.9 km the azimuth volume width is 41.5 m, while at 72 km the azimuth volume width is 302 m. The short range limit is defined by the near-field of the radar while the long range limit has been chosen to limit the occurrence of melting layers in measured rain fields (I. S. Usman, 2005).

Each PPI scan has been range corrected, calibrated, and correction made for absorption by atmospheric gasses. Reflectivities below the noise floor of 10 dBZ were assigned a small value equivalent to a rain rate of 0.05 mm/hr. Negative values of differential reflectivity are assumed to be due to nonliquid hydrometeors or anomalous propagation and are eliminated from the dataset. The rain-hail algorithm of Leitao and Watson (M. J. Leitao and P. A. Watson, 1984) has been used to eliminate other data points where non-liquid hydrometeors may have influenced reflectivities. Finally, dual polarisation reflectivity data was transformed into rain rate fields (I. S. Usman, 2005).

The estimated radar rain rate statistics are compared with rain gauge statistics at the same site, and also statistics from ITU Recommendation P. 837-1 for the UK and P. 837-2 for Chilbolton in particular (I. S. Usman, 2005). The result shows the radar statistics are well representative of rain statistics within the region (J. W. F. Goddard and M Thurai, 1996).

4.8 Summary

In terms of instrumentation, rain gauges and radars are the most frequently used tools for the estimation of rain. In particular rain gauges are considered as “ground truth” instruments when comparing other measurements. Radars provide a distinct advantage in the observation of precipitation over wide areas. In addition their products have wide application within the areas of weather forecasting, radio propagation and communications.

We have discussed the CRIE measurement campaign dual-polar radar data collected over an area in the Southern UK over a sample days of two years. These data provide an unbiased sample of the rain events that occur in this region. Usman (2005) used a range of sophisticated algorithms to transform the dual-polar radar data into rain rate estimates, while identifying and correcting anomalous data. The resultant rain maps are the finest spatial scale rain rate data available with this spatial and temporal coverage. The 9 years of rain gauge data are also described and will be used to justify the introduction of finer-scale variation to the rain fields.

CHAPTER 5 SPATIAL AND TEMPORAL RAIN RATE VARIATION

5.1 Introduction

The statistics of variation of rain rate in time and space are often described by empirical scaling relationships. In this Chapter, the typical scaling relationships observed i.e. multiscaling and the special case of simple scaling are defined. The scaling of rain rate statistics at the finest scales available are calculated. These data are the CRIE database for spatial variation and rapid response rain gauge data for temporal variation.

5.1.1 Scales of Interest

The variation of rain rate over distances as short as one metre is of interest in a number of industrial and environmental applications. One application of significant economic importance is the design and regulation of microwave telecommunications systems using frequencies above 10 GHz, for both terrestrial and earth-space communications. The volume sampled by a terrestrial radio link at these frequencies in approximately the first Fresnel zone has a diameter of a few metres and a length between 100 m and 30 km. The Quality of Service (QoS) of such a link is determined by the sequences of "severely errored seconds" the system experiences, principally due to attenuation caused by rain. To estimate the QoS a node in an arbitrary network will experience knowledge of rain variation down to these scales is required. Similarly, the understanding of erosion processes, such as rill formation and water infiltration on inclined surfaces, requires knowledge of rain variation over scales as small as landscape features e.g. plough furrows, Wainwright and Parsons (2002) and Parsons and Stone (2006). Urban hydrology usually focuses on "city block" catchment areas of a few square kilometres. However, the drainage systems of small areas of hard landscape or complex roof systems, and the design of micro-hydroelectric schemes are of increasing interest and require knowledge of rain variation over these scales.

5.1.2 Why Does Rain Rate Vary

The variation of rain rate within rain events, particularly at the finest scales, is generally linked to variations in the vertical component of the wind field. The major updraughts and downdrafts on the scale of a few km or so, feed the energy at large scales which then cascade down the scale-spectrum to smaller eddies, following the Kolomogorov spectrum (Kolmogorov, 1941; 1991), until the energy is viscously dissipated as heat. Lovejoy and Schertzer (1992) describe rain as a “passive tracer injected at a certain scale in a turbulent flow”. At the large and small scales rain is not a passive tracer, but interacts with the atmosphere through condensation, coalescence and heat transport e.g. small drops (<10 μm) are formed by condensation in the updrafts, Atlas and Williams (2003). Droplet inertia leads to large concentration variation and differential drop velocities greatly increasing collision rates, Bec *et al* (2005). The variation of water vapour due to cloud turbulence also needs to be accounted for, Celani *et al* (2005), and these processes lead to multiscaling (for a definition of multiscaling see Section 5.2) distributions of water and ice in clouds. Radar and gauge studies have also reported multiscaling ranges in wide-spread rain rate variation and this has been qualitatively linked to turbulent energy cascades, Lovejoy and Schertzer (1992) and Veneziano *et al* (1996). Non-inertial models also predict multiscaling behaviour with a scale break at the energy injection scale, Falkovich (2005). At the smallest scales the inertia of drops is important while at increasing scales the stratification of the atmosphere becomes increasingly important and turbulent motions change from being three dimensional to two dimensional, Lovejoy and Schertzer (1992). Recently, Veneziano *et al* (2006) has suggested that rain rate fields are only approximately multiscaling, due to these mechanisms, and that rain models need to allow for this deviation.

5.1.3 Measurement of Horizontal Variation

Two dimensional rain fields have been measured either with meteorological radars or using arrays of rain gauges. Both these measurement methods have problems. Rain gauge networks are usually irregular and the gauge placement displays some fractal clustering statistics of their own. It has been shown that the measured scaling statistics of the rain rate field is affected by the placement of gauges in the array (H. G. E. Hentschel and I. Procaccia, 1983). Rain fields derived from meteorological radars are sampled on a regular polar grid i.e. evenly sampled in azimuth angle and range. However, the effect of this is the rain rate samples at different ranges are derived from averages over spatial volumes of different shape (aspect ratio) and volume. Many authors have calculated the scaling statistics of rain fields, uniformly sampled on a Cartesian grid, and produced by interpolating polar grid data. This method has two significant flaws, which lead to significant concerns on the reliability of these results. The scaling behaviour being investigated would be present in the original data and so the statistics of the measured rain field will vary with range. To some unknown extent, this variation will still be present in the derived Cartesian data. Secondly, it is unknown what effect interpolation will have on the scaling statistics. Without pre-knowledge of the scaling behaviour it is impossible to design an interpolation scheme that will conserve them.

5.1.4 Conclusions

Predictions of rain variation derived from models of raindrops interacting with a turbulent atmosphere suggest that statistics should exhibit scaling properties over ranges of scales. Concerns exist over the published spatial scaling statistics. These concerns will be addressed in the rest of this Chapter.

The scaling behaviour of rain rate fields derived from CAMRa with 300 m resolution is investigated using the moment scaling structure function (MSSF). The data investigated is sampled on a finer scale than any previous reported, with the exception of a recent PhD thesis by Callaghan (2004). The analysis has been designed to avoid the two flaws present in previously published work. No interpolation of the data is performed and rain rate samples are accumulated to yield voxels (three dimensional volume elements) of the same shape and size.

In addition to the radar data, nine gauge-years of rapid response rain gauge data at Chilbolton Observatory with a 10 s integration time have also been investigated. These gauges yield rain rate measurements with a temporal resolution of 10 s and a rain height resolution of 0.004 mm. The MSSF of rain rate was calculated and two scaling ranges were identified. The existence of positive moments of the underlying rain rate distribution will be determined by examination of the quantile scaling statistics of both rain gauge and radar data.

The spatial moment scaling statistics are calculated using a method that avoids the problems associated with the interpolation of polar data onto Cartesian grids and the variation of integration region with range. The statistical properties of rain rate fields have been derived from the 3199 PPI radar scans containing rain, acquired by CRIE experiment over a two-year period. A subset of the most reliable data including ranges from 9.9 km to 72 km, have been used. Each radar scan is treated as a snapshot of the rain field, measured at a regular 10-minute sample period. Each scan yields rain rate measurements centered on a regular polar grid of 208 rays $\times$ 208 range-gates. The rays are approximately evenly spaced at 0.25 degree intervals while the range gates are of constant 300 m lengths.

5.2 Fractal and Rain Field Multi-fractal Analysis

The word ‘fractal’ was coined by Mandelbrot in his fundamental essay from the Latin *fractus*, meaning broken, to describe objects that were too irregular to fit into a traditional geometrical setting. Many fractals have some degree of self-similarity;

they are made up of parts that resemble the whole in some way. The similarity may be deterministic or statistical (K. Falconer, 1990).

A self-similar object is composed of N copies of itself each of which is scaled down by the ratio r in all E coordinates from the whole. The property of self-similarity or scaling is one of the central concepts of fractal geometry. It is closely connected with dimension. A D-dimensional self-similar object can be divided into N smaller copies of itself each of which is scaled down by a factor r where $r = 1/N^{1/D}$. Thus, given a self-similar object of N parts scaled by a ratio r from the whole, its fractal or similarity dimension is given by:

$$D = \log(N)/\log(1/r) \tag{5.1.1}$$

Exact self-similarity is rare in nature while objects do often possess a related property statistical self-similarity. These objects can look statistically similar while at the same time different in detail at different length scales.

In rain fields, contour lines can be used to draw level-sets enclosing areas where the rain rate exceeds a given threshold. These contours exhibit statistically self-similar behaviour, which is consistent with fractal geometry (Callaghan, 2005).

Radar measured rain fields can be considered a fractal surface of a dense object in three dimensions, two spatial (x and y) and one showing the log rain rate (z). This assumption is useful for dealing with radar measurements because the rain rate value in the given radar range gate is a function of all the individual drops in that gate. In the case of a log rain rate field, it can be seen that the field is self-similar along the x and y directions.

The most useful mathematical model for the random fractals found in nature has been the fractional Brownian motion (fBm) of Mandelbrot and Wallis (1968, 1977 and 1982), which is a generalisation of Brownian walks.

A random variable described by fBm statistics, $V_H(t)$, is a single valued function of one variable, t (usually time). Its increments $V_H(t_2) - V_H(t_1)$ have a Gaussian distribution with variance $\langle |V_H(t_2) - V_H(t_1)|^2 \rangle \propto |t_2 - t_1|^{2H}$, where the brackets $\langle\rangle$ denote averages over many samples of $V_H(t)$ and the parameter H, known as the Hurst coefficient has a value $0 < H < 1$. Such a function is both stationary and isotropic. Its mean square increments depend only on the time difference $t_2 - t_1$ and all t's are statistically equivalent. The special case of $H = 1/2$ corresponds to a Brownian walk where the increments are uncorrelated. Other values of H correspond to systems with memory where increments are correlated or anti-correlated.

Fractional Brownian fields (FBf) have power-law spectral density functions, $S(\omega) = \omega^{-\gamma}$, with the power exponent being $\gamma = n + 2H$. A FBf $L(\mathbf{x})$ has Gaussian updates which satisfy the scaling equation:

$$\frac{L(\mathbf{x}) - L(\mathbf{x} + \Delta\mathbf{x})}{\|\Delta\mathbf{x}\|^H} \in N(0, \sigma^2) \tag{5.2.1}$$

Rain rate and rain field statistics depend upon the size and shape of the integration volumes used to derive the individual rain rate measurements. Descriptions of how rain rate statistics vary with the size of the integration volume are known as *scaling statistics*. Many authors have postulated that the scaling statistics of rain rate follow special forms known as *simple scaling* or *multi-scaling*.

The word multi-fractal is used to describe a model that is characterised by its multi-scaling features. A field is multi-scaling only if the variation of certain statistics of the field vary with the scale at which it is observed, and can be described using a simple function, e.g. the structure function. Extensive data analysis suggests that rainfall fields in time or space display such features over a range of scales (Lovejoy and Mandelbrot, 1985; Gupta and Waymire, 1993).

For example, if raindrops were Poisson distributed in a homogeneous rain field, then the number of drops $N(L)$ in a cube of atmosphere with diameter L of the order of metres would be proportional to the diameter cubed: $N(L) \propto L^3$. The total water volume would scale as L^6 and the scaling of all moments of drop number could be calculated from the one scaling exponent. As L became large, i.e. the order of the height of the rain event, then the scaling exponent of drop number would change from 3 to 2 i.e. the enclosed number of drops would depend upon the area of the cube rather than its volume. A scale break would exist where L equaled the rain height. The higher moments of drop number could still be calculated from the one scaling exponent. However, for real rain fields where drop concentration changes in all directions and over all scales, this is not true and the scaling of each moment needs to be empirically determined. In this case the field is called multiscaling.

Rain is believed to be multi-fractal and scaling in both intensity and time. Early fractal models of rain relied on a mono-fractal approach, where rain was simulated by the scaling sum of a large number of random increments or pulses of different sizes (Lovejoy and Mandelbrot, 1985). In this model, commonly known as 'simple scaling', a single scaling exponent describes the behavior of the statistical moments at different scales. The linear structure of such additive processes comes into conflict with the actual non-linear dynamics that produce rain. Instead, multiplicative models, stemming from the phenomenological cascade models studied in turbulence, were proposed. These require multiple exponents and are therefore more general.

Multi-fractal analysis of rain fields has been extensively published. The method used varied from study to study. Most fractal analysis of rain has moved from the simpler monofractal analysis and description to the more complex multi-fractal analysis and synthesis (Lovejoy and Schertzer, 1985, 1995; Deidda, 1999; Marsan *et al*, 1996).

There is a pronounced tendency in the published multi-fractal studies of rain fields to rely more on the mathematics and modeling of the theory than on the actual physical measurements and results provided from the rain gauge or radar data (Callaghan, 2004).

In the following section, the multi-fractal analysis is used to identify spatial and temporal scaling ranges. The scaling behaviour of rain rate fields derived from CAMRa with 300 m resolution is investigated using the moment scaling structure function.

5.3 Quantile Scaling and Existence of Moments

Before the moment scaling statistics for both spatial and temporal rain rate variation are calculated for a range of moment orders, the existence of moments is determined by examination of the quantile scaling statistics of both rain gauge and radar data.

The following introduction summarises parts of the much more detailed description in Pavlopoulos and Gupta (2003). Consider the point rain rate process $R_\lambda(t)$ measured with an integration interval of length $T = \lambda T_0$ where $\lambda \in \Lambda$ a subset of $(0,1]$ and T_0 is the longest integration time considered. The cumulative probability distribution of rain rate is defined as:

$$F_\lambda^R(u) = P(R_\lambda < u). \tag{5.3.1}$$

This distribution is continuous and strictly increasing over the range $(0,+\infty)$. As a consequence, the quantile functions:

$$Q_\lambda^R(p) = \inf\left(u \in \Re \mid F_\lambda^R(u) \geq p\right) \tag{5.3.2}$$

are also continuous and strictly increasing for $p \in (0,1]$, and so are the inverse functions of the corresponding distribution. The moments of *q*th order are defined:

$$M_\lambda^R(q) = \int_0^\infty u^q dF_\lambda^R(u) \tag{5.3.3}$$

and exist only when this integral converges. The moments can be calculated from the quantile function:

$$M_{\lambda}^{R}(q)=\int_{0}^{1}\left[Q_{\lambda}^{R}(p)\right]^{q}dp \qquad (5.3.4)$$

Many authors have speculated on the shape of the extreme rainfall tail of the rain rate cumulative density function $F_{\lambda}^{R}(u)$ and the associated probability density function (pdf) $f_{\lambda}^{R}(u)$, e.g. Cho *et al* (2004), Kedem *et al* (1994). Where the pdf tail approaches a negative exponential i.e. $f_{\lambda}^{R}(u)\propto e^{-\frac{u}{u_0}} : u_0 > 0$, all positive moments exist. However, where the tail is rational i.e. $f_{\lambda}^{R}(u)\propto u^{-\alpha}$; $\alpha > 1$, then only positive moments $q<\alpha-1$ are finite. In practice, arbitrarily high rain rates do not occur. In the fine-scale limit, rain becomes quantised into raindrops. The largest dynamically stable raindrops, with a diameter of approximately 1 cm, fall with a terminal velocity of approximately 10 m/s. Rain rate averaged over spatial-temporal volumes entirely within the largest drops is approximately 10 m/s. Any spatial temporal volume that includes smaller drops, or regions between raindrops, will yield a lower averaged rain rate. In general, larger volumes will include more regions outside these extreme rain drops and so will yield a lower maximum rain rate. As rain rate is bounded above by the maximum possible value of 10 m/s, all moments exist.

5.3.1 Existence of Temporal Moments

Figure 5.3.1 illustrates the quantile functions for 9 gauge-years of rain rate measurements, for integration times from 10 seconds to 7 minutes. For 10 s integration and probabilities approaching 1 i.e. $1-p\rightarrow 0$, the quantile function approaches linearity in $\ln(1-p)$. The quantiles for probability: $1-p<5\times 10^{-7}$ are defined by less than 20 samples and so are not reliable. For longer integration periods the quantiles are bounded above by linear functions of $\ln(1-p)$. If the quantile function is bounded above by a linear function of $\ln(1-p)$ for all probabilities above some $p_c > 0 : Q_\lambda^R(p_c) = R_c$, then from $M_\lambda^R(q) = \int_0^1 \left[Q_\lambda^R(p)\right]^q dp$,

$$\begin{aligned} M_\lambda^R(q) &= \int_0^{p_c} \left[Q_\lambda^R(p)\right]^q dp + \int_{p_c}^1 \left[Q_\lambda^R(p)\right]^q dp \\ &\leq p_c R_c^q + \int_{p_c}^1 \left[A_\lambda + B_\lambda \ln(1-p)\right]^q dp \end{aligned} \tag{5.3.5}$$

By substitution, the second integral can be shown to be equal to $\frac{-1}{B_\lambda} e^{\frac{A_\lambda}{B_\lambda}} \int_{R_c}^{\infty} u^q e^{\frac{u}{B_\lambda}} du$ which exists and is bounded for all finite $A_\lambda, B_\lambda < 0$ and *q*. Therefore, all positive moments of point rain rate exist for all integration periods down to 10 s. These results are consistent with rain rate pdfs that are exponential in extreme rain rate before becoming equal to zero above a maximum rain rate that is determined by the size of the spatial-temporal integration volume.

The question remains as to whether the same is true in the short integration time limit, $T \to 0$. The slope of B_λ, the linear part of quantile $Q_\lambda^R(1-p) = Z_\lambda^R(p)$ as a function of $\ln(1-p)$, may be calculated as a function of integration period. If B_λ tends to a finite limit as the integration period reduces to zero, this implies that a model for rain rate distributions should always be bounded. The slope B_λ is approximately linear for integration periods between 50 s and 400 s. At shorter integration times the coefficient diverges rapidly from linear. As the current data only support four integration periods below this period, it is impossible to extrapolate to the zero integration time limit. There is also considerable uncertainty in the measurement of the extreme rains at these short integration times.

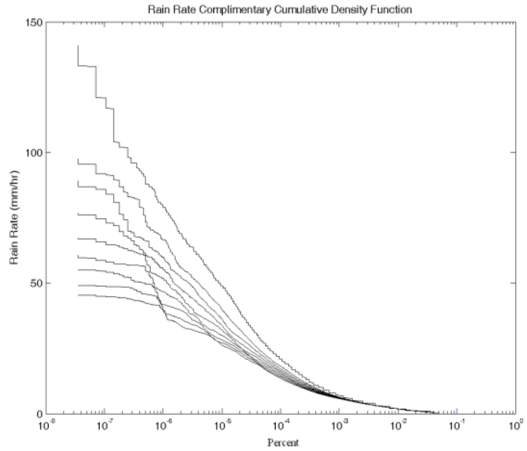

Figure 5.3.1 Rain rate exceeded with probability $1-p$ for integration periods, from top to bottom, of 10 seconds, 1, 2, 3, 4, 5, 6 and 7 minutes.

5.3.2 Calculation of Spatial Moments

The moments of spatially averaged rain rate have been calculated from radar images on many occasions. Terrestrial radars measure rain scattering parameters on a regular polar grid, centred on the radar. Typically, the radar scans near horizontally at a fixed rate of rotation. A measurement voxel is defined by the angles and ranges over which measurements are averaged. The height of a voxel is determined by the width of the primary lobe of the antenna pattern and for CAMRa this is 0.25^{o}. Therefore, rain radar data is averaged over voxels with tangential and vertical scales that grow linearly with range.

The usual process used to estimate the moment scaling statistics begins by interpolating the rain field derived from polar radar data onto a Cartesian grid e.g. Lovejoy (1982), Rhys and Waldvogel (1986), Deidda (1999) and Feral and Sauvageout (2002). The rain rate samples are then accumulated to yield integration volumes, with square footprints, with a range of sizes. This process is significantly easier on a Cartesian grid than a polar grid. However, there are several problems with this procedure. The statistics of the radar derived rain field are not homogeneous, due to the changes in the shape and size of the integration volume, but are a function of range. The design of an interpolation scheme that preserves the original statistics, before they are measured, is a significant problem. Even if this problem were addressed, the inhomogeneity in the polar data will be present in the Cartesian data and so it is not correct to accumulate samples with equal weights, for widely separated ranges. Finally, the increasing height of the radar voxels with range has not been addressed. Although radar voxels can be accumulated into voxels with the same footprint, those at greater range will have greater volume. It is likely that the vertical variation of rain rate will be much smaller than the horizontal variation, but this needs to be tested.

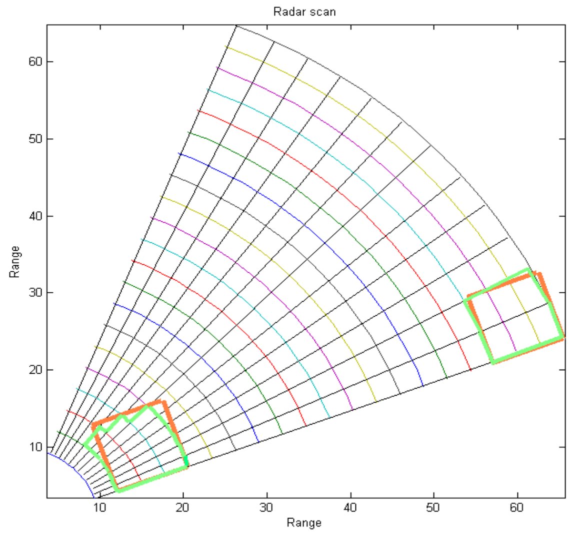

Figure 5.3.2 Accumulation of radar voxels to yield analysis voxels of similar size and shape

This work uses an accumulation process without interpolation. Analysis voxels are defined with square footprints and sides of lengths that are multiples of 300 m. Radar voxels are accumulated to yield volumes as close to the size and shape of analysis volumes as possible. Figure 5.3.2 illustrates radar data on a polar grid centred on a radar. Also indicated are two squares, target volumes and the best approximation formed by accumulating voxels on the polar grid. The rain rate sample is calculated as a weighted sum of radar rain rates with weights proportional to the radar voxel footprint area. Each rain rate sample calculated by accumulation is stored along with information on the mean range and a measure of the difference between the analysis and actual sample voxel shape and size.

Estimates of quantile functions can be calculated from the accumulated rain rate database. The CRIE database contains over 120 million rain samples from the regular polar grid, with each sample being an average over a voxel 300 m x 0.25^{o} x 0.25^{o} range x azimuth x elevation; in the ranges used for analysis. After accumulation this yields approximately 2000 million overlapping samples with footprints 300 m square, decreasing to 100 million samples 10 km square. Moments and quantiles can be calculated using subsets of the accumulated rain rate database to check for sensitivity to range or accumulation voxel size and shape.

5.3.3 Existence of Spatial Moments

Figure 5.3.3 shows the quantile functions for the whole of the CRIE database, for a range of spatial integration volumes of linear size 300 m, 600 m, 900 m, 2.1 km, 3.9 km, 6 km, 8.1 km and 9.9 km. Once again the quantile functions approach, or are bounded above by, linearity in $\ln(1-p)$. Therefore moments of all orders exist by the same argument used to analyse the temporal quantiles. The sensitivity of these results to the increasing height of voxels was checked by dividing the dataset in two subsets of analysis voxels with ranges less and greater than 40 km. The resulting quantile functions exhibit the same $Q_{\lambda}^{R}(1-p) \cong A_{\lambda} + B_{\lambda} \ln(1-p)$ interval but plateaus at different extreme rain rate values due to the different extreme events experienced by the two regions. The accumulated rain rate data set was also divided into two subsets depending on how well the square, target voxel was approximated by the accumulation of radar voxels. The quantile functions for the two sets had the same features but leveled-off at different rain rates for the same reason. This suggests that the voxel accumulation method is sufficiently good for all the data to be treated as accumulations over equivalent areas. It does not imply that the accumulation shape is not important, as all accumulation areas were close to square.

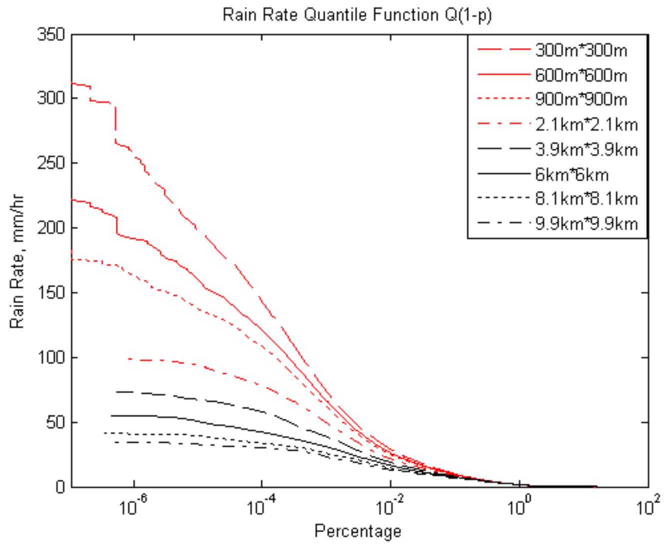

Figure 5.3.3 Rain rate exceeded with probability $1-p$ for spatial integration volumes

5.3.4 Simple and Multi-Scaling

The rain rate process $R_\lambda(t)$ is stochastically scaling if and only if there is a scalar process $\{C_\lambda\}_{\lambda\in\Lambda}$, such that $P(C_1=1)=1$ and $P(C_\lambda>0)=1$ for all $\lambda\in\Lambda$, and $R_\lambda \overset{D}{=} C_\lambda R_1$. Here $\overset{D}{=}$ denotes equality of probability distribution functions so that $P(R_\lambda \le r)=P(C_\lambda R_1 \le r)$. Special cases of scaling exist, depending on the form of the process C_λ . For simple scaling, also known as stochastic self-similarity, $P(C_\lambda=\lambda^\theta)=1$. In this case the finite moments scale as power-laws, and the scaling exponents $n\theta$ are linear in moment order:

$$M_\lambda^R(q)=\lambda^{q\theta}M_1^R(q) \tag{5.3.6}$$

Although the rain rate process cannot be simple-scaling due to intermittence, Kedem and Chiu (1987), it has been proposed that log rain rate, where raining, is well approximated as simple-scaling, Paulson (2001). The rain rate process is more commonly modeled as multi-scaling, Gupta and Waymire (1990) where:

$$C_\lambda=\lambda^\theta \exp\{Z_{\ln(1/\lambda)}\} \tag{5.3.7}$$

The process $\{Z_\rho; \rho \geq 0\}_{\lambda\in\Lambda}$ is such that $P(Z_0 = 0) = 1$ and has stationary increments: $Z_{\rho_1+\rho_2} \stackrel{D}{=} Z_{\rho_1} + Z_{\rho_2}$. Assuming independence of R_T and C_λ, the finite moments still scale as power laws, but the scaling exponents are now an arbitrary convex function of moment order i.e.

$$M_\lambda^R(q) = \lambda^{\xi(q)} M_1^R(q) \tag{5.3.8}$$

Having identified a process as having the properties of a multi-scaling process, a range of cascade processes can be used to simulate or downscale a given realisation (Lovejoy and Schertzer.1995; Ossiander and Waymire, 2000).

5.4 Multi-fractal Analysis

In the previous section, the existence has been verified of moments of all orders of spatial and temporal averages of rain rate. In this section a selection of positive moments are calculated for a range of spatial and temporal integration volumes and these data are used to identify scaling ranges

5.4.1 Spatial-Temporal Multi-fractal Analysis

A literature review revealed that two main types of scaling have been suggested for rainfall, simple scaling and multiscaling. Analysis results in the literature indicated that temporal and spatial rainfall intensities generally are characterised by multiscaling, whereas the fluctuations, i.e. intensity changes are typically simple scaling (C. Svensson, J. Olsson, and R. Berndtsson, 1996).

The multi-fractal analysis is used to identify spatial and temporal scaling ranges. The identification of scaling ranges allows modeling with strong control on the statistical moments. Spatial and temporal analysis and modeling are often treated separately.

Temporal variation is inherently one-dimensional. Temporal modeling aims to produce synthetic rain rate time series, or to downscale existing time series, in a way that is consistent with *a priori* known statistics, often multi-fractal scaling statistics. Spatial rain fields can be one, two or three-dimensional. Similar to temporal modeling, spatial modeling can aim to produce synthetic rain fields, or downscaling existing fields. The simultaneous downscaling of spatial and temporal dimensions is an open problem. It has been observed that sequential downscaling of spatial and temporal dimensions does not preserve the desired statistics (R. Deidda, 2000). Ultimately, algorithms are required to simultaneously downscale a mixture of spatial and temporal dimensions while preserving all *a priori* statistics.

In order to simulate the statistical properties observed in real-world precipitation events in both space and time, a spatial-temporal approach to modeling precipitation fields is required. Space-time rainfall can be considered to a good approximation to be a self-similar multi-fractal process (R. Deidda, 2000). The spatial and temporal statistics of rain rate variation are linked by Taylor's hypothesis (Taylor, 1938). Rain events evolve over time and advect with the ambient wind field. Taylor hypothesis states that the temporal statistics of rain at a fixed location are equivalent to the spatial statistics measured along a line parallel with advection. This is equivalent to assuming that rain variation is predominantly due to advection and that evolutionary effects are negligible. For this reason it is sometimes known as the frozen storm model. Taylor's frozen storm hypothesis (Taylor, 1938) presupposes that the spatial-temporal rain field may be approximated as a fixed spatial field moving with a constant velocity.

Taylor's hypothesis has been verified for periods up to 40 minutes on several occasions (Zawadski, 1973; H. S. Wheater, 1997). Using Taylor's hypothesis, temporal analysis and spatial analysis in one-dimension parallel with advection, are interchangeable. Transformation between spatial and temporal statistics requires a scaling factor linking the equivalent spatial and temporal units, which is often interpreted as an advection speed. At scales smaller than event sizes, rain fields are often assumed to be isotropic and so fine-scale temporal statistics can be transformed to spatial statistics in directions perpendicular to advection or to multi-dimensional spatial statistics.

5.4.2 Temporal Modeling

The following structure function will be used to characterise the spatial properties of rain rate in time over fixed areas of size λ. The statistics investigated is the *q*the moment of point rain rate averaged over different intervals of time:

$$S_q(\tau) = \left\langle [P_{\lambda,\lambda,\tau}(x,y,t)]^q_{\lambda=const} \right\rangle \tag{5.4.1}$$

where $\langle * \rangle$ is both an ensemble average or an average of samples with different starting times t and eventually different locations x, y. P is an integral measure of rainfall over an area $\lambda_x \times \lambda_y$ with an accumulative time τ. It can be defined as:

$$P_{\lambda_x,\lambda_y,\tau}(x,y,t) = \frac{1}{\lambda_x \lambda_y \tau} \int_x^{x+\lambda_x} d\xi \int_y^{y+\lambda_y} d\theta \int_t^{t+\tau} d\sigma \cdot R(\xi,\theta,\sigma), \tag{5.4.2}$$

where $R(x, y, t)$ is the notional instantaneous rainfall intensity continuous in space and time (F. Fabry, 1996). Section 5.4.4 investigates the spatial moment structure function i.e. moments of instantaneous rain rate averaged over squares of a range of diameters.

The analysis in time can be performed by investigating how the moments of time-averaged rain rate vary with the averaging time τ, keeping λ constant. In particular, in order to identify one or more ranges of timescales τ where the following scaling law holds:

$$S_q(\tau) \sim \tau^{\zeta_\lambda(q)} \tag{5.4.3}$$

Multi-fractal exponents $\zeta_\lambda(q)$ are functions of the moments q and do not depend on the timescale τ (Deidda, 2000). The multi-fractal exponent function $\varsigma(q)$ can be viewed as a characteristic function of multi-fractal behavior. It is used to characterise the multi-fractal nature of the measured radar data. For simple scaling fields, also known as mono-fractal, $\varsigma(q)$ is a linear function. When $\varsigma(q)$ is non-linear and convex, the underlying field is multi-scaling or multi-fractal (Deidda, 2000). Random fields can exhibit more than one, disjoint, ranges of scales, which are either simple or multi-scaling. Various experiments have demonstrated multifractal scaling of rain fields in one or more space-time dimensions e.g. Tessier *et al*. (1993) over scales 200 m to 2000 km, Schertzer and Lovejoy (1995) over scales 6 minutes to 30 days, Deidda (2000) over scales 15 minutes to 16 hours and 4 km to 256 km. A recent paper by Peters *et al* (2002) has used vertical pointing Doppler radar data to demonstrate several rain scaling results for integration intervals as short as 1 minute.

5.4.3 Temporal Analysis

Radar derived rain rate time series were calculated by tracking the rain rate at any one polar grid point (i.e. fixed area) in the observed radar scans. Where no-rain has been recorded at a scan time, rain rates of zero are put in the time series. Periods outside the 9 out of 27 duty cycle have been excluded from the analysis.

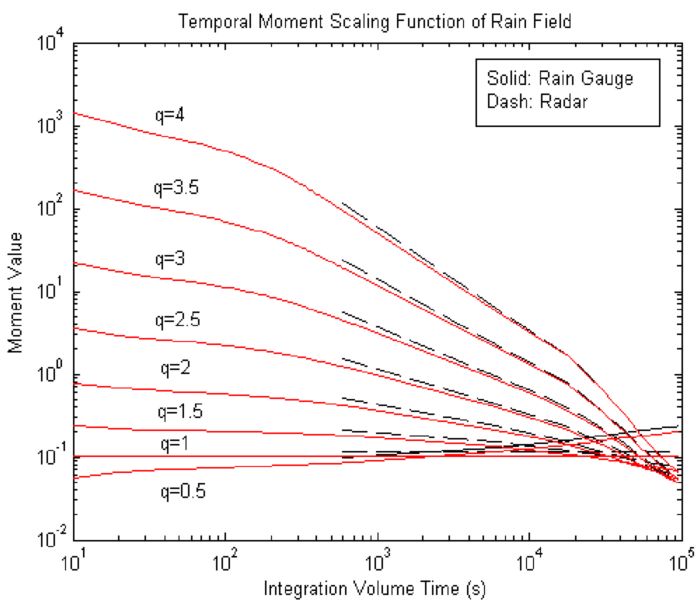

Figure 5.4.1 Moment scaling structure function for CRIE data and averaged 9

gauge-years rain gauge data (temporal modeling)

The validity of $S_q(\tau) \sim \tau^{\zeta_\lambda(q)}$ may be evaluated by plotting the average moments $\left\langle [P_{\lambda,\lambda,\tau}(x,y,t)]^q_{\lambda=const} \right\rangle$ as a function of τ in a log-log (base 10 is used) diagram. Figure 5.4.1 shows a plot of the average moments $\left\langle [P_{\lambda,\lambda,\tau}(x,y,t)]^q_{\lambda=const} \right\rangle$ (i.e. structure function $S_q(\tau)$) against τ for values of q between 0.5 and 4 with a step 0.5 both for radar data and 9 years rain gauge data. The rain gauge data were collected within 10 km of the CAMRa radar with a 10 s integration time.

The radar and gauge moment scaling curves in figure 5.4.1 are of similar shape with slightly different values. This is due to the different sample periods, locations and sample volumes for the two datasets. The *q=1* lines occur at a very similar level indicating that the mean rain rate is similar in both data sets. The *q=2* are slightly different indicating a slightly different variance.

As all positive moments exist, the moments considered are those of most interest in applications. Moments of high order are increasingly determined by the extreme rain rates in the dataset, with longer return times, and so are estimated to lower accuracy. The observed moments do not follow power-laws across the range of scales investigated. However, they are well approximated by three scaling intervals: approximately 10 s to 200 s, 200 s to 10000 s and above 10000 s. These three regions correspond to scaling intervals where different physical processes dominate.

Figure 5.4.2 shows the scaling exponents over the two scaling ranges 10 s to 200 s (dotted) and 200 s to 10000 s. For the moments of order $q \geq 1$ the scaling exponents are concave and well approximated by quadratics.

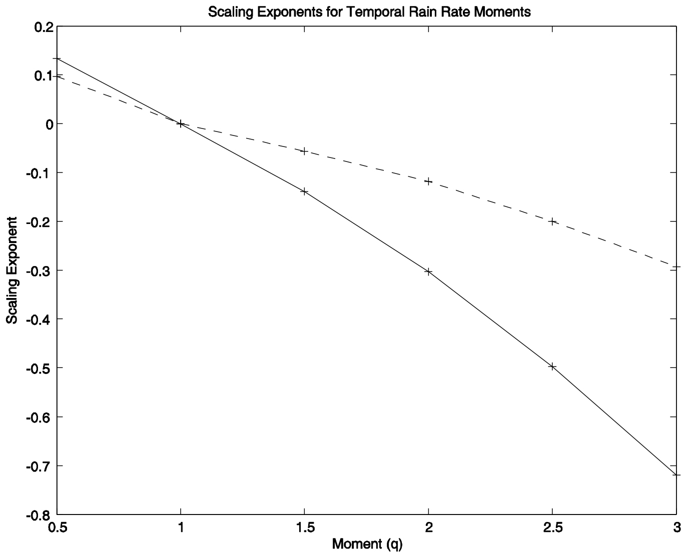

Figure 5.4.2 Moment scaling exponent as a function of moment order (Temporal Modeling)

5.4.4 Spatial Modeling

If a spatial field of rain rates averaged over a fixed duration τ can be considered as homogeneous and isotropic, the following moment scaling structure functions can be defined to characterise the spatial multi-fractal behavior:

$$S_q(\lambda) = \left\langle [P_{\lambda,\lambda,\tau}(x,y,t)]^q_{\tau=const} \right\rangle, \tag{5.4.4}$$

where $\langle * \rangle$ is an expected value, estimated using an ensemble average or an average of samples with different starting points x and y.

The multi-fractal analysis in space consists of the search for one or more ranges of spatial scales λ where the moments follow a scaling relationship:

$$S_q(\lambda) \sim \lambda^{\zeta_\tau(q)} \tag{5.4.5}$$

where $S_q(\lambda)$ is the ensemble average qth moment of the rain rate field averaged over areas of diameter λ (when normalized by the largest voxel diameter this is known as the scale ratio).

5.4.5 Spatial Analysis

In this section the moment scaling structure function of spatial rain rate variation is calculated. The purpose is to identify scaling ranges as these can be simulated using a number of known algorithms. This analysis has been performed several times in the past but the results reported must be treated with some caution. As mentioned in section 5.1.3, calculating scaling statistics of rain fields on a Cartesian grid, which is interpolated from polar grid data, will lead to unreliable results. Thus in this work, no interpolation of the data is performed and rain rate samples are accumulated to yield the same shape and size.

PPI rain field data is analysed by calculation of the mean moments of rain rate, derived by averaging over voxels of the same size and shape. These analysis voxels are calculated by combining radar measurement voxels. The analysis voxels were parallelopids with horizontal side lengths that were multiples of 300 m. The analysis rain rate was a weighted sum of the measured rain rates in the measurement voxels that were combined to approximate the target analysis voxel. The weights were the volumes of the measurement voxels divided by the total volume of the accumulated measurement voxels. The rain rate moments, averaged over analysis volumes, were averaged over all such volumes in each scan and across all 3199 scans.

The validity of $S_q(\lambda) \sim \lambda^{\zeta_\tau(q)}$ may be evaluated by plotting the average moments $\left\langle [P_{\lambda,\lambda,\tau}(x,y,t)]^q_{\tau=const} \right\rangle$ as a function of λ (spatial scales) in a log-log (base 10 is used) plot. Figure 5.4.3 shows a plot of the average moments $\left\langle [P_{\lambda,\lambda,\tau}(x,y,t)]^q_{\tau=const} \right\rangle$ (i.e. structure function $S_q(\lambda)$) against λ for values of q between 0.5 and 4 with a step 0.5. λ has values of 0.3 km, 0.6 km, 0.9 km up to 9.9 km.

As with the temporal moments, the observed moments do not follow power-laws across the range of scales investigated. However, they are well approximated by two scaling intervals: approximately 300 m to 1 km and above 3 km. The scale break apparent in the temporal data at 200 s is less clear in the spatial data. This may be due to anisotropy in the statistics along lines parallel and perpendicular to advection e.g. squall lines or fronts. Dotted lines in figure 5.4.3 indicate the linear fits used to derive scaling exponents.

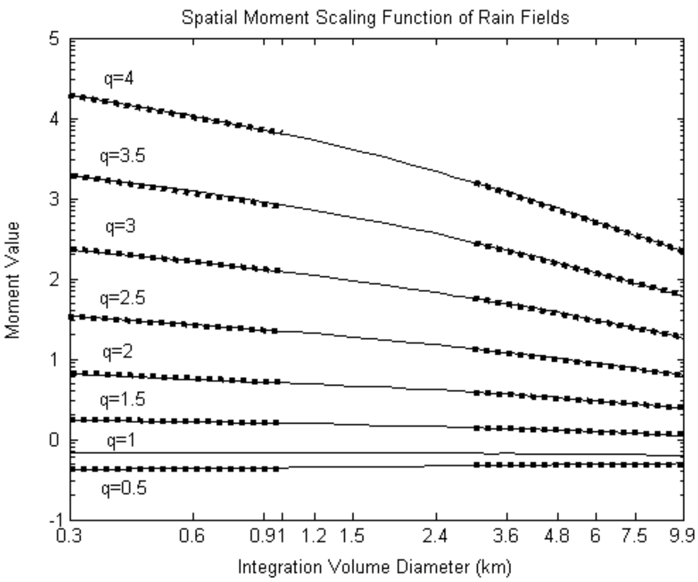

Figure 5.4.3 Moment scaling structure function for CRIE data (spatial modeling)

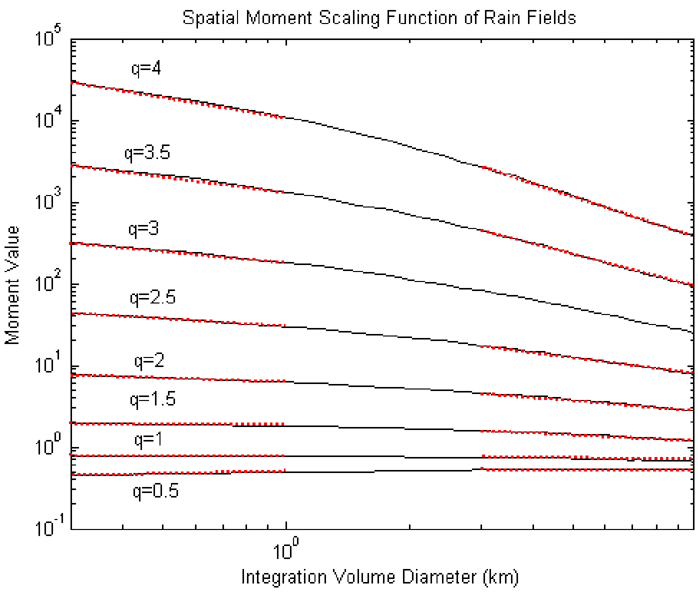

Figure 5.4.4 Moment scaling structure function for CRIE data (spatial modeling, near radar area)

Figure 5.4.4 and figure 5.4.5 shows the near radar area (similar ancillary information) and far radar area (similar ancillary information) moment scaling structure function for CRIE data. As the statistics are expected to be the same across the radar scan region, this analysis can highlight effects due to the methods used to calculate moment averages and voxel heights. Some variation is expected due to the sensitivity of high-order moments to extremes in the data. The same pattern occurs in all three analyses, figures 5.4.3, 5.4.4 and 5.4.5.

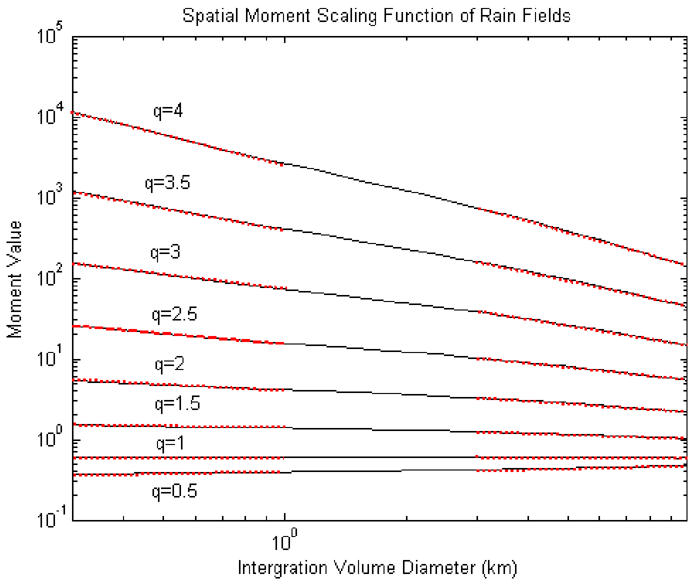

Figure 5.4.5 Moment scaling structure function for CRIE data (spatial modeling, far radar area)

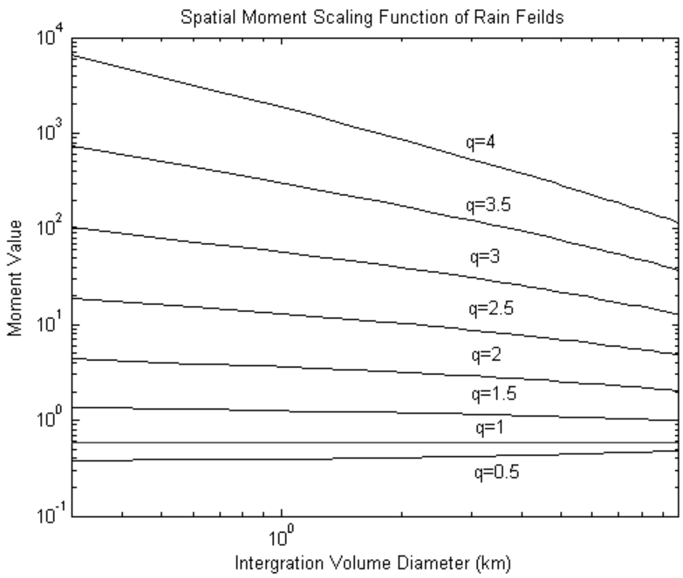

Figure 5.4.6 The calculated moment scaling statistics of rain fields after interpolation onto a Cartesian grid (spatial modeling)

Similar analysis of radar data has been reported several times in the past. In all the published analysis the radar data, acquired on a polar grid, has been interpolated onto a Cartesian grid before moment scaling statistics have been calculated. This process has never been justified. It is not clear how the interpolation process will affect the moment scaling statistics. Figure 5.4.6 shows the moment scaling statistic calculated using the interpolation method. Comparing them to the statistics calculated earlier, the moment scaling curves show the same general features but with significantly different scaling exponents.

For comparison, the scaling moments were calculated on rain data bi-linearly interpolated onto a regular Cartesian grid with samples separated by 300 m, before accumulation into larger sample volumes. The interpolation process reduced the extremes of measured rain rates and so reduced the values of higher order moments. The log-log moment scaling curves became much closer to linear across the scale range, obscuring the possible scale-break around 3 km. The moment scaling exponents were greatly reduced over the larger scale range identified in Figure 5.4.7. Using interpolated measurements could have lead to the conclusion that the data were approximately multi-scaling across the scale range considered, with scaling exponents much closer to zero.

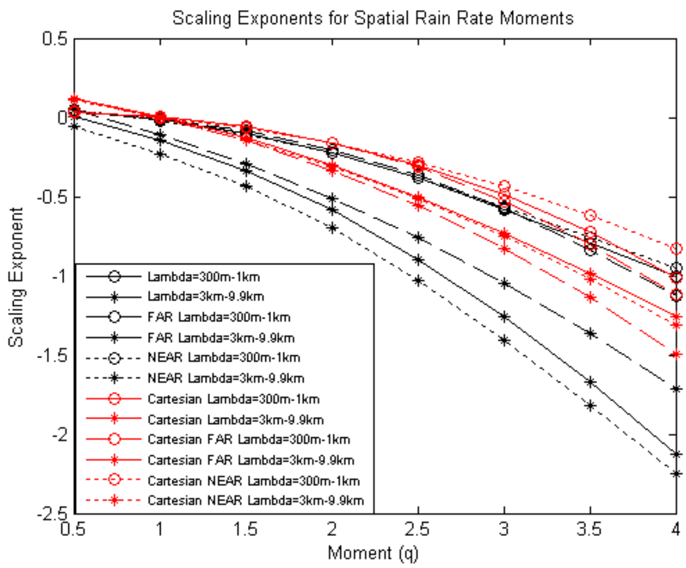

Figure 5.4.7 Moment scaling exponent as a function of moment order (calculated from the polar and Cartesian rain data) (spatial modeling)

Figure 5.4.7 compares the scaling exponent calculated from the polar and Cartesian rain data; it shows the scaling exponents $\varsigma(q)$ in the range $0.5 \le q \le 4$, for the two scaling ranges 300 m to 1 km and 3 km to 10 km. The scaling exponent variation is concave, approximately quadratic, and so multi-scaling. It is clear that there are significantly different scaling exponents between the values calculated from the polar and Cartesian rain data.

There is a decrease in moment scaling function $\varsigma(q)$ when q increases. This is because when the rain is averaged across whole scans, the resulting ensemble average is very small. When these average values are raised to exponents greater than 1, their value decreases.

5.5 Summary

Rain rate is a physical parameter that is only defined over some spatial or spatial-temporal integration volume. The moments of rain rate fields calculated from measurements derived from integration volumes of the same shape and a range of sizes, are commonly used as a summarising statistic of the rain rate process. Ranges of scales have been shown to be stochastically scaled, either simple or multi-scaling, when the moments are a power-law of integration volume size.

Radar data from the Chilbolton CAMRa radar in the UK has been analysed and the existence of positive moments of all orders demonstrated. An algorithm has been implemented for the calculation of moments from spatially averaged rain data on a regular polar grid. Three real and potential problems with the reported statistics are identified i.e. the existence of moments is not verified, the effects of interpolation have not been considered and the inhomogeneity introduced by variation in radar sample volume with range has been ignored.

The scaling behaviour of rain rate fields was investigated using the moment scaling structure function. The multi-fractal behaviour of rain fields observed by radar (from

CRIE database) was investigated by studying the variation of statistical moment $S_q(\lambda)$ with scale λ and $S_q(\tau)$ with scale τ. The moment scaling function $\varsigma(q)$ was studied.

The result shows that rain field is well characterised by a scaling behavior in terms of average statistics moment. The resulting moments are well approximated by two multi-scaling ranges with a scale break around 3 km or 200 s. Moment scaling function $\varsigma(q)$ is convex, which implies the field has as multi-fractal structure. The moment scaling statistic calculated using the polar grid and Cartesian grid have been compared. The moment scaling curves show the same general features but with significantly different scaling exponents.

CHAPTER 6 INTERPOLATION OF RAIN RATE FIELDS

The following two chapters explore the downscaling (disaggregation and interpolation) of rain data. Each rain rate measurement is an average over a spatial-temporal integration volume limited by the measurement technique. Disaggregation replaces a measurement with several measurements over smaller volumes e.g. if a rain gauge records hourly rain rates then disaggregation could transform each hourly rain rate measurement into two 30-minute rain rate averages. In general, disaggregation does not conserve the original rain rate distribution as rain rates derived from smaller integration volumes tend to be more extreme. Interpolation introduces rain rate measurements where there were none e.g. if one-minute rain rates were recorded every ten minutes then interpolation could generate new one-minute rain rates between existing ones. In general, interpolation conserves statistics, as the original rain rate samples are an unbiased sample.

The proposed network simulator requires spatial-temporal rain fields with integration volumes with diameters of tens of meters and sampling intervals of ten seconds or less. It is proposed to disaggregate and interpolate CRIE data to produce these data. The downscaling algorithms developed in the following chapters need to operate on data with the sampling and error characteristics of these data.

This chapter develops interpolation algorithms for rain fields. Interpolation methods are based on a range of algorithms such as the Random Midpoint Displacement algorithm of Voss (1985) and the Local Average Subdivision algorithm of Fenton and Vanmarcke (1990). Algorithms are tested on one, two and three-dimensional subsets of the CRIE data.

6.1 Rain Rate Statistics

A fundamental assumption driving the development of disaggregation and interpolation algorithms is: how should the rain rate statistics be changed by the process. In the simplest case, some statistics should be conserved. When rain rate data is interpolated, the coarse-scale data can be assumed to be an unbiased sample of the population of rain rates for that event. Interpolation algorithms should conserve these. However, the interpolated fine-scale data has samples with smaller sample intervals. The covariance of these samples cannot be directly estimated from the coarse–scale data and so a covariance model needs to be assumed.

The fractional Brownian model of log rain rate variation directly provides the covariance of log rain rate where raining. However, the rain rate moments as a function of scale are strongly affected by the non-raining areas and so these cannot be estimated from the Brownian model.

6.2 One-Dimensional Interpolation Scheme

A stochastic, numerical method to interpolate point rain rate time-series to shorter sampling periods, while conserving the expected first and second order statistics, was developed by Paulson (2004). The algorithm is based on the Random Midpoint Displacement (RMD) algorithm (Voss, 1985) designed to construct fractional Brownian fields; see Section 3.3. Paulson's algorithm applied Voss's algorithm to event time series of gauge-measured rain rate while raining. Smooth interpolation was achieved using a filter and additive Gaussian noise with a variance that decreased following the Voss power-law. The filter was calculated at each iteration so as to conserve event statistics. The full details of the analysis and development of the procedure can be seen in appendix A.

This algorithm was tested on rain rate time series extracted from the CRIE database. Each time series has a ten-minute sampling interval and is derived from the rain rate measured at single voxel in the region scanned by the radar, over the two-year experiment.

Each time-series has been interpolated using Paulson's algorithm and summary statistics calculated. Figure 6.2.1 compares the rain rate exceedance distribution in the original and interpolated radar-derived rain rate time series. Also plotted is the exceedance distribution for 9 gauge-years of rapid-response, drop-counting rain gauge data, acquired over a three-year period that does not overlap the CRIE collection period. The interpolated data has the same distribution as the original data and compares well with the rain gauge data down to 0.01% of the time. This is consistent with data collected over different years.

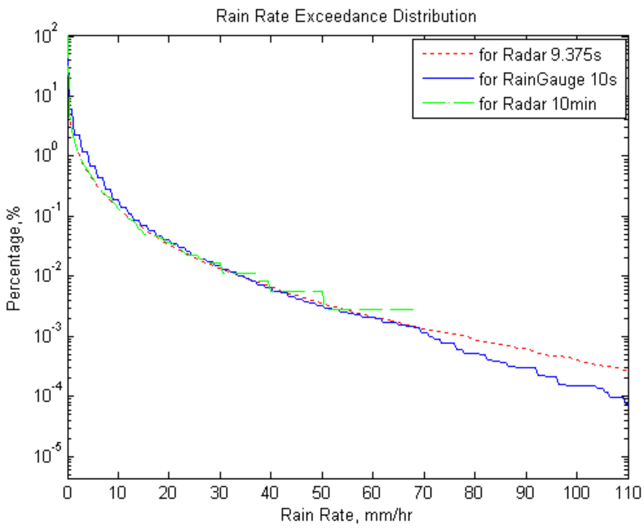

Figure 6.2.1 Comparison of the percentage of time that abscissa rain rates are exceeded from the measured radar rain rate data and with 1D interpolated rain rate time-series and 9 gauge-years of rain rate data

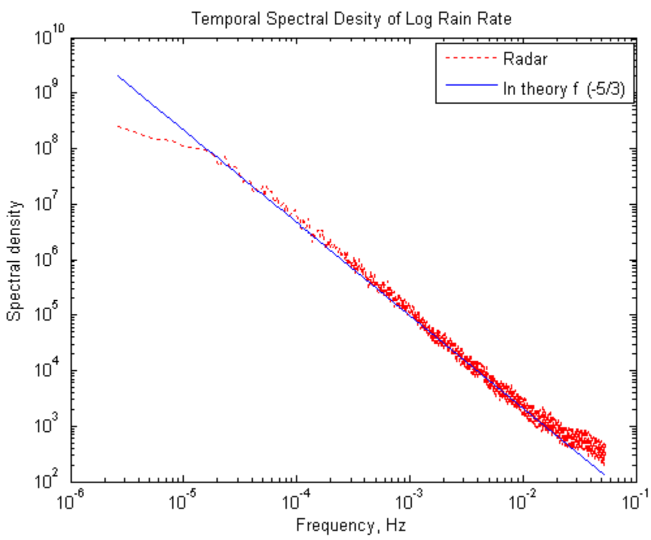

Figure 6.2.2 Average spectral density of log rain rate from interpolated radar rain rate compared with fractional Brownian $H = 1/3$ model (a power-law of –5/3)

Figure 6.2.2 shows the spectral density function of the interpolated rain rate time series and compares this with the power-law predicted by the fractional Brownian model. Only frequencies up to 0.00083 Hz were present in the original data. Interpolation has introduced the higher frequencies and these follow the expected power-law.

The 1D algorithm conserves the distribution of rain rates and introduces fine scale variation consistent with the fractional Brownian model.

The interpolated rain rate measurements are treated as 9.375 s averages and accumulated to yields rain rate measurements with longer integration times. The temporal moment scaling analysis has been performed on the derived time series with increasing integration times as shown in figure 6.2.3. It can be seen that the radar and gauge moment scaling curves are of similar shape with slightly different values. There is a scale break around 200 s.

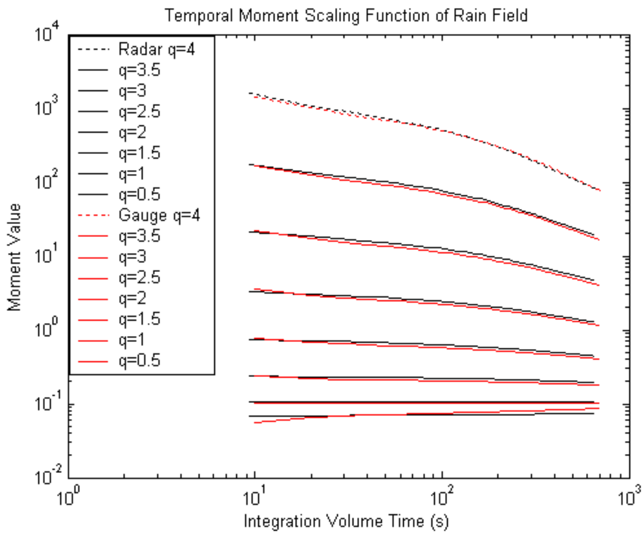

Figure 6.2.3 Moment scaling structure function for interpolated CRIE data and averaged 9 gauge-years rain gauge data (temporal modeling)

6.3 Two-Dimensional Rain Rate Interpolation

Rain rate near the ground can be interpreted as a collection of random variables forming a random field parameterised by three co-ordinates: two spatial co-ordinates and one temporal. In the following section, the interpolation of 2D spatial-temporal data is considered.

6.3.1 Two-Dimensional Spatial-Temporal Interpolation

The problem addressed in this section is the temporal interpolation of rain rates acquired along a line radial to the radar, corresponding to a scan line. The original data is rain rate averaged over 300 m range gates along the radial line and sampled at a 10 minutes interval. The aim is to interpolate these data to a temporal sampling period of approximately 10 seconds. This can be thought of as numerically generating the rain measurements that the radar could have made at these times, if the radar was stationary rather than scanning. The underlying assumption that log rain rate is an isotropic fractional Brownian field with Hurst coefficient equal to 1/3 is used. Two problems need to be solved to interpolate these data. Firstly, some method of equating temporal and spatial variation is required. Secondly, the spatial and temporal sampling will initially not be equivalent and so a variant of Voss's RMD algorithm needs to be developed.

The simplest transformation between spatial and temporal statistics requires a scaling factor linking the equivalent spatial and temporal units, which is often interpreted as an advection speed. A very simple formula *distance = time multiplied by the velocity* is used in Synthetic Storm models (Matricciani and Pawlina Bonati, 1994; 1996; 1997). The scaling factor used in this section is 10 minutes in time corresponds to 10 km in space, suggested by Paulson (2002). This can be estimated by equating the autocorrelation of temporal series and spatial series of rain rate with different lags. An alternative method uses the temporal-spatial spectral density function. When equivalent spatial and temporal units are used the spectrum is rotationally symmetric. This was the method used by Paulson (2002).

A temporal sampling interval of ten minutes corresponds to a spatial sampling of ten kilometers. As the actual spatial sampling interval is 300 m, the data is sampled approximately 33 times more finely in space than in time. An equivalent temporal sampling interval would be 18 seconds. An algorithm is needed to introduce 32 rain rate lines between each pair of scan lines measured ten minutes apart.

6.3.2 2D Interpolation Algorithm

If the two-dimensional spatial-temporal data were spatially sampled with a 10 km interval, the standard RMD algorithm could be used to interpolate simultaneously in the space and time dimensions. However, as more finely sampled data is available, the algorithm needs to be modified to be consistent with these. A possible adaptation is to use the RMD algorithm using measured data at the appropriate spatial separation at each iteration of the algorithm i.e. the first iteration would use points separated by 10 km in each of two consecutive scan lines. Subsequent iterations would use samples spatially separated by 5 km, 2.5 km, etc. This is only an approximate method because it has no mechanism to introduce the correct covariance between introduced points and measured data at intermediate points.

Furthermore, the asymmetric RMD algorithm described above needs to be refined in a similar way to the 1D algorithm to conserve the rain rate distribution. This has been achieved by expressing the smooth interpolation as a sum of two 2D filters. The algorithm is described in detail in the following paragraphs.

Consider a two-dimensional array of log rain rate samples $X = \{X_i = X(j\Delta x, k\Delta t)\}$ sampled at spatial intervals of Δx along the ray (initially $\Delta x = 300m$) and with a temporal sampling period of Δt, initially $\Delta t = 10$ minute. The single index i mapping onto the multi-index, (j,k) in 2D, is a notational convenience that makes algorithm developments independent of the number of dimensions. The new interpolates form a set $Y = \{Y_i\}$ via the Voss process $Y = S(X) + \varepsilon$. Here S

represents smooth interpolation and ε is the random noise process yielding Gaussian i.i.d. samples $\varepsilon \in N(0,\sigma_n^2)$. We choose the smoothing operator to be a linear FIR filter i.e. $S(X) = \sum_{i=1}^{n} a_i X_i$, where $a_i \neq 0$ only in neighborhood of Y_i. Furthermore we assume that, in the neighborhood of Y_i log rain rate variance can be described by random variation about a mean value i.e. $X_i = \overline{X} + \xi : \ \xi \in N(0,\sigma_s^2)$. This assumption allows the neighborhood mean and variance to be measured i.e. the mean is $\overline{X}$ and the variance is σ_s^2.

The interpolation problem then requires the filter coefficients $F = \{a_i\}$ to be determined such that $E(Y) = E(X) = \overline{X}$ and $E(Y^2) = E(X^2) = \overline{X}^2 + \sigma_s^2$. Other assumptions, such as isotropy in the fine-scale rain rate statistics, impose further constraints on the filter coefficients. The conservation of the mean implies that $\sum_{i=1}^{n} a_i = 1$. The variance constraint yields a similar relation between the sum of squares of filter coefficients, and the noise and rain rate variances σ_n^2 and σ_s^2. Many filters satisfy these constraints. We choose the filter F to be a linear combination of two filters: $F = \alpha * F1 + (1-\alpha)F2$. We have chosen the $F1$ coefficients to approximate a truncated Sinc filter while $F2$ has constant coefficients. Both filters are chosen so that the sum of filter elements is one. The conservation of the mean is therefore automatically enforced. The constant alpha is chosen to conserve the observed local variance. Additive Gaussian noise follows the Voss power-law. The details of the analysis and development of the procedure can be seen in appendix B.

6.3.3 Test of the 2D Algorithm on Brownian Data

An adaptation of the asymmetric 2D RMD algorithm using synthetic data with known statistics is tested. A square array of fractional Brownian field data, with $H = 1/3$, was generated using the standard Voss's RMD algorithm. Most of the data in the array will be deleted leaving only the data along the first and last columns. Then the refined and adapted algorithm will be used to regenerate the deleted data and the statistics of the interpolated array will be compared with the original. The objective is not to regenerate the original array as interpolation is a stochastic process. The algorithm aims to generate a fractional Brownian field equal to the original in the first and last columns, with the same marginal distribution and with the model spectral density.

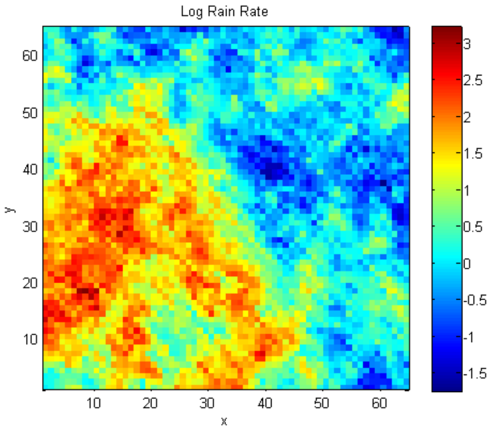

Fig 6.3.1A

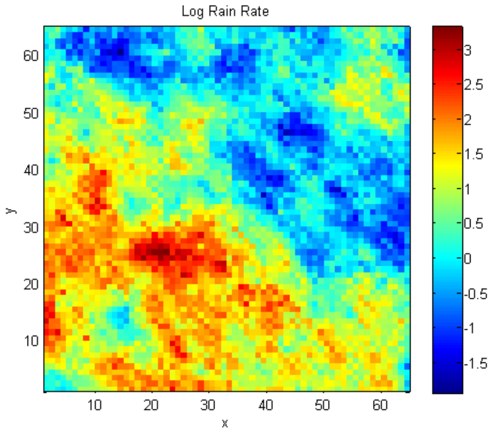

Fig 6.3.1B

Figure 6.3.1A An example of a 65 by 65 discrete fractional Brownian field with $H = 1/3$. Figure 6.3.1B is the result of interpolation between the first and last columns.

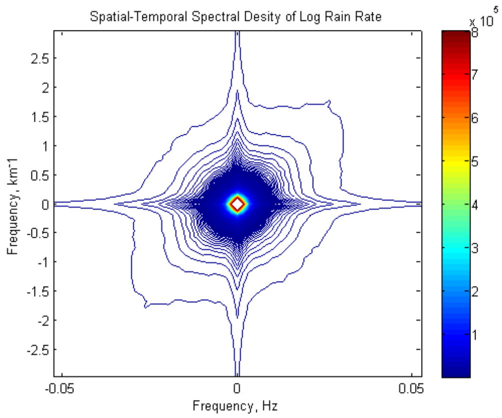

Fig 6.3.2A

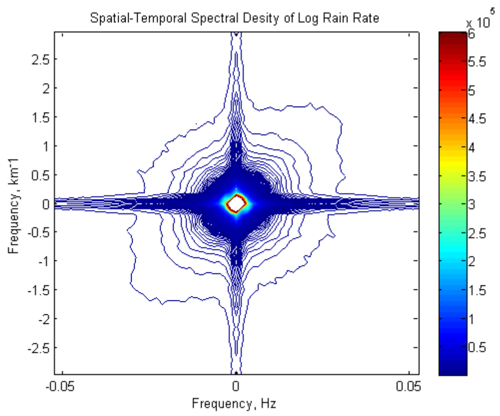

Fig 6.3.2B

Figure 6.3.2A&B 2D spectral density of data illustrated in Fig 6.3.1 A&B.

Figure 6.3.1A shows an example of an array of 65 rows by 65 columns of simulated log rain rate data generated using the standard Voss algorithm. Columns 2 through to

63 are subsequently deleted. Figure 6.3.1B shows the 65 by 65 array log rain field calculated by interpolation between columns 1 and 65 of the data illustrated in Figure 6.3.1A. Figures 6.3.2 A&B illustrate the spectral density of the random fields in Figures 6.3.1, treating them as spatial-temporal log rain rate fields with sampling intervals the same as the CRIE data. The contour levels are the same in these figures. Figure 6.3.2A has a slightly higher DC peak due to chance. Although different, the interpolated field has the correct distribution, spectral density and agrees with the original data in the first and last columns.

6.3.4 Test of the 2D Algorithm on Radar Data

The radar rain rate data (one ray data with 3199 scans) is interpolated to a time series with 9.375 s time resolution and 150 m space resolution using the method described above. The non-zero rain rates in the time-series were converted to log rain rate. In the original processing, radar reflectivities at the noise-floor of the radar were interpreted as 0.05 mm/hr rain rates. The initial interpolation scales are 10 minutes in time and 10 km in space.

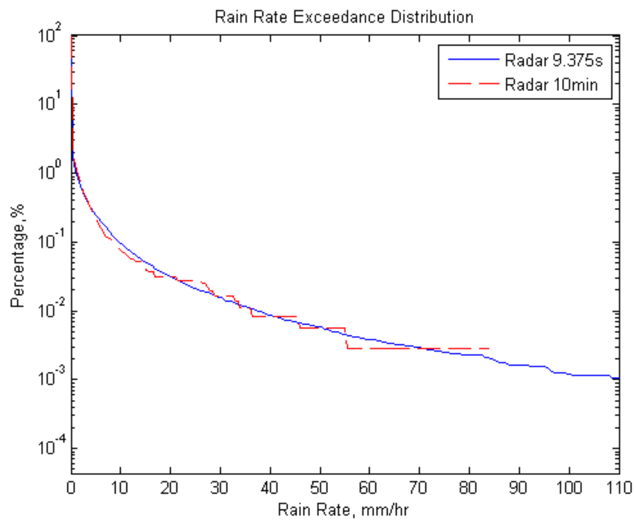

Figure 6.3.3 Comparison of the percentage of time that abscissa rain rates are exceeded from the measured and interpolated radar rain rate data.

Figure 6.3.3 compares the exceedance distribution of rain rates along a single scan line with those generated by the interpolation algorithm. The algorithm can be seen to be consistent with the original data at all exceedance probabilities present in the original data. The distribution has been smoothly extrapolated by the introduced samples.

The spatial-temporal spectral density function can be calculated by 2-D Fourier transform. Fixing the angular coordinate yields 193 (rays) two-dimensional data sets with coordinates (range gate, time). Each interpolated ray time-series is grouped into 193 consecutive scan lines of rain rates. This yields a large (3199*64/193) number of square, 2D spatial-temporal log rain rate datasets. Figure 6.3.4A illustrates the spectral density of spatial-temporal log rain rate variation, averaged over these data sets. The near circular contours are consistent with rotational symmetry, and hence the isotropy of the finer scales of variation. Figure 6.3.4B illustrates the rotationally averaged, radial, spatial-temporal, spectral density compared with the theoretical power law model with an exponent of -8/3.

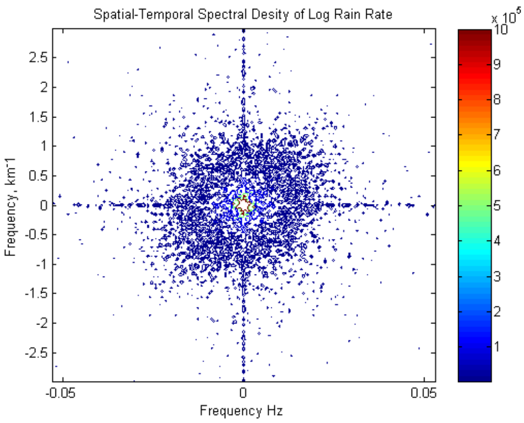

Fig 6.3.4A

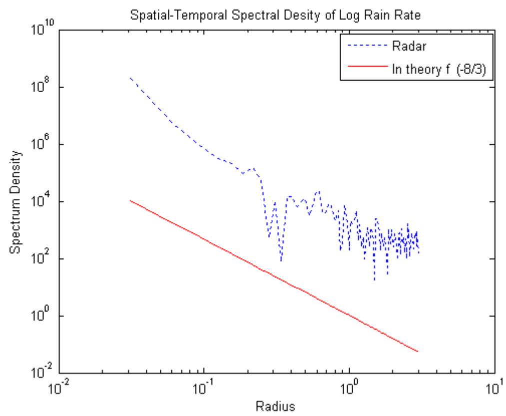

Fig 6.3.4B

Figure 6.3.4A Averaged spectral density of spatial-temporal log rain rate and Figure 6.3.4B the spectral density as a function of spatial-temporal range assuming rotational symmetry compared to a power-law with exponent of -8/3.

6.4 Three-Dimensional Interpolation of Radar Data

In this section we consider the interpolation of full radar scans i.e. we aim to numerically simulate the 2D spatial radar scans that might have been measured at times between two actual radar PPI scans.

Experience with the 2D spatial-temporal interpolation highlighted a number of deficiencies. It was noted that when a compact event was observed in consecutive scans, it was often of greater spatial extent in the interpolated scans. It was determined that this was due to advection being present in the dataset. Rather than advecting an event, interpolation tended to dissipate it in the original location while growing a new event in the subsequent location. To address this issue it was decided that the 3D algorithm would remove advection before interpolation and then reintroduce it afterwards.

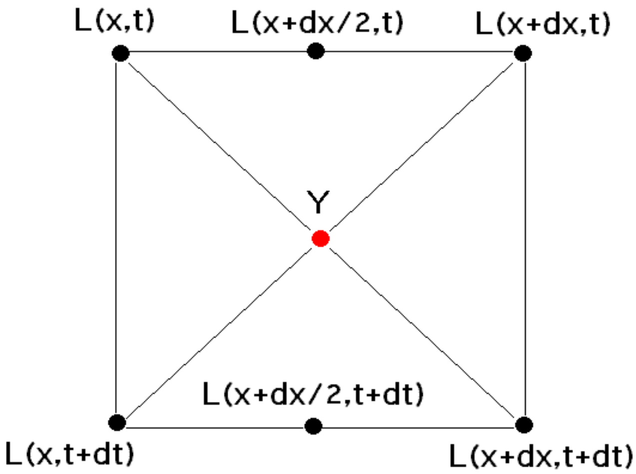

Figure 6.4.1 Relative positions of data points used for interpolation. Black dots are existing data while the red point indicates the interpolation position.

A second issue was the lack of covariance constraints on the introduced rain rate samples. Interpolates temporally near the measured scans needed to be conditioned upon measured data at scales finer than the interpolation scale. Figure 6.4.1 illustrates the situation. Given an interpolation scale of dx in space corresponding to dt in time, 2D interpolation used the four points at the corners of the square to smoothly interpolate the central red point Y. However, finely sampled spatial data is known at intermediate points at times corresponding to scans. These data are more highly correlated with the interpolate than the corner points and should be used to condition the smooth interpolation stage. A method more general than that used for 2D interpolation is needed.

Finally, interpolation often generated light rain events in regions where no rain was measured in consecutive scans. Although statistically this is possible, a mechanism leading to the generation of spurious rain events was identified. Regions of no rain and low rain rates corresponding to reflected power below the noise floor of the radar are treated identically in the data i.e. they are both set to the minimum measurable rain rate of 0.05 mm/hr. Interpolation across rain event boundaries will then mix real rain rate measurements with arbitrary values determined by the radar noise floor. Also, in areas of no rain where rain rates have been arbitrarily set to 0.05 mm/hr, the addition of random noise during interpolation leads to periodic generation of new rain events. A method of dealing with this anomaly was necessary.

6.4.1 3D Interpolation Algorithm

Each pair of log rain rate fields, $L_1 = \ln\left(R\left(\mathbf{x}+\mathbf{y}_A, t_1\right)\right)$and $L_2 = \ln\left(R\left(\mathbf{x}, t_1 + \Delta_t\right)\right)$, is assumed to be from a Gaussian fractional Brownian process, see Section 5.2 for justification for this assumption and for a description of the properties of FBfs. The marginal mean μ_L and variance σ_L^2 are estimated using a Maximum Likelihood algorithm for censored data: $L > L_{\min}$, where $L_{\min}$ is the smallest measurable log rain rate. Let $A \equiv \{A_i \in (x, y)\}$ be the set of spatial sampling points and $T \equiv \{t_1 \le T_i \le t_1 + \Delta_t\}$ be the equi-spaced interpolation times. The discrete interpolation volume is $V \equiv \{(\mathbf{x}, t) : \mathbf{x} \in A, t \in T\}$. Interpolated log rain rate values are calculated using a hierarchical algorithm that introduces new samples separated by distances that decrease exponentially with iteration. The Random Midpoint Displacement algorithm (RMD) of Voss (1985) has been used to refine isotropic FBfs and was adapted in the previous section to interpolate 2D rain fields. It is used as a starting point as existing samples are conserved at each iteration. The paragraphs below develop an algorithm for asymmetrically sampled FBfs. The method is loosely based on the Local Average Subdivision algorithm of Fenton and Vanmarcke (1990).

The RMD takes a FBf evenly sampled at scale Δ in each dimension and introduces new samples to yield a FBf sampled at scale $\Delta/2$. Let $L_\Delta = \{L_i; i = 1,\cdots N_\Delta\}$ be the log rain rate samples in a region of scale Δ around the interpolate L_Y at position ***Y***. The interpolated value is chosen to be:

$$L_Y = S(L_\Delta) + \sigma_\Delta \varepsilon_Y \tag{6.4.1}$$

where $S(L_\Delta)$ and σ_Δ^2 are estimates of the mean and variance of the L_Y distribution, while ε_Y is an i.i.d. standard Normal sample. For the asymmetric algorithm a linear estimator will be used i.e. $S(L_\Delta) = a_0\mu_L + \sum_{i=1}^{N_\Delta} a_i L_i$ where the coefficients a_i depend upon the shape and distribution of samples in the scale region and are chosen to satisfy:

$$E(L_Y) = \mu_L \ , \tag{6.4.2i}$$

$$E(L_y L_j) = B_{FBf}(\delta_{yj}) \ \text{ and} \tag{6.4.2ii}$$

$$E(L_Y^2) = B_{FBf}(0). \tag{6.4.2iii}$$

where $B_{FBf}(\delta)$ is the expected value of the product of two log rain rates separated by distance δ, given the FBf assumption. It may be calculated from the marginal distribution and (5.2.1) i.e. $B_{FBf}(\delta) = E(L^2) - \delta^{2H}\sigma^2/2$. Substituting (6.4.1) into the expected values in (6.4.2), and using the independence of L_i and ε_Y, yields:

$$E(L_Y) = a_0\mu_L + \sum_{i=1}^{N_\Delta} a_i E(L_i) = \sum_{i=0}^{N_\Delta} a_i \mu_L \ , \tag{6.4.3i}$$

$$E(L_y L_j) = a_0\mu_L^2 + \sum_{i=1}^{N_\Delta} a_i B_{FBf}(\delta_{ij}) \ \text{ and} \tag{6.4.3ii}$$

$$E(L_Y^2) = a_0^2\mu_L^2 + 2a_0\mu_L^2\sum_{i=1}^{N_\Delta} a_i + \sum_{i=1}^{N_\Delta}\sum_{j=1}^{N_\Delta} a_i a_j B_{FBf}\left(\delta_{ij}\right) + \sigma_\Delta^2. \qquad (6.4.3iii)$$

Equations (6.4.2i) and (6.4.3i) imply that $\sum_{i=0}^{N_\Delta} a_i = 1$. Furthermore, (6.4.2ii) and (6.4.3ii) yield a further N_Δ equations linear in a_i. The coefficients $\{a_i\}$ are found by solving these $N_\Delta + 1$ linear equations. Once the coefficients $\{a_i\}$ have been found, (6.4.2iii) and (6.4.3iii) yield an expression for σ_Δ^2.

For interpolation at the midpoint of regularly spaced samples and L_Δ taken to be the $N_\Delta = 2^n$ nearest neighbours, Voss's RMD algorithm generated FBfs using $a_0 = 0$, $a_i = N_\Delta^{-1}$ and noise variance exponentially decreasing with scale. In this case, the overhead in calculating interpolation coefficients is negligible. However, the CRIE rain data is more finely sampled in space than in time, where units are decorrelation intervals. Define the second order moment of measured data as:

$$B_L(\mathbf{y},\tau) \equiv E\left(L(\mathbf{x},t)L(\mathbf{x}+\mathbf{y},t+\tau)\right) \qquad (6.4.4)$$

An initial, interpolation scale of $N = 2^m$ sample units is determined: $B_L\left((N+1)\Delta_x \mathbf{e},0\right) \cong B_t\left(0,\Delta_t\right)$, where e is a unit vector. To yield samples symmetrically distributed in space and time, $N-1$, new, equi-spaced, log rain fields need to be interpolated. This can be achieved in *m* iterations of an asymmetric RMD (ARMD) using equations (6.4.1), (6.4.2) and (6.4.3). Interpolation regions of diameter $\Delta_0 = 2N$ in sample units are used in the first iteration and the diameter is halved at each subsequent iteration. The interpolation coefficients $\{a_i\}$ for the known L_i within the interpolation volume, and σ_Δ^2, need to be determined for each scale. Interpolation regions on the boundary of L, require coefficients consistent with the asymmetry of L_Δ, i.e. the existence of finely scaled measured data on L_1 and L_2 or the lack of samples outside L. However, all regions away from the boundary use the same coefficients.

Further interpolation to any temporal sampling period is possible using the method above. At finer temporal sampling, the log rain rate samples become more strongly correlated in time than in space and, in the limit, each spatial point yields a time series that can be refined using 1D RMD.

6.4.2 Test 3D ARMD on Numerical Data

In this Section the 3D ARMD algorithm is tested on numerically generated FBfs. A FBf with $H = 1/3$ and suitable marginal distribution can be thought of as a synthetic log rain rate field.

Figure 6.4.2A shows the middle (level 32) level (65 by 65) from a 65 by 65 by 65 discrete FBf with $H = 1/3$ generated using the standard Voss's RMD algorithm. The top and bottom levels are retained while all other data points are discarded. The ARMD interpolation algorithm described above is used to regenerate the discarded data. Figure 6.4.2B shows level 32 (65 by 65) of the interpolated 65 by 65 by 65 array. The spectrum density functions of both 65 by 65 arrays averaged over all 65 levels are shown in figure 6.4.3A and 6.4.3B. The cross in the centre of the graph is due to the edge effects of the 2D FFT. Assuming rotational symmetry, the rotationally averaged, radial, spatial-spatial-temporal, spectral density functions (calculated by using 3D FFT) compared with the theoretical power law model with an exponent of -11/3, are illustrated in figure 6.4.4B. Also, the mean and variance of rain field before and after interpolation are calculated and the results agree to within 2%. These figures illustrate that the ARMD algorithm conserves the marginal distribution and introduces new points with the desired covariance structure.

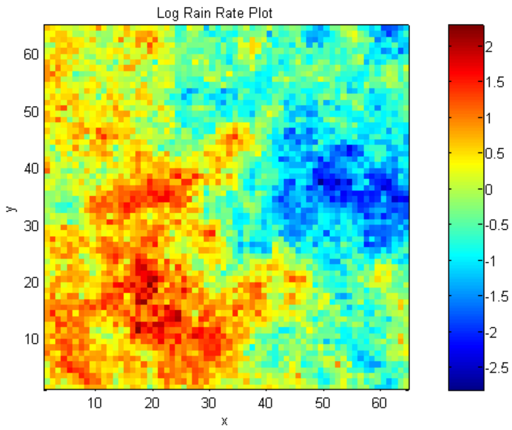

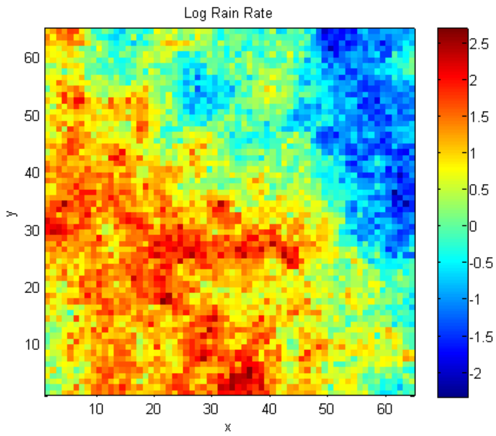

Fig 6.4.2A Fig 6.4.2B

Figure 6.4.2A An example of one scan in a 65 by 65 by 65 array of synthetic log rain rate samples generated using the standard Voss's RMD algorithm. Figure 6.4.2B illustrates an example scan of an array formed by interpolation of the data on the top and bottom surface.

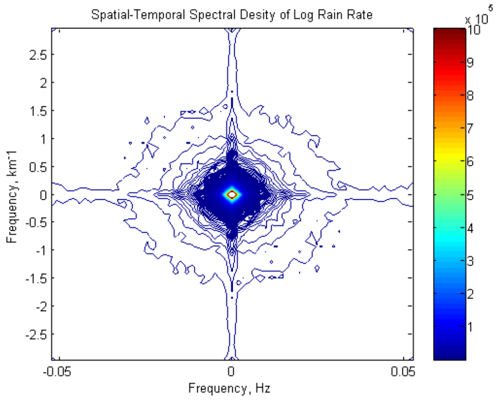

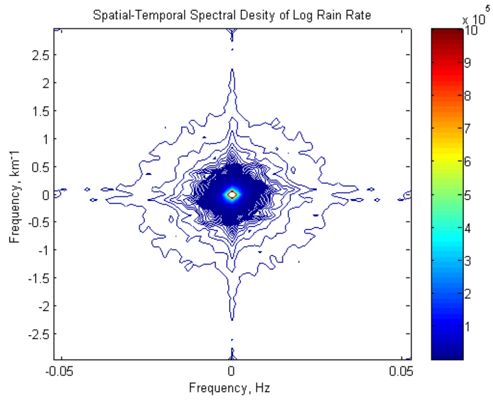

Fig 6.4.3A Fig 6.4.3B

Figure 6.4.3A&B Averaged spatial-temporal 2D spectral density of data illustrated in Fig 6.4.2 A&B.

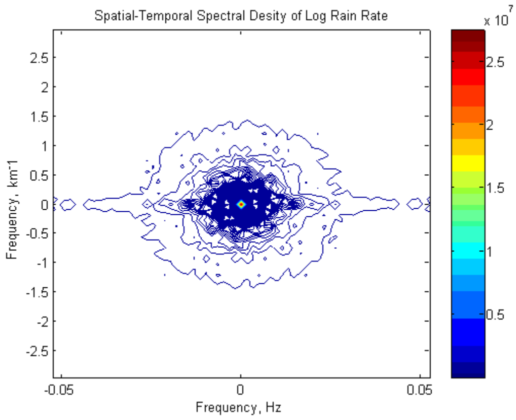

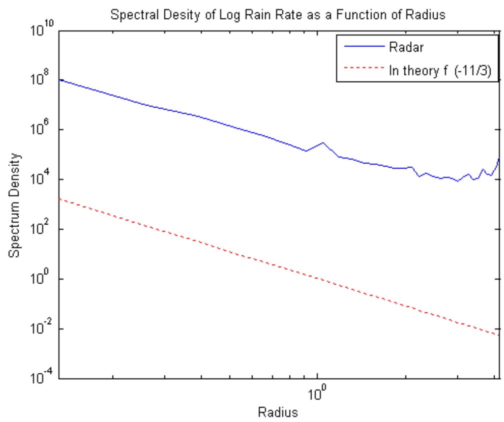

Fig 6.4.4A Fig 6.4.4B

Figure 6.4.4A Averaged 2D spectral density of spatial-temporal log rain rate. Figure

6.4.4B Averaged radial spectral density of 3D log rain rate, averaged over several scans assuming rotational symmetry, compared with the fractional Brownian $H = 1/3$ model (a power-law of –11/3)

6.5 Summary

Algorithms have been developed for the temporal interpolation of one, two and three-dimensional fractional Brownian fields. The 1D algorithm has been applied to point rain rate time series in previous studies and has been shown to be able to interpolate ten second rain rates sampled every ten minutes to a ten second sampling interval, while matching the first and second order statistics of the original data. This algorithm has been extended to higher dimensions and tested using discrete fractional Brownian fields. In Chapter 8 these algorithms are applied to rain fields derived from radar measurements.

CHAPTER 7 DISAGGREGATION RAIN RATE FIELDS

Disaggregation transforms rain rate measurements made with a particular spatial-temporal integration volume into a larger number of samples made with smaller integration volumes. In general, rain rate measurements made with smaller integration volumes exhibit greater variation i.e. very high rain rates are more likely to be measured with smaller integration volumes. When a rain rate is disaggregated to rain rates over smaller areas then the mean rain rate should be conserved as the total volume of rainwater collected over the larger area is equal to the sum of the volumes collected over the smaller areas. Other statistics are not conserved; for example the rain rate variance is expected to increase as the averaging volume decreases. The variance of the fine-scale rain rates cannot be directly estimated from the coarse-scale data and so a model of variance as a function of scale needs to be assumed.

For microwave network simulation it will often be desirable to have rain rate measurements made over spatial volumes smaller than the 300 m diameter yielded by CAMRa. Therefore a downscaling method is required that is applicable to these data and which can be integrated into a disaggregation and interpolation process. In Chapter 8 the integration is discussed in more detail. There it is shown that it is possible to disaggregate the radar scans independently before interpolation. Therefore, a 2D disaggregation algorithm is required.

In this chapter, the disaggregation algorithms are reviewed and Deidda's (1999, 2000) multiplicative cascade disaggregation method is presented.

7.1 Overview

A typical disaggregation procedure is based on the implementation of a stochastic disaggregation algorithm that is capable of generating a small scale fluctuating field from a smoother rainfall distribution on larger scale. In principle, this method provides random precipitation fields that should simultaneously satisfy the large scale constraints obtained by meteorological radar and are consistent with the known statistical properties of the small scale rainfall distribution.

A rainfall field produced by a disaggregation procedure is not a prediction of the fine-scale rain field that would have been measured if the appropriate instruments were available. The disaggregated field is a sample from the ensemble of fields that match the coarse-scale measurements and other conditioning statistics. Repeated application of the disaggregation procedure naturally leads to an ensemble of possible realisations of the fine-scale rainfall field and to the concept of ensemble rainfall prediction (Ferraris et al., 2002).

In past years, several stochastic models for rainfall disaggregation have been proposed. They can be grouped into three main categories. The following paragraphs describe each category. All these models have been proven to score fairly well in reproducing the observed statistical properties of precipitation (Ferraris et al., 2003).

Firstly, the spatial structure of intense rainfall is often conceptualised as a superposition of rain cells over different scales e.g. strong convective cells within small mesoscale area. This has lead to point and area process models based on the random positioning of a given number of rainfall cells (Waymire et al., 1984; Rodriguez-Iturbe et al., 1986; Eagleson et al., 1987; Northrop, 1998; Wheater et al., 2000; Willems, 2001). In these models, the rain process is modeled by simulating the band structure and the cell patterns, and the arrival times of the cells. Rainfall cells are usually circular or elliptical and have a constant or Gaussian rain rate profile. They are spatially distributed following a Neyman-Scott or Bartlett-Lewis process (Cowpertwait et al., 2002). These models have wide acceptance in hydrological modeling.

Secondly, autoregressive processes subjected to a static nonlinear transformation, also known as "Meta Gaussian" models (Mejia and Rodriguez-Iturbe, 1974; Bell 1987; Guillot and Lebel, 1999). In this model, the higher-order spatial correlation and the Fourier phase correlations are entirely generated by the posteriori nonlinear transformation, as they are absent in the original additive process before taking the transformation. It has been used to describe convective precipitation in tropical areas (e.g., Guillot and Lebel 1999). Kolmogorov (1962) has shown that a lognormal process can account for some of the observed scaling properties of three-dimensional, homogeneous turbulence.

Finally, multi-fractal cascades (Lovejoy and Mandelbrot, 1985; Schertzer and Lovejoy, 1987; Gupta and Waymire, 1993; Over and Gupta, 1996; Perica and Foufoula-Georgiou, 1996; Menabde et al., 1997a, 1997b, 1999; Deidda, 1999, 2000). Rain rate multifractality has been postulated to span scales from 40 cm to global variation (Lovejoy, in press). In recent years attempts have begun to incorporate cascade models in hydrological pulse models to increase the span of applicable scales (Onof, 2007).

All these models are characterised by an extremely fast numerical implementation and by a small number of free parameters. In each model, a lower amplitude threshold is also introduced. The threshold fixes the value below which the field produced by the model is set to zero. The threshold is necessary as most disaggregation models generate field values that are always different from zero, while rainfall fields are characterised by large areas of null values. An exception is the Multiplicative Beta Cascade method of Paulson and Baxter (2007) which includes a finite probability of introducing zero rain rates.

7.2 Disaggregation Using Multiplicative Cascade

In this thesis, Deidda's (2000) multi-fractal cascade method is employed. Multi-fractal cascade processes were introduced in the seventies and have been widely used to reproduce the variability of precipitation fields. Standard cascade processes are known to fail to reproduce observed spatial-temporal structure functions (Davis et al., 1004; Menabde et al., 1997b). For the network simulator, a 2D, spatial, multi-fractal disaggregation method is required that preserves spatial statistical properties observed in real rainfall. In the following paragraphs details of Deidda's (2000) algorithm based on multiplicative cascades are provided and applied to CRIE data.

The random cascade is constructed using a multiplicative process (Monin and Yaglom, 1971, 1975; Yaglom, 1966). Each son rain rate R_j^i at the *j*th level is obtained by multiplying the corresponding father at level *(j-1)* by an independent and identical distributed random variable w_i. Thus $R_j^i = w_i R_{j-1}$, where the scale at the level *j* is half of the scale at the level *(j-1)*. Ensemble average of *q* moments of random variables R can be related to the statistics of the generator w as following:

$$\overline{R_j^q} = R_0^q \overline{w^{q^j}} \tag{7.2.1}$$

Given knowledge of the distribution of rain rates at the coarsest scale, the moment scaling structure function can be established. Deidda (1999 and 2000) has proven that this structure function obeys the scaling law with expected multi-fractal exponent $\zeta(q)$ depending only on the ensemble averages of the moments of the generator w.

$$\zeta(q) = q(2 + \log_2 \overline{w}) - \log_2 \overline{w^q} \tag{7.2.2}$$

Using the Cauchy-Schwarz inequality, it can be proved that $\zeta(q)$ is a convex and nonlinear function of the moments q, so the model is suitable for generation of multi-fractal fields. The choice of probability distribution for the random generator w characterises the multi-fractal behaviour and the scale covariance of synthetic signals. In this work, the log-Poisson distribution is used. $w_i = e^a \beta^y$, where y is an i.i.d. sample from a Poisson distribution of mean c.

The q-order moment of the log-Poisson distribution is $\overline{w^q} = \exp[qa + c(\beta^q - 1)]$, when $q = 1$, then $a = c(1-\beta)$. And the expected scaling of synthetic fields can finally be evaluated:

$$\zeta(q) = 2q + c\frac{q(\beta - 1) - (\beta^q - 1)}{\ln 2} \quad , \tag{7.2.3}$$

where the multi-fractal exponents $\zeta(q)$ depend only on the parameters c and β. In order to reproduce a scaling regime in synthetic fields, parameters c and β must be scale-independent.

Estimates of the model parameters c and β can be obtained by solving the following minimisation problem:

$$\min_{c,\beta} \sum_q [\frac{\zeta_s(q) - \zeta(q)}{q-1}]^2 \ , \tag{7.2.4}$$

where $\zeta_s(q)$ are the sample multi-fractal exponents, $\zeta(q)$ is the theoretical expectation as above, and $q-1$ is a weight that accounts for the estimation error, that is, the standard deviation of $\zeta(q)$.

Examples of the method applied to CRIE data are presented in Chapter 8.

7.3 Summary

I have presented an algorithm due to Deidda (2000) that can disaggregate 2D fields and which yields a particular variation of the multifractal scaling exponents. For

CRIE data, these scaling exponents can be estimated from the moment scaling function over scales from 300 m to 10 km, see figure 5.4.3 and 5.4.7. Assuming that these exponents can be extrapolated to finer scales allows finer scale rain fields to be numerically generated from CRIE derived fields. Ultimately these need to be verified by fine scale rain rate measurements or, alternatively, from measurements that depend upon fine-scale variation such as microwave link attenuation.

CHAPTER 8 DISAGGREGATION AND INTERPOLATION ON CRIE DATA

Chapters 6 and 7 have presented algorithms to interpolate FBfs and to disaggregate rain rate fields. Rain fields measured by radar are typically near instantaneous measurements of volume averaged rain rate. The rain rates are spatially disaggregated but temporally sampled. To produce fine-scale fields for radio network simulation it is necessary to produce rain fields with much shorter temporal sampling interval and smaller averaging volumes. Therefore, a combination of interpolation and disaggregation is required.

In this chapter, these algorithms are applied to CRIE derived rain rate fields. These rain fields have properties that need special consideration. These are:

1. Intermittency i.e. large areas of no rain,
2. Advection i.e. rain fields both move and evolve,
3. Censorship of data due to radar noise.

Each of the properties will be discussed in the following sections.

8.1 3D Intermittency and Censorship

Numerically generated FBfs and measured log rain rate fields have significant differences in the marginal distribution due to intermittency of real rain i.e. rain events are finite in extent and separated by long intervals without rain, and measurement uncertainty. These lead to two significant problems for the multi-scale interpolation method. The marginal distribution of the measured rain fields is not log-Normal as all samples from voxels with no rain or very low rain rate are interpreted as having the threshold rain rate of 0.05 mm/hr. Secondly, the multi-scale interpolation uses spatially distributed samples to estimate the mean of interpolates. Some or all of these points could be in areas of no or very low rain rate. Therefore, choice of the threshold rain rate distorts the shape of rain events, as it relies on gathering log rain rate data from points where it is undefined. Replacing no-rain with a very small rain rate introduces problems in defining the mean and variance of log rain rate i.e. the choice of threshold rain rate dominates these summarising statistics.

8.1.1 Maximum Likelihood Estimation of the Marginal Distribution

The interpolation algorithm requires the mean and variance of log rain rate where raining, for each scan, to condition the interpolation. These parameters cannot be estimated directly using averages due to the uncertainty of the location of the edges of rain fields. Instead a Maximum Likelihood (ML) algorithm is used. The distribution of rain rates is assumed to be zero with some probability p_0 defined to be the probability of no rain, and log-Normally distributed otherwise. The probability density function $f(R)$ can be written:

$$f(R) = p_0\delta(r) + (1 - p_0)N(\mu, \sigma^2; \log(R)) \tag{8.1.1}$$

where μ and σ^2 are the mean and variance of log rain rate while raining. The probability of making a measurement at the threshold rain rate is therefore:

$$\Pr(R = R_t) = p_0 + (1 - p_0)F(\mu, \sigma^2; \log(R_t)) \tag{8.1.2}$$

where $F(\mu, \sigma^2; L)$ is the Normal cumulative probability function. Using (8.1.1) and (8.1.2) allows the log likelihood of a measured scan to be calculated. The ML method estimates the parameters p_0, μ and σ^2 by minimising the log likelihood functional. The ARMD algorithm also required the second moment function $B(\delta) \equiv E(L(\mathbf{x})L(\mathbf{x} + \delta\mathbf{e}))$ to be estimated. The 1D ML yields the marginal distribution for $L(\mathbf{x})$. A 2D ML algorithm can be used to estimate σ_δ^2 the cross-covariance of $L(\mathbf{x})$ and $L(\mathbf{x} + \delta\mathbf{e})$, assuming the marginal parameters given by the 1D algorithm. From μ and the cross-covariance $B(\delta) \cong \mu^2 + \sigma_\delta^2$ is estimated. For Gaussian $L(\mathbf{x})$ and $L(\mathbf{x} + \delta\mathbf{e})$ this is unbiased.

8.1.2 Extrapolation into Low Rain Rate Regions

The ARMD algorithm has been validated for FBfs. However, measured log rain rate fields have been censored at the threshold level $L_t \equiv \log(R_t)$. Interpolation at scales that cross rain event boundaries requires log rain rate values at points below the threshold. Using the threshold values inflates rain rates near the edges of events and leads to new events being numerically generated in no-rain regions. To address both these issues, conditioned log rain rate fields are generated by fitting minimum bending energy surfaces to the measured log rain rate fields. Log rain rates above the threshold are considered to be known to a small relative error. Measurements at the threshold are treated as a maximal constraint i.e. it is only known that the actual log rain rate is below the threshold value. The minimum bending energy surface consistent with all these constraints is used for interpolation. The effect of this is two fold. The smooth extrapolation beyond the threshold isohyet yields plausible decay of rain rates at the edges of events. Regions near rain events have a chance of yielding measurable rain rates in the interpolated field but regions far from rain events, or near rain events with sharp transitions (e.g. convective storms), have a much smaller chance.

8.2 Advection

The horizontal movement of rain fields by the ambient wind field, known as advection, is not described by the FBf model. Before interpolation, advection between consecutive scans needs to be removed. If it is not then interpolation does not yield a smoothly advecting and evolving rain event. Instead a rain event at the earlier location dissipates and disappears and a new rain event appears in the later location. This artifact looks artificial in rain field animations and would lead to errors when calculating rain fade time series on links.

Advection is assumed to be a linear translation between radar scans. This assumption would not be valid for large areas or long inter-scan times but is reasonable for the CRIE data. The rain field advection vector varies between events and over time. Thus advection needs to be estimated between each consecutive pair of scans. In both 2D and 3D interpolation, the speed with which the rain fields were being advected is calculated by finding the linear displacement that maximises the correlation between successive rays and scans respectively.

Consider two rain fields measured 10 minutes apart. The advection between the measurement of the rain fields $R_1(\mathbf{x})$ and $R_2(\mathbf{x})$ is estimated by identifying the two-dimensional lag $\mathbf{y}$ that maximises the cross-correlation i.e.

$$\mathbf{y}_A = \max_{\mathbf{y}} E\left(R_1(\mathbf{x}+\mathbf{y})R_2(\mathbf{x})\right) \tag{8.2.1}$$

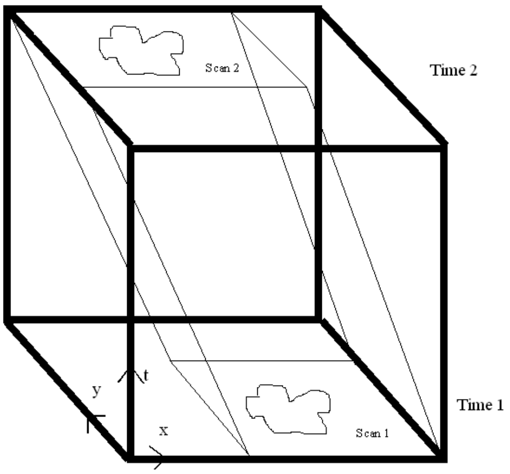

Figure8.2.1. Demonstration of 3D interpolation with advection removal

Before interpolation, rain field 1 is space shifted to remove advection i.e. $R_1(\mathbf{x}) \leftarrow R_1(\mathbf{x}+\mathbf{y})$. Spatial cross-correlation is now maximised with zero lag and rain events are seen to evolve without movement when radar scans are animated. Interpolation then reproduces the statistical fluctuations expected due to rain event evolution. After interpolation, advection is reintroduced i.e. $R_1(\mathbf{x}) \leftarrow R_1(\mathbf{x}-\mathbf{y})$. The scans at intermediate times, introduced by interpolation, are space-shifted by a multiple of $\mathbf{y}$ that decreases linearly to zero as the time of the second scan is approached. Figure 8.2.1 illustrates how interpolation is performed on a parallopid defined by regions of interest in consecutive scans that are maximally correlated by a zero length lag.

8.3 Disaggregation the CRIE Data

For network simulation we require the sampling volume of the numerically enhanced rain rates to be comparable to the diameter of a radio link. As a first approximation this diameter is equal to the width of the first Fresnel zone. Depending on the length and frequency of the link, this width can vary between a fraction of a metre to tens of metres. In Chapter 7, Deidda's multiplicative cascade disaggregation algorithm was introduced. The algorithm can be used to disaggregate rain fields to arbitrarily small integration volumes. The limit is constrained by the availability of data for calculation of the scaling exponents and for verification. For this thesis, scaling exponents have been extrapolated from the minimum measured scale i.e. diameters of 300 m. This is partially justified by comparison with the scaling moments of point rain rate measured by rain gauge, see Chapter 5. These show a scaling interval from 200 s down to 10 s. Using Taylor's approximation, this corresponds to a scaling region from 3 km down to 150 metres. The lower limit is not an identified scale break but the limit of measurement resolution. This implies that the disaggregation algorithm is justified down to regions of this diameter and probably much smaller.

A choice needs to be made as to what order disaggregation and interpolation are to be applied. Numerically these operations can occur in either order or interleaved. However, 3D spatial-temporal disaggregation has been identified as a difficult problem by Deidda and others. Furthermore, most literature considers the disaggregation of temporal averages rather than the instantaneous samples used in this thesis. In general, the disaggregation of an instantaneous spatial average cannot be performed in isolation from the disaggregation of other samples made close in time. For example, two radar derived rain rates made over the same sample volume only a few seconds apart could not be disaggregated independently, as a fine-scale high rain rate produced in the disaggregation at the first time would be correlated to a high rain rate at the second time. For the independent disaggregation of two rain rate fields to be valid, they need to be sufficiently separated in time. For the CRIE data, we assume the independence of variation at scales below the radar spatial sampling scale, $\Delta_x = 300$, on consecutive scans measured $\Delta_t = 10$ minutes apart. This will be true as long as $\Delta_x / D_x << \Delta_t / D_t$, where D_x and D_t are the spatial and temporal decorrelation distances. This allows each measured radar scan to be disaggregated independently.

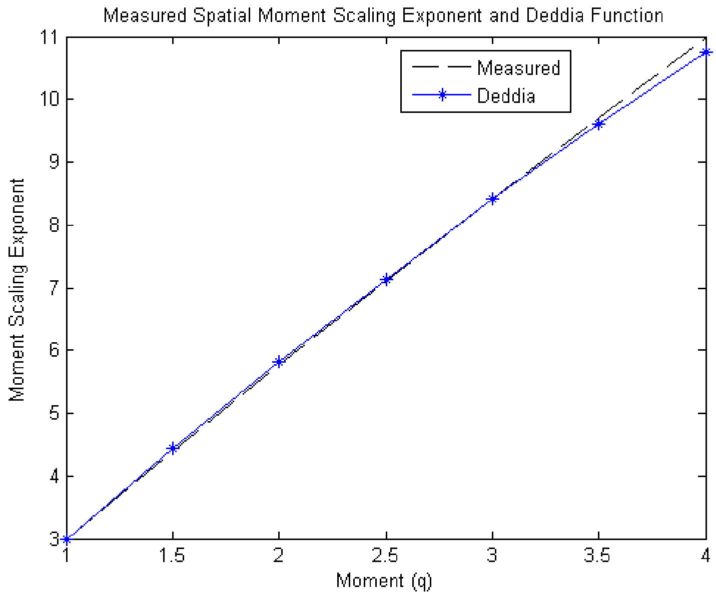

Figure 8.3.1 Comparison of measured spatial moment scaling exponents and best fit Deidda function

The multi-fractal exponent $\zeta(q)$ is estimated by linear regression of the structure function $S_q(\lambda)$ versus scale λ (from $\lambda = 300m \sim 1km$) in the log-log plot figure 5.4.3 and 5.4.7, also Paulson and Zhang (2007). They are presented in table 8.3.1. Sample multi-fractal exponents are used to estimate the two log-Poisson parameters c, β and hence to derive a. The cascade scaling exponents are within the error ranges of the measured exponents for combinations of parameters spanning 5 orders of magnitude, and so comparisons with other published parameters are unhelpful. Figure

8.3.1 is a plot of measured spatial moment scaling exponents and the best fit Deidda function.

$q=1.5$	$q=2$	$q=2.5$	$q=3$	$q=3.5$	$q=4$	c	β	a
4.40	5.78	7.12	8.42	9.71	10.99	10	1.115	-1.15

Table 8.3.1 Results of the multi-fractal analysis on measured radar data set.

The CRIE radar scans have been disaggregated by a factor of eight using three iterations of the Deidda method i.e. each 300 m by 300 m voxel has been replaced by an 8 by 8 array of voxels, each with a diameter of 37.5 m. Figure 8.3.2 compares the exceedance distribution of rain rates on measured scans with those generated by the disaggregation. This illustrates that disaggregation has increased the variance of rain rate by introducing higher values in a controlled way. Figure 8.3.3 is a comparison of spatial moment scaling structure function between measured radar data and disaggregated radar data. The algorithm can be seen to conserve the mean ($q=1$) while the variance ($q=2$) has increased in a way consistent with the measured data. Higher moments have also increased in a plausible way.

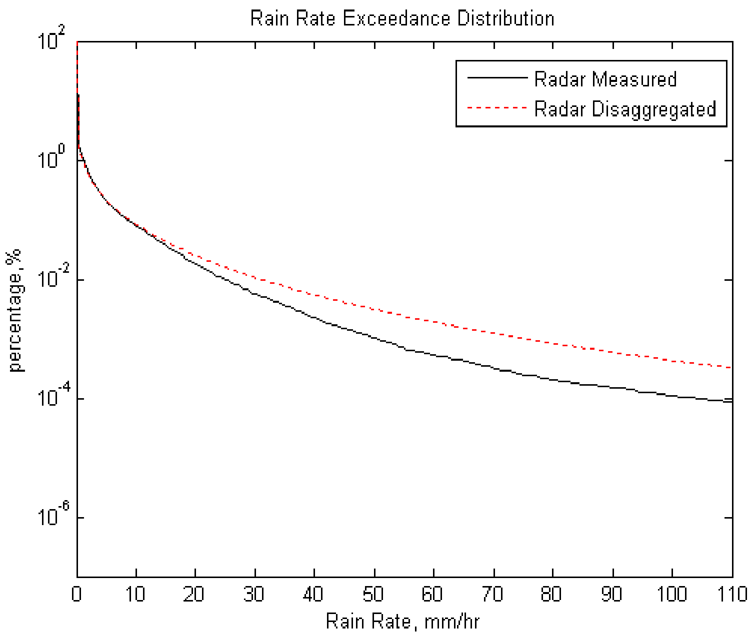

Figure 8.3.2 Comparison of the percentage of time that abscissa rain rates are exceeded from the measured and disaggregated radar rain rate data

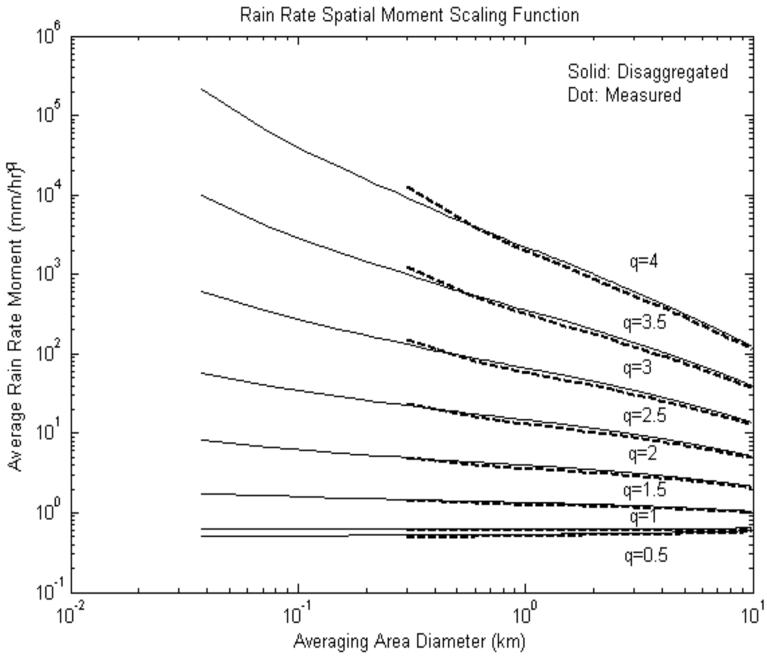

Figure 8.3.3 Spatial moment scaling structure function of measured radar data and disaggregated radar data

8.4 Disaggregation and Interpolation of Radar Data

The ARMD algorithm has been successfully tested on numerically generated FBfs and synthetic rain rate fields generated using the Callaghan model. However, the interpolation and disaggregation of real measurements are a more challenging test due to the issues highlighted in section 8.1 i.e. inhomogeneity, advection, rain intermittence and systematic measurement error.

To generate fields for network simulation, a combination of disaggregation and interpolation has been used. Rain fields have been disaggregated in three iterations of cascade by a factor of 8 to a spatial averaging over squares of diameter $\Delta_x = 37.5\,\text{m}$. Six iterations of the ARMD algorithm has then reduced the radar sampling time to $\Delta_t \cong 9.375\,\text{s}$. The algorithm can be summarised in the following six steps:

1. Disaggregate measured rain rate fields using Deidda's algorithm.
2. Estimate and remove the advection between the two measured rain rate fields.
3. Calculate log rain rate over the analysis regions.

4. Calculate the relative spatial and temporal scales.
5. Interpolate scans using AMRD algorithm
6. Re-introduce advection.

Before the process above can begin the radar derived rain rates are interpolated onto a regular Cartesian grid. There are excellent reasons not to do this, as discussed in Section 5.3 i.e. the interpolation of spatially varying averages of an inhomogeneous stochastic process without effecting the statistics is a problem worthy of a thesis in its own right. However, all the subsequent processes are made vastly easier if samples are regularly spaced. To reduce the variation of statistics with range, only a subset of the radar data was used between ranges of 20 and 60 km.

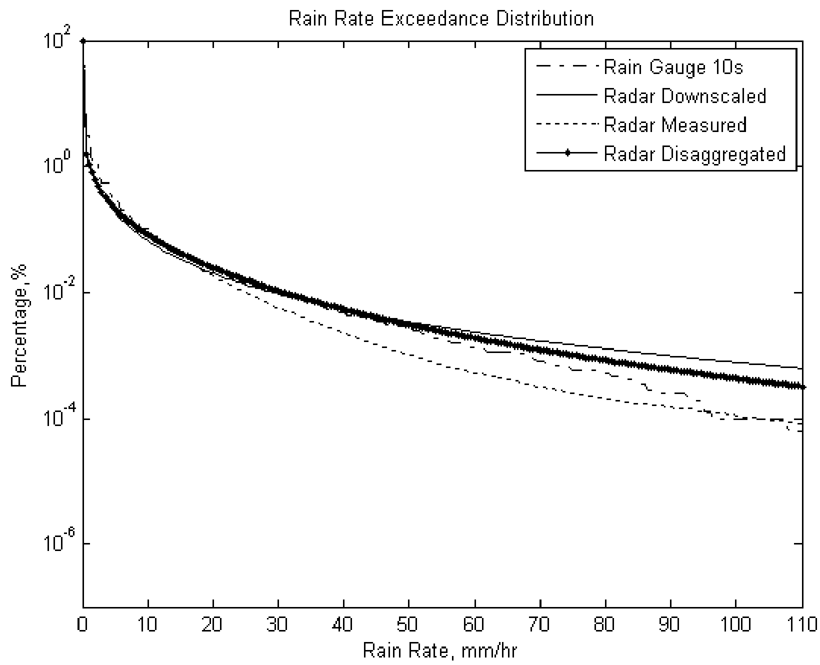

Figure 8.4.1 Comparison of the percentage of time that abscissa rain rates are exceeded from the measured radar rain rates (dot), the disaggregated rain rates (thick), the downscaled rain rates (solid) and 9 gauge years of gauge data (dash)

Figure 8.4.1 compares the marginal rain rate exceedance distribution at several stages in the algorithm. The disaggregation has increased in incidence of heavy rain as described in Section 8.1. This leads to higher exceedance probabilities for more intense rain. Interpolation has largely conserved the disaggregated distribution, as it is designed to do. The distribution differences are due to multimodal distribution in some scans. Some scans contain more than one rain event and so the distribution of rain rates is multi-modal. This leads to over-estimation of the variance of log rain rate and hence more extreme values being introduced by interpolation. The downscaled rain rates are largely consistent with those measured by rain gauge. Some variation is to be expected, particularly at very low exceedance probabilities, due to the different years spanned by the radar and gauge data. Although the CRIE contains 3199 radar scans, these cover only ~800 events.

8.5 Quantile function and Moment Scaling

8.5.1 Temporal Moment Scaling

Figure 8.5.1 illustrates the quantile functions for radar rain rate data after 3D interpolation compared with 9 gauge-years of rain rate measurements, for integration times from 10 seconds to 5 minutes. For 10 s integration and probabilities approaching 1 i.e. $1-p \to 0$, the quantile function approaches linearity in $\ln(1-p)$. The quantiles for lower probability are defined by few samples, thus are not reliable. Interpolation appears to conserve the original quantile functions over a range of integration periods.

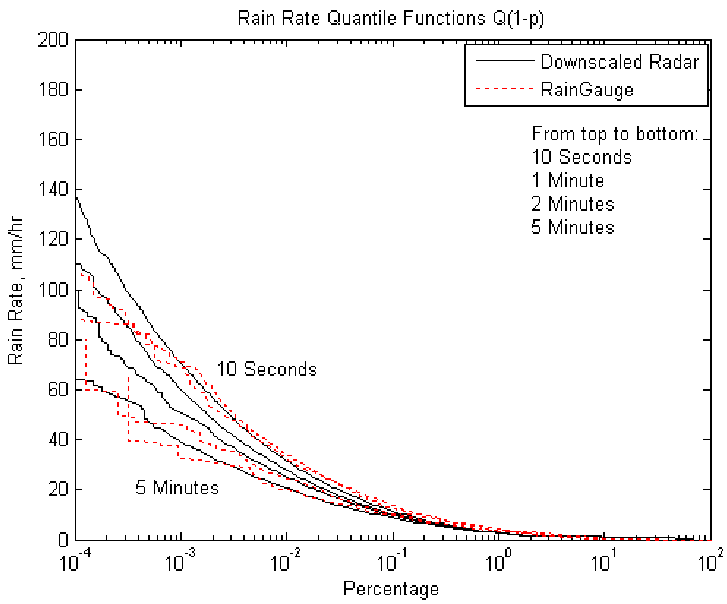

Figure 8.5.1 Simulated rain rates exceeded with probability $1-p$ for different

integration periods

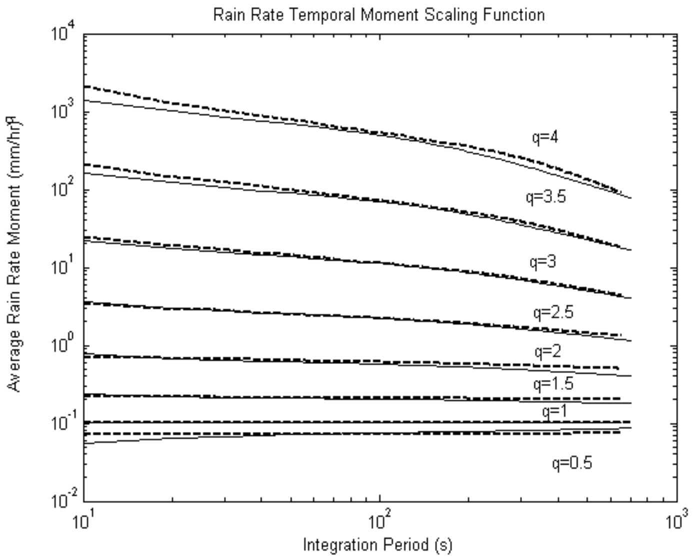

Figure 8.5.2 Moment scaling structure function for interpolated CRIE data and averaged 9 gauge-years rain gauge data (temporal modeling)

Moment scaling analysis is performed on the derived time series with increasing integration times. Each spatial point yields a time series from which the temporal moment scaling function can be calculated. Figure 8.5.2 shows a plot of the average moments $\left\langle [P_{\lambda,\lambda,\tau}(x,y,t)]^q_{\lambda=const} \right\rangle$ (i.e. structure function $S_q(\tau)$) against τ for values of q between 0.5 and 4 with a step 0.5 both for radar data and 9 years rain gauge data. Despite the radar and rain gauge data being acquired over different years, there is remarkable agreement between the two results.

8.5.2 Spatial Moment Scaling

Figure 8.5.3 illustrates the quantile functions for radar rain rate data after 3D interpolation compared with measured CRIE data, for integration diameter from 300 m to 4.8 km. The quantiles for lower probability are defined by few samples, thus are not reliable. It can be seen that after interpolation, the initial properties are conserved.

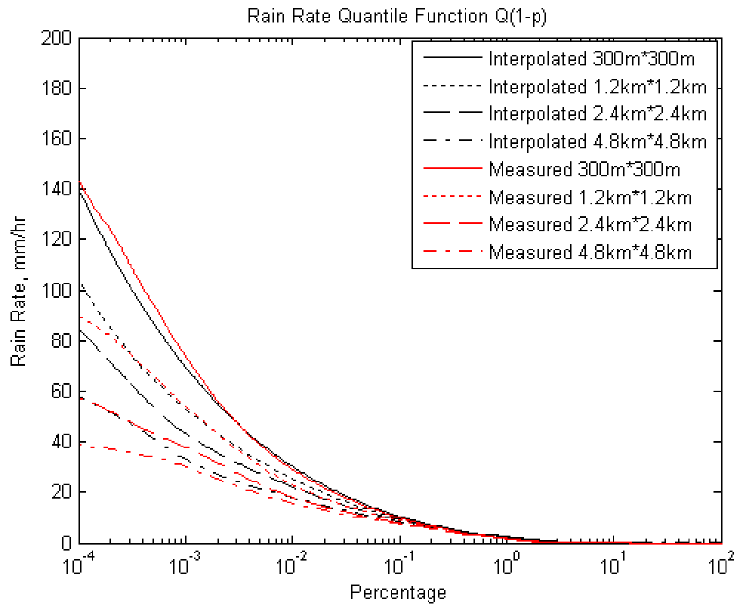

Figure 8.5.3 Simulated rain rates exceeded with probability $1-p$ for different spatial integration volumes

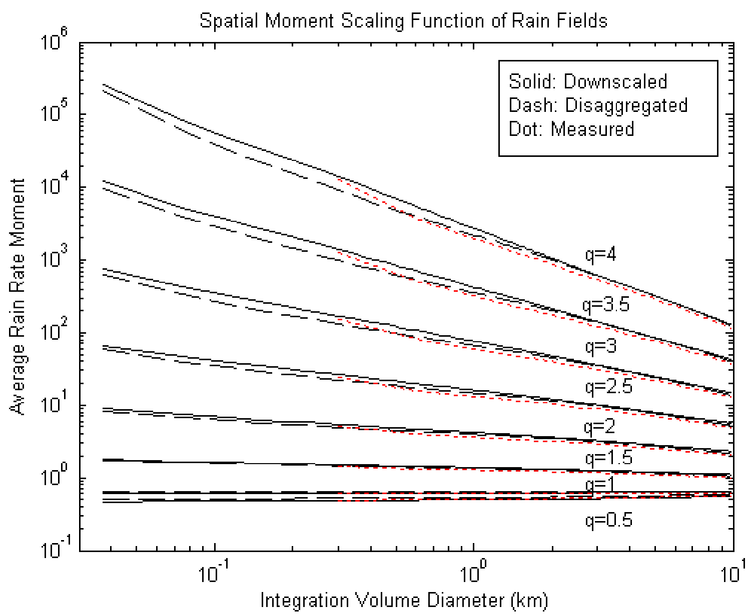

Figure 8.5.4 Moment scaling structure function for measured (dotted), disaggregated (dashed) and downscaled CRIE data (solid)

Moment scaling analysis is performed on the derived rain rate series in each scan with increasing integration diameter. Figure 8.5.4 illustrates a plot of the average moments $\left\langle [P_{\lambda,\lambda,\tau}(x,y,t)]^{q}_{\tau=const} \right\rangle$ (i.e. structure function $S_q(\lambda)$) against voxel diameter λ, for values of moment order q between 0.5 and 4. Curves are plotted for the original

CRIE data, disaggregated rain rates and downscaled rain rates. The voxel diameter λ has values ranging from 37.5 m to 10 km. Disaggregation has conserved the original moments from the measured scale $\lambda = 300\,\mathrm{m}$ up. At shorter scale the moments have been extrapolated in a plausible way. Interpolation has largely conserved the moments. The interpolation is designed to conserve the $q = 1$ and $q = 2$ moments. The higher order moments are largely determined by these.

8.6 Summary

A method has been developed to disaggregate and interpolate time-series of rain fields measured by rain radar with inter-scan periods as long as 10 minutes to yield time-series with sample periods as short as 10 seconds. The spatial resolution has also been disaggregated from 300 m to 37.5 m. The method has been applied to a database of radar derived rain fields from CAMRa, at Chilbolton in the UK. Interpolation has been shown to preserve the rain rate distribution and moment scaling of spatially averaged rain rate data. Furthermore, the interpolated and disaggregated data have reproduced the moment scaling of temporally averaged rain rate data measured from rain gauge.

CHAPTER 9 FADE MODELING

Once spatial-temporal rain data has been numerically generated from the coarse-scale measured data, they can be used for microwave network simulation. Heterogeneous networks of any geometry and of any radio parameters can be over-laid onto the fine-scale rain fields. Rain rates may be converted to specific attenuations at the relevant frequencies using the power-laws of Rec. ITU-R P.838-2. Instantaneous joint rain fade may be calculated by pseudo integration of the specific attenuation along the path of each link. Joint rain fade time series may be calculated by repeating this for each rain field.

For individual links, or collinear networks, the process described above requires rain rates restricted to a line. This can be achieved using a single scan line of radar data. This yields a large saving in computational effort with a few disadvantages. The major disadvantage is the inability to test different orientations to the prevailing wind. This parameter is largely ignored in ITU-R recommendations as the data has not been available to measure variation. However, using the full 3D downscaled (disaggregated and interpolated) dataset, the strength of orientation effects can be tested.

9.1 Fade Modeling Based on 2D Interpolation

The radar rain rate data (one ray data with 3199 scans) is interpolated to a time series with 9.375 s time resolution and 150 m space resolution by using 2D method presented in Chapter 6. In this section, these simulated data will be used to generate fade time-series on individual links. Summarising statistics will be compared to measurements and accepted models.

9.1.1 Attenuation Statistics

In this section, the average annual attenuation statistics for simulated links of 2 km and 10 km lengths are estimated using the radar data. These are compared with the Rec. ITU-R P. 530-12 model. Further validation is supplied by a comparison with two-years of measured link attenuation data at 38 GHz with a path length 3 km and a time resolution 1 minute measured close to Chilbolton. Higher order statistics are also compared. In addition, six-months of measured link attenuation data at 38 GHz with a path length 5.5 km and a time resolution 1 second is also compared.

9.1.2 Marginal Rain Rate Distribution

One ray of radar data is downscaled to have a time resolution of 10 s and a space resolution still 150 m. This time series is integrated to 1 minute sampling. The figure 9.1.1 shows the downscaled rain rate exceedance distribution and compares it to the Rec. ITU-R P.837-5 prediction based on a 0.01% exceeded rain rate of $R_{0.01} = 30$ mm/hr .

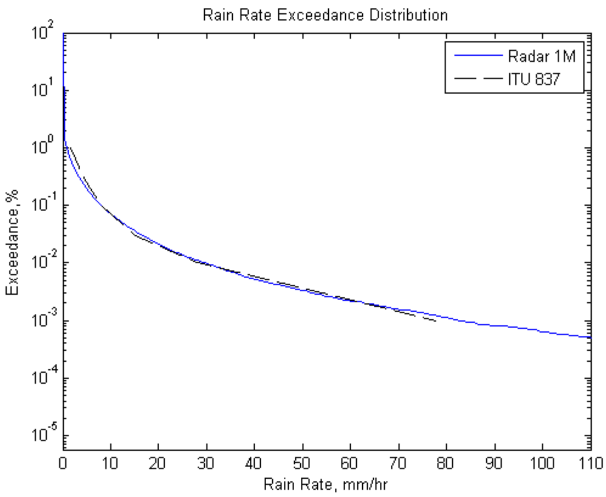

Figure 9.1.1 The one-minute radar rain rate exceedance distribution compared with the Rec. ITU-R P.837-5 prediction using $R_{0.01} = 30$ mm/hr

9.1.3 Marginal Rain Fade Distribution

Figure 9.1.2 shows a schematic description of how terrestrial links of a specified length 'd' are superimposed onto the PPI data. The terminals are positioned either along the radar rays or along a line tangential to the scan centre. In each case, all radar data cells traversed by the simulated link are identified and for each of these cells, the specific attenuation, γ_R, for the required frequency is obtained from the rain rate by using the relation: $\gamma_R = kR^{\alpha}$ (dBkm^{-1}), where parameters of k and α are identified in ITU-R Rec. 838.

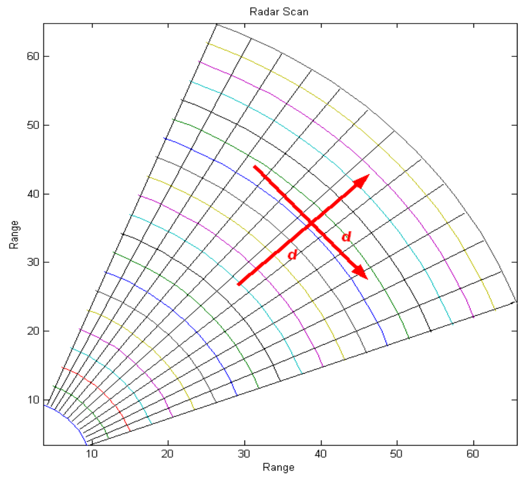

Figure 9.1.2 Examples of two terrestrial links superimposed on the PPI data

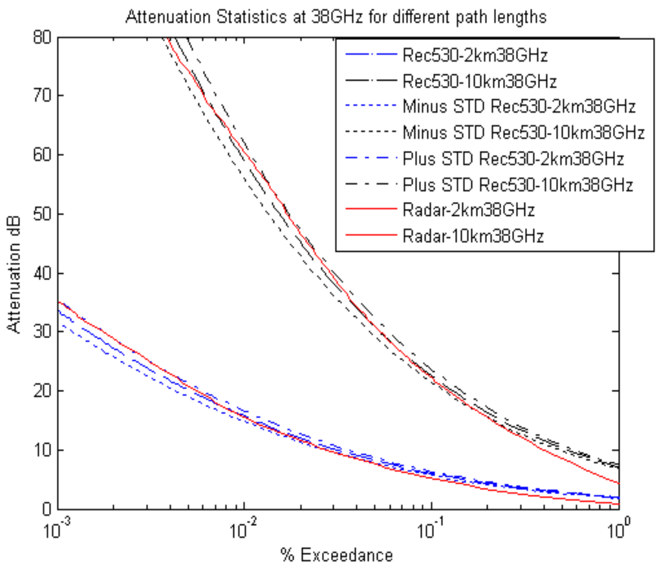

Figure 9.1.3 38 GHz attenuation statistics for 2 km and 10 km path lengths from radar simulation (solid) and ITU-R Rec. 530, using $R_{0.01} = 30$ mm/hr . Model confidence intervals are also plotted (dotted, dashed)

Having obtained γ_R for each of the radar data cells along the simulated link, the total attenuation was determined by multiplying γ_R by the length of the link segment contained within the data cell and summing this quantity over the link length (J.W. F. Goddard and M. Thurai, 1996).

Using the methods described above for a single scan line, attenuation statistics are generated for path length 2 km and 10 km at 38 GHz. The results are compared with ITU-R Rec. 530-12, using $R_{0.01} = 30\ \text{mm/hr}$, and are shown in figure 9.1.3. The dotted and dash-dot lines indicate confidence intervals, based on estimates of year-to-year variation. These are rain attenuation exceedance curves associated with 0.01% exceeded rain rates one standard deviation either side of the mean. The population standard deviation of $\sigma = 1.9 mm/hr$ was calculated from 482 complete station-years of data from 42 meteorological stations spanning ITU-R Rec. P.837-5 Rain Zone F and the Adjustment Factor (AF) postulated by Prof. Peter Watson for the conversion between the hourly to one-minute rain rates exceeded 0.01% of the time, of AF = 2.7.

9.1.4 Comparisons with Measured Real Link

For further validation, link rain fade statistics derived from the 2D interpolated rain rates are compared with statistics of fade measured on real links. Although these comparisons are necessary as rain fade predictions are the ultimate deliverable of the proposed simulation method, it is very difficult to specify when differences between simulated and measured statistics are significant. There are many reasons for these differences. Real links experience attenuation due to many processes other than rain fade e.g. multi-path, ducting, atmospheric attenuation, variable obstruction, other hydrometeor effects e.g. sleet, fog and antenna wetting; interference by animals (spiders, birds, insects) or/and plants to the equipment as well as human interference during maintenance and equipment failure. The proposed simulation method does not aim to mimic any of these processes. Even if rain fade could be isolated from all other mechanisms in real link attenuation time-series, differences in statistics would still be present due to random differences in the simulated and actual rain. Given arbitrarily long periods of both simulation and measurement it is hoped that the statistics would converge but this is impossible to guarantee given limited knowledge of actual rain statistics. In the comparisons below both the simulation data and measured data are very limited. The CRIE data base contains rain information for only 2/3 of a year (acquired over two years). The link data is from a few years at most. Currently there is no accepted method to tell when the first order statistics of rain are significantly different between two periods of such short duration. Certainly no methods exist for higher order statistics or statistics of rain fade.

Two-years of attenuation data from a 3 km, 38 GHz link, with a time resolution 1 minute, measured close to Chilbolton is used to compare with radar. The data has had a daily reference level estimated and removed. This compensates for many of the slowly varying fade processes. Figure 9.1.4 illustrates attenuation statistics generated for the link. The shift between real link and radar attenuation statistics is probably due to residual errors in the reference level estimates. Attenuation is derived from monitoring the automatic gain control (AGC) at the receive end of the link. For this system the AGC reached a maximum gain at an attenuation of 40 dB and so the measured attenuation distribution flattens off at this level.

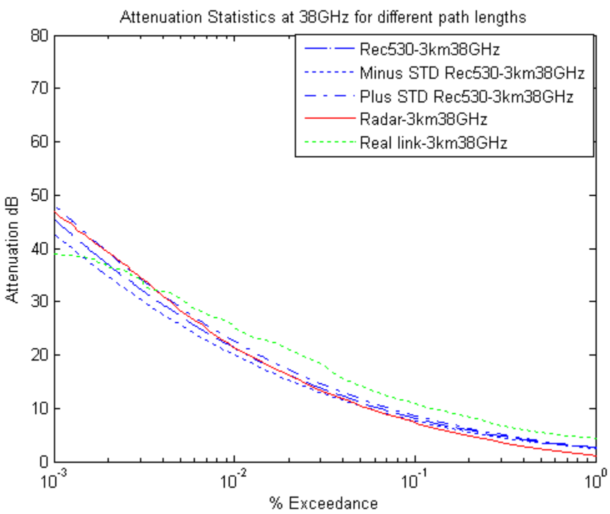

Figure 9.1.4 Measured, one-minute attenuation statistics for a 3 km, 38 GHz link

compared with predictions derived from 2D radar simulation and ITU-R Rec. P.530-12, using $R_{0.01} = 30$ mm/hr

In order to verify the second order temporal statistics yielded, it is required to compare the temporal autocovariance function of real and predicted rain fade time series. Real data include many effects other than rain fade. For real data, as it rains only 5% of the time, there is a chance that the smaller fluctuations that occur 95% of the time may have a large effect on autocovariance. A threshold of 3.5dB is set i.e. all values smaller than 3.5dB is converted to zero. For comparison, the same threshold is set for the simulated data. Figure 9.1.5 illustrates the autocovariance of attenuation from radar and real link.

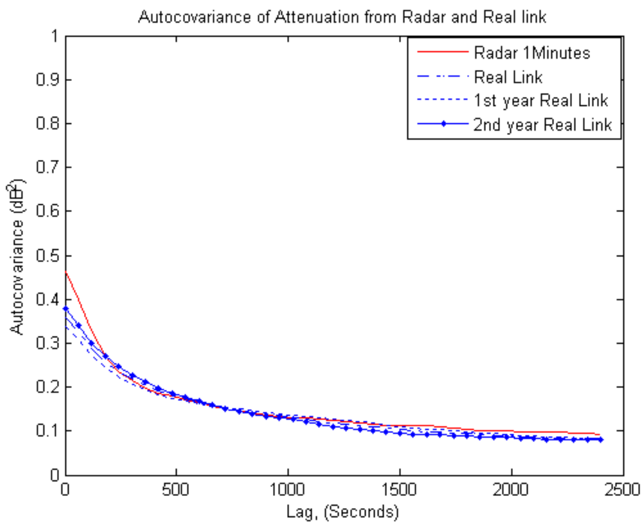

Figure 9.1.5 Temporal autocovariance function for 1-minute accumulations of the measured real link attenuation (38 GHz, 3 km) compared to the result predicted by simulation

It can be seen from figure 9.1.4 that the real link attenuation is always several dB larger than radar attenuation. This leads to the different variance (when lag is zero) between the real link and simulation results in figure 9.1.5. The difference has several possible explanations. Firstly, during the rain, although the rain effects dominate, the path clearance effects may still be present. Secondly, there is likely to be poor sampling of convective events in the single ray considered. Convective events are typically only a few kilometres across and so a single ray will sample only a fraction of those in the data base. This is likely to lead to large variation between results from different scan lines.

A second 38 GHz link with a 5.5 km path was monitored for six months and attenuation recorded with a one-second integration period. The measured one-second link attenuation data has been accumulated to generate 10 seconds attenuation time series. Figure 9.1.6 illustrates the 10 s attenuation statistics compared with the one-minute statistics predicted by Rec. ITU-R P.530. The measured attenuation plateaus due to the AGC limit. Figure 9.1.7 illustrates the autocovariance of attenuation with a time resolution 10 seconds from radar and real link.

The simulated autocovariance is similar to the measured curve but has an implausible wobble. This is almost certainly due to poor sampling statistics in the 2D interpolation of a single scan line.

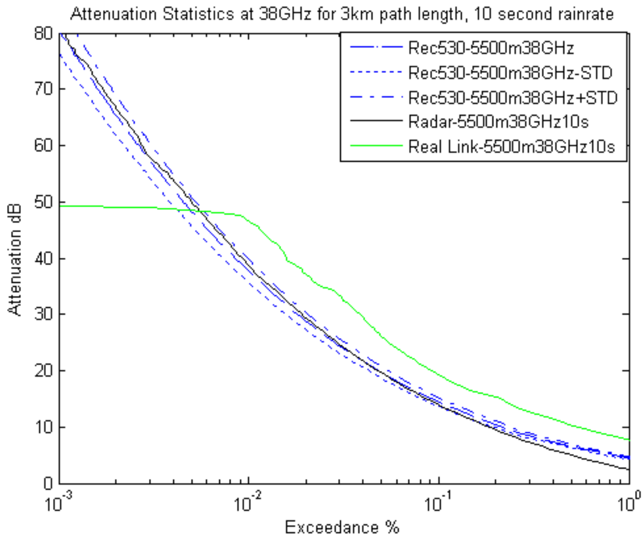

Figure 9.1.6 Ten-second attenuation statistics for a 5.5 km, 38 GHz link compared with ITU-R Rec. P. 530-12 predicted one-minute statistics based on a 0.01% exceeded rain rate of 30 mm/hr, and the prediction of the network simulator using a single scan line

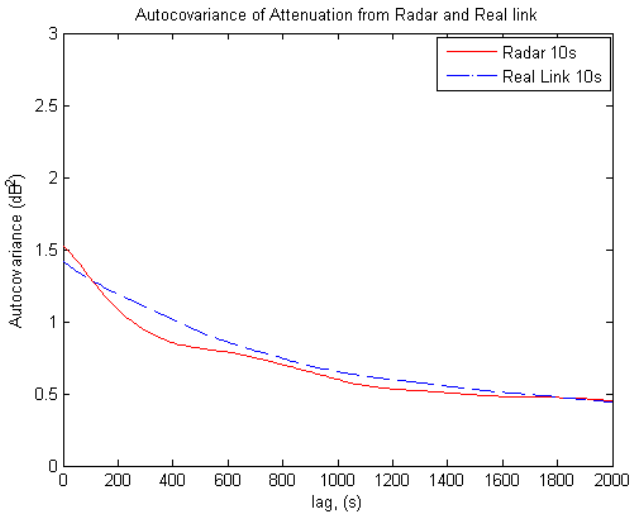

Figure 9.1.7 Temporal autocovariance function for 10-second accumulations of the measured real link attenuation and 2D network simulation at the 5.5 km scales

9.1.5 Summary

The 2D interpolation of radar data derived from a single ray appears to be able to predict the first and second order statistics of individual links (or collinear link networks) to promising accuracy. However, the 2D algorithm produced anomalous results. These anomalies were addressed in the 3D algorithm. The results from 3D disaggregation and interpolation are described in next section.

9.2 Fade Modeling Based on 3D Interpolation

The temporal rain rate data derived from the radar, with a sampling interval of 10 minutes and spatial time resolution of 300 m, has been downscaled to a sampling interval of 9.375 s and spatial resolution of 37.5 m. In this section, these fine-scale rain rate maps will be used to predict the average annual statistics for a range of 38 GHz microwave links. These will be compared to statistics derived from measurements on real links and with ITU-R model predictions.

9.2.1 Attenuation Compared with Measured Real Link

Figure 9.2.1 illustrates the average annual fade statistics for 38 GHz links of length of 1 km, 5 km and 10 km. Simulation results are plotted using the original radar derived rain rate fields, the downscaled rain fields and Rec. ITU-R P.530-12 for a 0.01% exceeded rain rate of 30 mm/hr. This shows excellent agreement between simulation results and the ITU-R model down to exceedance probabilities of 0.05%. The simulation results are for 10 s statistics while the ITU-R model yields 1 minute averages. This should lead to bias in the comparison where the simulation results would yield more intense fades. However, below 0.05% of time the statistics for the longer links deviate from the ITU-R model. This may be due to the event sampling statistics i.e. the CRIE data may lack a representative selection of intense events with large spatial extent.

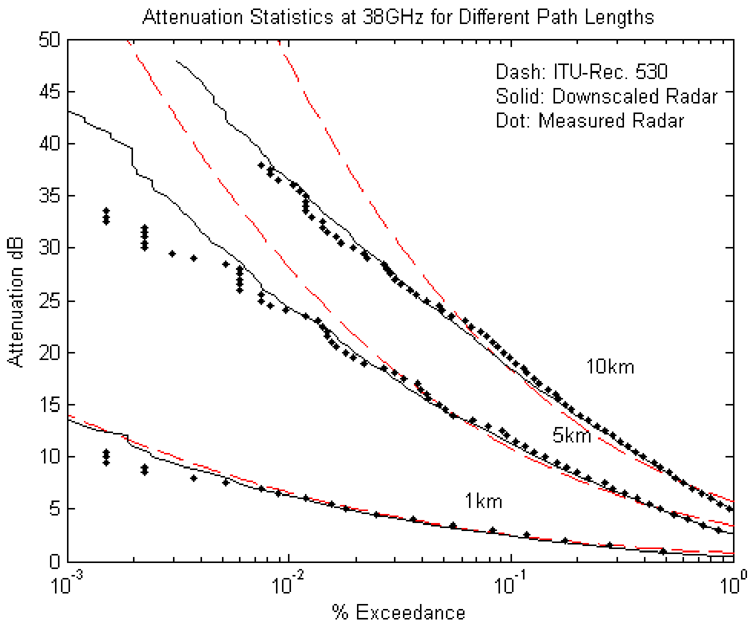

Figure 9.2.1 Simulated attenuation statistics for 38 GHz links of length 1 km, 5 km and 10 km using CRIE data (dotted) and downscaled data (solid), compared with Rec. ITU-R P.530-12 using $R_{0.01} = 30$ mm/hr (dashed)

For further validation, a 38 GHz link with a 5.5 km path was monitored for six months and attenuation recorded with a one-second integration period. The real link attenuation data with a time resolution 1 second is accumulated to generate 10 seconds attenuation time series. The attenuation distribution calculated from interpolated radar data, real link and ITU-R Rec. 530 model is shown in figure 9.2.2. The flat curve around 50dB for real link attenuation distribution is due to the AGC limit. The measured link data contains large uncertainties due to the restricted period of data collection. The results could be quite different if a different 6 month period was used due to seasonality and general sampling statistics. The simulated results appear to underestimate the intensity of events at the 0.005% exceedance level, compared to both the measured link data and the ITU-R model.

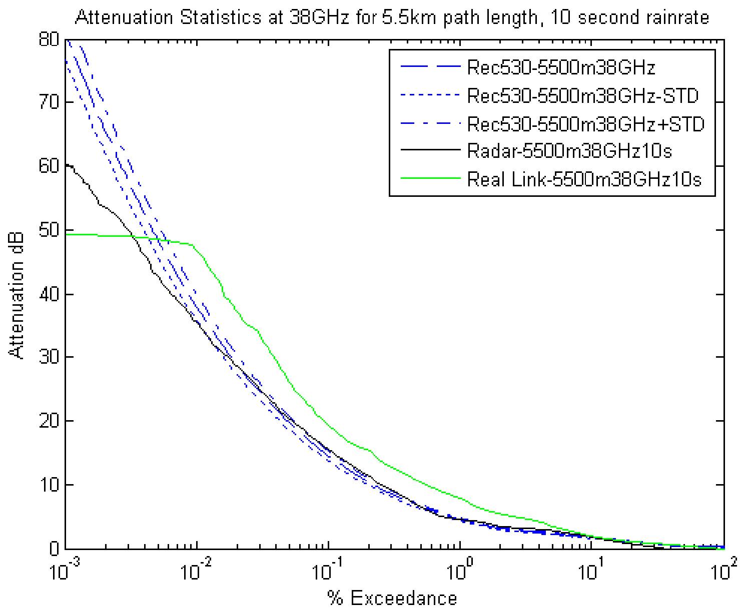

Figure 9.2.2 Measured 10-second, attenuation statistics for a 5.5 km, 38 GHz link (grey) compared with predictions derived from radar simulation (black) and ITU-R Rec. P.530-12, $R_{0.01} = 30$ mm/hr

Two-years of attenuation data from a 3 km, 38 GHz link, with a time resolution 1 minute, measured close to Chilbolton is used to compare with radar. The data has had a daily reference level estimated and removed. This compensates for many of the slowly varying fade processes. The radar attenuation data with a time resolution 10 second is accumulated to generate 1 minute attenuation time series. Figure 9.2.3 illustrates the measured and simulated attenuation exceedance statistics. In order to verify the second order temporal statistics, the measured and simulated temporal autocovariance function is compared in Figure 9.2.4.

Figure 9.2.3 shows excellent agreement between simulation results and measured link below exceedance probabilities of 0.01%. The autocovariance illustrated in Figure 9.2.4 also shows excellent agreement.

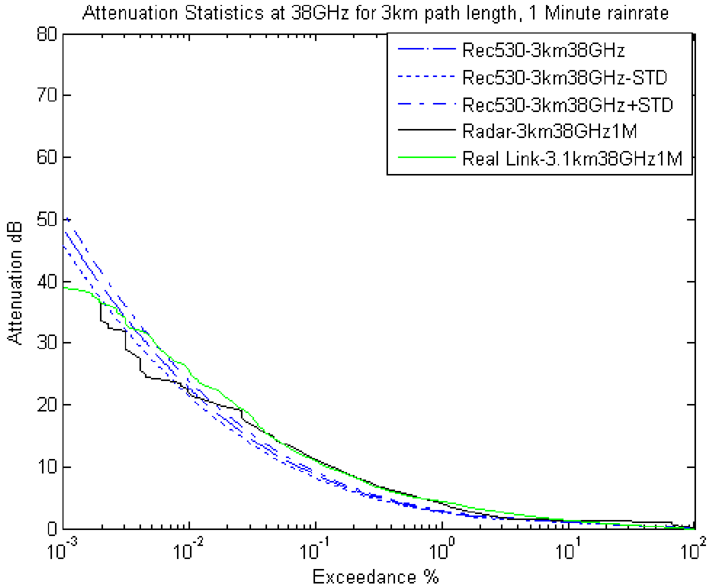

Figure 9.2.3 Measured one-minute attenuation statistics for a 3 km, 38 GHz link (grey solid) compared with predictions derived from radar simulation (black solid) and ITU-R Rec. P.530-12

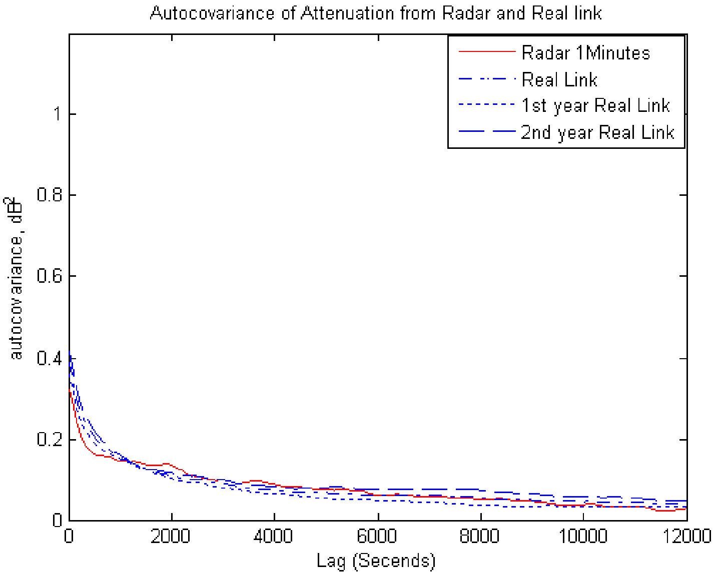

Figure 9.2.4 Temporal autocovariance function for 1-minute accumulations of the measured real, 38 GHz, 3 km link attenuation (dotted, dashed) and simulated radar attenuation (solid)

9.2.2 Summary

The numerically generated fine-scale rain field time-series described in Chapter 8 has been used to simulate the time-series of rain fade on a range of 38 GHz links. The average annual, first and second order summary statistics have been generated and compared to ITU-R model predictions and some real link measurements. Very encouraging results have shown that the method can be used to predict rain fade exceedance and autocovariance for individual links. Furthermore, fade duration statistics can be predicted. Differences at low probabilities are probably due to the sampling inherent in the CRIE database i.e. they are probably within the variation produced if the experiment had operated longer or for a different two year period. This chapter has focused on validation of the predicted fade time-series for individual links. Further work will apply the simulation techniques to networks of more than one link.

CHAPTER 10 FADE DURATION STATISTICS

The planning of radio communications systems requires an estimate of the average annual outage due to fading, which, at millimetric wavelengths, is generally dominated by the effects of rain attenuation. Links engineered for 99.99% availability experience outage for 50 minutes of an average year. However, the effects on systems are very different if this outage period occurs as a single 50 minute period or 50 periods of one minute. The Fade Mitigation Techniques (FMT) employed to counter the effects of these outages would be very different. For example, an outage of 50 minutes may be completely unacceptable and backup systems would be required where outages of a minute or so could be handled by introducing latency or buffering the data. Many systems take a significant period of time to restart communications after an outage, generally as the system has “lost lock” and receivers need to re-establish phase-lock and determine what data has not been successfully transmitted. For this reason, the number of very short outages is important. The design and implementation of FMTs require not only the knowledge of the annual long term attenuation statistics, but also of the dynamic characteristics of attenuation, such as rain fade duration, interfade intervals and fade slope. One of the criteria defining the quality of service is the probability of system being unavailable for a given time duration. Recommendation ITU-TG.821 (ITU, 1996) defines unavailable time as that where a link outage occurs for more than 10 consecutive seconds.

The average annual fade duration distribution, of which extensive measurements have been made for a wide range of fade thresholds, is of interest in the planning of communication systems. Fade duration distributions are frequently presented as conditional probabilities of fades exceeding certain durations, given that the fade has exceeded a chosen threshold. This distribution can also be presented as the number of fades exceeding certain durations, once the threshold is exceeded. This representation provides information on the number of outages and system availability due to propagation on links, given a fade margin and an availability specification.

In this chapter, the rain fade time-series of a 38 GHz, 9 km link are simulated. Then the derived fade duration model and the Rutherford Appleton Laboratory (RAL) model are compared.

10.1 Average Fade Duration

In Chapter 2, I introduced the RAL rain duration model for the number of events in an average year N, where the point rain rate exceeds R for a period greater than t_d:

$$N = 1.70 \cdot 10^4 R^{-1.76} \exp\left\{ -\frac{(\ln t_d - 2)^2}{3.86 - 0.0409R} \right\}.$$

This model had been adapted to provide an estimate of the number of rain fade events experienced by a link in an average year. This was accomplished by devising two transformations. The first related rain fade to a point rain rate with the same exceedance probability. The second associated a rain fade duration to the duration of that rain intensity at a point. These relationships were optimised to yield an expression which matched the measured fade duration statistics on a 38 GHz experimental link 9 km path near Chilbolton. The model is based on the rainfall rate R (mm/hr) which gives rise to a given path attenuation, A, from the expression $A = kR^{\alpha} \cdot d \cdot r(R)$ (dB); where k and α are constants obtained from ITU-R Recommendation P.838 and d is the path length in km. The path length reduction factor, r, was derived from the RAL model. For a given fade depth A, in dB, the appropriate point rainfall rate, R_A, can then be determined. Using this procedure, the model for rain rate durations was fitted to the 38 GHz fade data to yield the following expression for the number of fades N_A exceeding a depth of A dB and a duration of t_d seconds (Paulson and Gibbins, 2000 and Rec. ITU-R P.530-12):

$$N_A = 1.7 \cdot 10^4 R_A^{-1.76} \exp\{-\frac{[\ln(273R_A^{0.39} + (0.166 + 0.0194R_A)t_d) - 2]^2}{3.86 - 0.0409R_A}\}$$

The objective of the research has been to generate rain field time-series as an input into a general microwave link rain fade simulation tool. To test the ability of the system to predict temporal variation, we have simulated rain fade time-series of 38 GHz links of length 9, 5 and1 km, and compared the derived fade duration model to the RAL model, Paulson and Gibbins (2000) and Rec. ITU-R P.530-12, see Figure 10.1.1, 10.1.2 and 10.1.3. The RAL/ITU model uses a standard log-normal pdf to model exceedance distribution. A consequence is that the model becomes non-physical at short durations (around 10 s). However, the curves were originally only fitted to the number of durations longer than 30 s. For duration greater than 30 s with statistically significant numbers of events, the agreement is satisfactory. The RAL.ITU model appears to over-estimate the number of long duration events for the shorter links. The simulator predicts a large number of short events of 10 and 20 second duration. These are outside the range of the RAL model but are very important for FMT design. These results are consistent with measured fade duration distributions reported to Ofcom task groups. It is currently unknown how much variation is introduced by year-to-year variations. It is possible that the shape of the curves will remain but the total numbers will vary. The high attenuation curves are expected to vary more due to the lower probability of the extremes they describe.

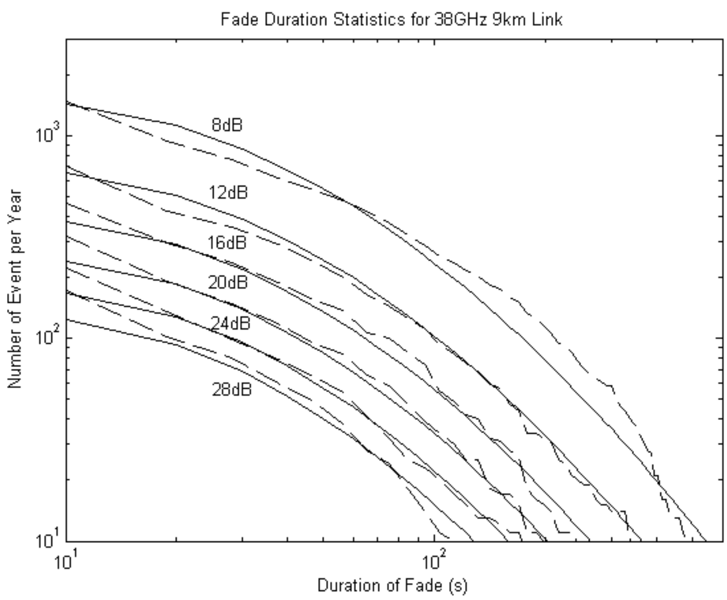

Figure 10.1.1 The RAL fade duration model predictions for a 38 GHz, 9 km link

(solid) compared to the fade durations of a simulated link using downscaled (disaggregated and interpolated) radar data (dashed). The curves indicate number of events in an average year for attenuations of 8, 12, 16, 20, 24 and 28 dB, from top to bottom

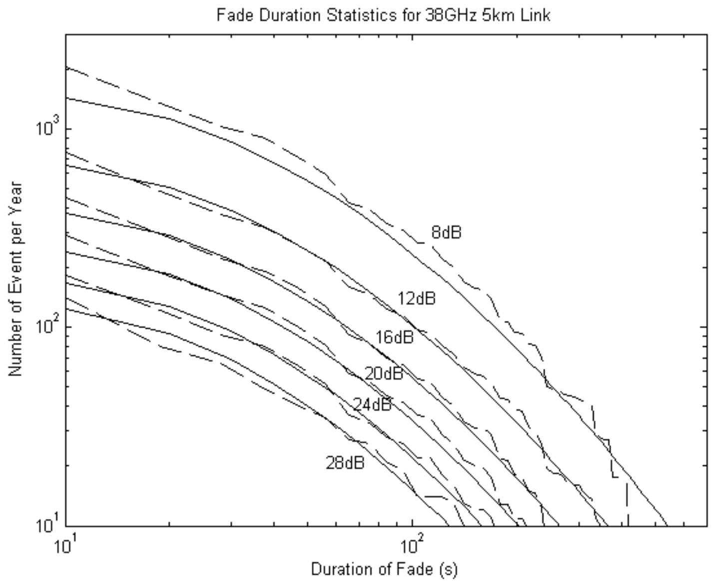

Figure 10.1.2 The RAL fade duration model predictions for a 38 GHz, 5 km link (solid) compared to the fade durations of a simulated link using downscaled radar data (dashed). The curves indicate number of events in an average year for attenuations of 8, 12, 16, 20, 24 and 28 dB, from top to bottom

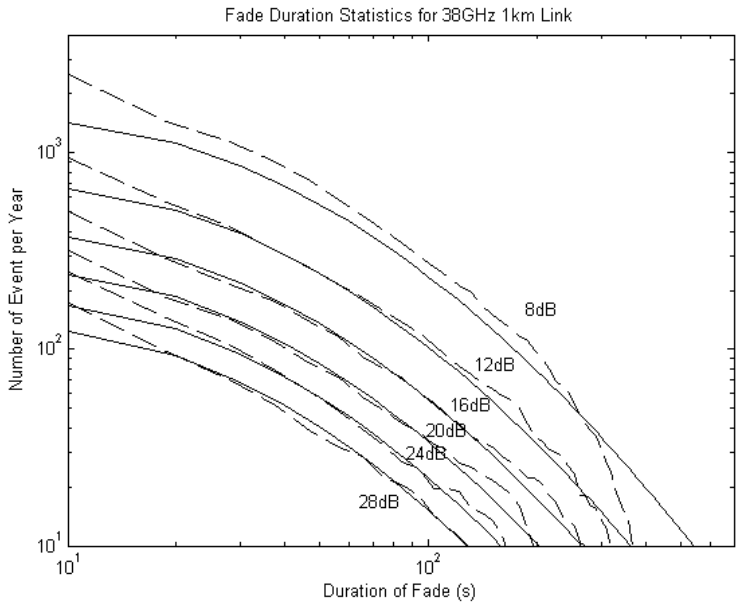

Figure 10.1.3 The RAL fade duration model predictions for a 38 GHz, 1 km link (solid) compared to the fade durations of a simulated link using downscaled radar data (dashed). The curves indicate number of events in an average year for

attenuations of 8, 12, 16, 20, 24 and 28 dB, from top to bottom

10.2 Summary

One of the criteria defining the quality of communication system is the probability of the system being unavailable for a given time period. It is therefore useful to determine not only the annual statistics of signal attenuation due to rain, but also the statistics of the rain fade durations. The downscaling method described in the Chapter 8 has been applied to simulate time-series of rain fade on a 38 GHz link and it has reproduced measured fade duration statistics. Simulated fade durations are consistent with the RAL fade duration model. They indicate the possibility that the RAL model over-estimates the number of long fade events on short links. The simulator results yield fade duration statistics for durations of 10 s compared to a shortest duration of 30 s provided by the RAL model. These results provide some validation of the usefulness of the simulator. It is likely that the simulator could provide fade durations experienced by complex networks i.e. route diverse or multi-hop links.

CHAPTER 11 CONCLUSIONS AND FUTURE OUTLOOK

The main objective of the work described in this thesis was the development of a simulation tool to predict joint rain fade time-series on arbitrary networks of terrestrial microwave links. This has been achieved. A major hurdle in the development of the simulator was the generation of time-series of fine-scale rain rate fields. A significant amount of effort has been exerted in the characterisation of fine-scale rain rate fields and the development and validation of numerical algorithms for the downscaling (disaggregation and interpolation) of these fields. In the process, analyses have been performed on rain fields that have never before been reported and some fundamental properties of rain rate fields have been observed. The resulting simulation tool represents a major step forward in rain fade modeling. Current internationally recognised fade models provide average annual distributions of one-minute rain fade averages on individual links. The simulator developed in this project yields joint rain fade time series of ten second averages for arbitrary networks of links. From these time-series, joint distributions can be calculated. In addition more complex statistics can be derived such as fade durations on arbitrary link networks.

The following sections summarise some of the important conclusions reached in earlier chapters. The final section described further work in this area

11.1 Summary of Conclusions

11.1.1 Rain Field Analysis

Multifractal statistics were identified as the most powerful and appropriate analysis tools for the characterisation of the stochastic properties of rain rate fields. The moment scaling and quantile scaling statistics had been calculated on rain rate time-series and rain fields before but never down to the fine scales reported in this thesis. In addition, three systematic errors were observed in the methods reported to have been used to calculate moment scaling statistics from rain fields derived from radar data. A method to calculate moment scaling statistics from rain rates averaged over a regular polar grid have been devised and tested. The improved method has been shown to yield significantly different moment scaling exponents.

The improved method was applied to radar data from the Chilbolton CAMRa radar in the UK and these were compared to statistics derived from 9 gauge-years of co-sited, rapid response rain gauge data. The resulting moments show smooth variation across the scales considered, 300 m to 10 km and 10 s to 6 hours. They are well approximated by two multi-scaling ranges with a scale break around 3 km or 200 s. The moment scaling function $\varsigma(q)$ is convex, which implies the field has a multi-fractal structure. The gauge data allowed analysis over a wider range of scales and another scale break was observed around 10000 s. The scale break at 3 km or 200 s becomes better defined at higher moment orders implying that it is present in intense rain. Intense rain occurs in small convective cells, typically with diameters in the range 4 to 8 km Harden *et al* (1974) and spacing 3 to 7 km, Veneziano *et al* (1996). The break at 2 km implies a finer structure within intense rain cells. Sinclair (1974) reports a scale break in the vertical wind velocity at 0.5 km, derived from penetrating flights through thunder storms. This should be observable in rain variation at integration times of 30 s and at the fine-scale limit of spatial scaling. However, this effect was not observed.

11.1.2 Downscaling of Rain Field

Once the stochastic variation of rain rate fields had been quantified, it was necessary to find numerical methods to downscale the fields to the fine scales necessary for radio link simulation. Rain field time-series derived from radar data is disaggregated in space but sampled in time and so different algorithms are required to increase the resolution in these dimensions. As an additional complication, radar derived rain rate fields include a systematic error due to the minimum measurable rain rate. The stochastic downscaling algorithms needed to be robust in the presence of this error.

The existing disaggregation algorithm due to Deidda has been used to refine the spatial resolution. This disaggregation has been constrained by extrapolating the moment scaling statistics measured on radar data, with the extrapolation justified by the smooth variation observed in rain gauge derived statistics over the comparable scale range.

Interpolation has required the development of a new algorithm. The Asymmetric Random Midpoint Displacement algorithm has been developed. It is an extension of Voss's Random Midpoint Displacement algorithm and is loosely modelled on the Local Area Subdivision algorithm of Fenton and Vanmarcke. The algorithm allows the interpolation of log rain rate at any point in space time, given arbitrarily placed existing samples in a surrounding interpolation volume. The method has been tested on numerically generated fractional Brownian fields.

Three characteristics of rain fields measured by radar needed to be addressed before these algorithms could be applied to them. Measured rain fields advected, were intermittent and were distorted by systematic errors in measurement. Methods were developed and tested to deal with all three of these effects. Combining these methods, Deidda's disaggregation algorithm and Asymmetric Random Midpoint Displacement allows the downscaling of rain field time-series to fine scales. The smallest scale possible is not limited by these algorithms but by the existence of rain measurements for verification. It is postulated that link rain fade data may be the best way to verify the downscaled rain fields.

The downscaling methods have been applied to rain field time-series derived from the CRIE database. The refined rain fields have a spatial integration diameter of 37.5 m and a temporal sampling interval of 10 s. The interpolated rain map time series is used to predict the rain fade distribution and fade duration statistics of a range of microwave links and these are compared to published ITU-R models. Results have shown that the method can be used to predict rain fade exceedance and autocovariance for individual links. Furthermore, fade duration statistics can be predicted.

11.2 Recommendation for Further Work

This section contains a few of topics identified in the course of this research project which the author feels are worth investigating in the future. These possible future projects either develop the simulation method further or apply the link simulation tool to current problems in microwave telecommunications engineering. Development project include reduction of the finest temporal scale down to one second, application of the methods to a different radar database and adaptation of the CRIE results to different climates. Current engineering problems include the evaluation of FMTs including Automatic Transmit Power Control (ATPC) and Dynamic Modulation (DM). Furthermore, a general rain Rain Fade Duration model could be developed.

11.2.1 Development of the Simulator

The current simulator uses rain fields downscaled to spatial averages of 37.5 m diameter and temporal sampling of 10 s. For QoS prediction it is desirable to reduce the sampling interval to one second. The algorithms can achieve this but the rain fields cannot currently be verified. Rain rate measurements with a one second integration time are required. These could be produced by vertically pointing Doppler radar measurements. A special instrument would be required which could measure at altitudes occupied by terrestrial links i.e. below 50 m. Instruments such as acoustic disdrometers currently under development could provide these data in the future.

This project used coarse scale rain field data derived form the CRIE database of radar measurements. This restricts the size of network that can be simulated to those with diameters less than 30 km. Other radar databases could be used and yield larger simulation areas. The Nimrod rain radar network, run the UK Meteorological Office, produces rain fields spanning the entire UK with a range of voxel diameters from 1 to 5 km and with a sampling time to 15 minutes. The application of the downscaling methods to these data are likely to require further developments but would yield a simulator that could be applied to national networks. At a minimum, a more sophisticated method to describe advections between rain fields would be required as the linear translation is unlikely to be adequate for fronts of this size.

A weakness of the current simulator is its reliance upon rain rate as the fundamental parameter. Rain rate was chosen as it can be converted to specific attenuation at any frequency using Rec. ITU-R P.838-2. Also, many studies had been performed, and models existed describing, rain rate variation in time and space. The Rec. 838 transformation from rain rate to specific attenuation is deterministic where the actual transformation is stochastic due to the variability in the drop size distribution. This is one of the major uncertainties in the simulation model. The CRIE database contains dual polarization radar data and these have been converted to rain rate using a two-parameter (M-P) drop size distribution. An alternative approach would have been to model the spatial-temporal variation of the DSD parameters rather than rain rate. This would have been entirely novel and would lack the foundations of known rain rate variation statistics. However, it would be an interesting future study.

As the current simulator is based on CRIE data, the results are only applicable to link networks in the southern UK, or places with a similar climate. Starting with different data bases of radar data would yield simulators applicable to the climates where the data was acquired. However, numerical methods could probably be developed to adjust the simulator to other climates. The HYCELL pulse model scales the intensity and mean arrival rate of rain cells of different classifications to match a range of climates. It is likely that similar methods could be applied to the current simulator. Similar methods could be used to introduce year-to-year variation into the current simulator. Although considerably more speculative, the simulator could be used to predict and quantify the effects of climate change on the telecommunications network.

11.2.2 Automatic Transmit Power Control

Most wireless local loop and fixed wireless access systems in the market already employ adaptive power control techniques. With power control Fade Mitigation Techniques, the transmitter power is adjusted in order to increase the radiated power during fading conditions. Given a reliable power control system, it could be possible to reduce the fixed margin during clear sky conditions, thereby improving the rate of frequency reuse. Adaptive power control has the ability to compensate for fades whilst reducing the potential for interference outside the network. The level of transmit power is adjusted dynamically, based on information such as the distribution of fades experienced by users within the network. Information on the distribution of fades can be obtained by employing monitoring stations at the periphery of the network, or by user terminals sending information back on their received power levels.

Two recent Spectrum Efficiency Scheme projects (SES 2004-7 and SES 2006-1, reports on Ofcom web site) have examined the potential of ATPC on fixed links to reduce frequency reuse distances and assess the problems posed by introducing ATPC links into existing non-ATPC bands. Both projects concluded that ATPC was beneficial and the increase in outage due to interference was minimal. The advantage depends upon the incidence of wanted paths experiencing rain fade while unwanted paths do not, and so depends upon the spatial and temporal incidence of rain. The rain model used for these projects was extremely simplistic i.e. snap-shot FBfs not constrained to any real measurements and without advection i.e. time-series were not generated. The model assumed it rains everywhere. The repeat of this analysis by using developed simulator can be done. The expect is that, using this method illustrate by this work, link orientation will be shown to lead to different outage durations where it was not possible to assess this in the previous studies. Differences between the two results will yield information on the sophistication of rain models necessary for spectrum regulation.

11.2.3 Dynamic Modulation

The RF links are run using fixed margins with the size of the margin dependent upon the maximum rain attenuation predicted for the service area. One way to increase the system data throughput is to manage each user terminal separately and have each one use as high a level modulation in combination with as a code rate as the instantaneous link conditions allow. As link conditions fade for each individual terminal, the modulation level and code rate is changed to maintain BER (Bit Error Rate) requirements. Dynamic modulation switching responds to fading by switching between various M-PSK modulation schemes, each at a different data throughput rate.

Fixed links typically operate with a pre-set modulation scheme e.g. 16-QAM or 64-QAM. Higher order modulation schemes yield higher capacities but require higher signal to noise plus interference ratio. As a channel degrades, due to attenuation of the wanted signal or increases in interference, high order modulation schemes rapidly loose capacity as the BER increases, where lower order modulation would yield higher capacity. A dynamic system would use high order modulation when the channel was clear and automatically reduce the modulation order as the channel degraded e.g. in rain, to optimise capacity. There is engineering overhead in building this capability into links so it is important that the benefits are quantified. This can only be achieved by second-by-second simulation of a variety of small networks i.e. combinations of path geometries, frequencies etc. Trails in India have suggested significant improvements for PMP systems, Hughs (2003).

11.2.4 Fade Durations

In Chapter 10 the RAL/ITU rain fade duration model was introduced and compared simulation results for a range of links. The rain fade duration statistics could be calculated for a range of link frequencies and lengths, possibly with a one second integration time. Fitting parameterised distributions to these results, e.g. a Weibull distribution, would yield a general fade duration model for terrestrial links. A similar process could be used to generate a fade slope model for terrestrial links.

APPENDIX A

ONE DIMENSIONAL INTERPOLATION SCHEME

A stochastic, numerical method to interpolate point rain rate time-series to shorter sampling periods, while conserving the expected first and second order statistics is described in this section.

Consider the sequence {X_{-2}, X_{-1}, X_1, X_2} which is interpolated to {X_{-2}, Z_{-3}, Y_{-1}, Z_{-2}, X_{-1}, Z_{-1}, Y_1, Z_1, X_1, Z_2, Y_2, Z_3, X_2}. Then,

$$Y_1 = AX_{-2} + BX_{-1} + BX_1 + AX_2 + \xi_0$$

$$Z_1 = AX_{-1} + BY_1 + BX_1 + AY_2 + \xi_1$$

where $\xi_i \in N\left(0, \sigma_i^2\right)$, the additive random variable being sampled from a Gaussian distribution. Thus:

$$E[Y] = (2A + 2B)E[X]$$

$$E[Z] = (A + B)E[X] + (A + B)E[Y]$$

In order to conserve mean, i.e. $E(Z) = E(Y) = E(X)$, then:

$$A + B = \frac{1}{2} \tag{A1}$$

$$E[Y_1^2] = E[(AX_{-2} + BX_{-1} + BX_1 + AX_2)^2 + 2\xi_0(AX_{-2} + BX_{-1} + BX_1 + AX_2) + \xi_0^{\ 2}]$$

$$E[(AX_{-2} + BX_{-1} + BX_1 + AX_2)^2] =$$

$$[2A^2 + 2B^2 + 2A^2\rho(3) + 2B^2\rho(1) + 4AB\rho(1) + 4AB\rho(2)]E[X^2]$$

where $E[X^2]\rho(\tau) = E\left(X_i X_{i+\tau}\right)$

$$E[2\xi_0(AX_{-2} + BX_{-1} + BX_1 + AX_2)] = 0$$

$$E[\xi_0^{\ 2}] = \sigma_0^{\ 2}$$

Thus:

$$E[Y_1^{\ 2}] = [2A^2 + 2B^2 + 2A^2\rho(3) + 2B^2\rho(1) + 4AB\rho(1) + 4AB\rho(2)]E[X_1^{\ 2}] + \sigma_0^{\ 2}$$

For interpolation we choose $E(Y^2) = E(X^2)$ to conserve variance and so:

$$\sigma_0^{\ 2} = [1 - (2A^2 + 2B^2 + 2A^2\rho(3) + 2B^2\rho(1) + 4AB\rho(1) + 4AB\rho(2))]E[X^2] \qquad \text{(A2)}$$

$$E[Z_1^{\ 2}] = E[(AX_{-1} + BY_1 + BX_1 + AY_2)^2 + 2\xi_1(AX_{-1} + BY_1 + BX_1 + AY_2) + \xi_1^{\ 2}]$$

$$E[Z_1^{\ 2}] = (A^2 + B^2)E[X^2] + (A^2 + B^2)E[Y^2] + 2AB\rho(1)E[X^2] + 2ABE[X_{-1}Y_1] +$$

$$2A^2E[X_{-1}Y_2] + 2B^2E[Y_1X_1] + 2ABE[Y_1Y_2] + 2AB[X_1Y_2] + \sigma_1^{\ 2}$$

$$E[X_1Y_1] = E[X_1(AX_{-2} + BX_{-1} + BX_1 + AX_2 + \xi_0)] = [A\rho(2) + B\rho(1) + B + A\rho(1)]E[X^2]$$

$$E[X_{-1}Y_1] = E[X_{-1}(AX_{-2} + BX_{-1} + BX_1 + AX_2 + \xi_0)] = [A\rho(1) + B\rho(1) + B + A\rho(2)]E[X^2]$$

$$E[X_1Y_2] = E[X_1(AX_{-1} + BX_1 + BX_2 + AX_3 + \xi_0)] = [A\rho(1) + B\rho(1) + B + A\rho(2)]E[X^2]$$

$$E[Y_1Y_2] = E[(AX_{-2} + BX_{-1} + BX_1 + AX_2 + \xi_0)(AX_{-1} + BX_1 + BX_2 + AX_3 + \xi_0)]$$

$$= [(2A^2 + 2AB + 2B^2)\rho(1) + (A^2 + 2AB + B^2)\rho(2) + 2AB\rho(3) + A^2\rho(4) + (2AB + B^2)]E[X^2]$$

$$E[X_{-1}Y_2] = E[X_{-1}(AX_{-1} + BX_1 + BX_2 + AX_3 + \xi_0)] = [B\rho(1) + B\rho(2) + A + A\rho(3)]E[X^2]$$

$$E[Z_1^{\ 2}] = (A^2 + B^2 + 4AB^2 + 2A^3 + 2B^3 + 4A^2B^2 + 2AB^3)E[X^2] +$$

$$(A^2 + B^2)E[Y^2] +$$

$$(2B^3 + 6A^2B + 6AB^2 + 2AB + 4A^3B + 4A^2B^2 + 4AB^3)\rho(1)E[X^2] +$$

$$(2A^3B + 2AB^3 + 2AB^2 + 6A^2B + 4A^2B^2)\rho(2)E[X^2] +$$

$$(2A^3 + 4A^2B^2)\rho(3)E[X^2] +$$

$$2A^3B\rho(4)E[X^2] +$$

$$\sigma_1^{\ 2} \tag{A3}$$

If variance is to be conserved then $E(Z^2) = E(Y^2) = E(X^2)$

In order to obtain $\sigma_1^{\ 2} = \left(\frac{1}{2}\right)^{2H} \sigma_0^{\ 2}$, where $H = 1/3$, then

Thus: $\sigma_1^{\ 2} = \left(\frac{1}{2}\right)^{\frac{2}{3}} \sigma_0^{\ 2}$ (A4)

From (1), (2), (3), (4) then:

$$(2A^2 + 2B^2 + 4AB^2 + 2A^3 + 2B^3 + 4A^2B^2 + 2AB^3 - 1)E[X^2] +$$

$$(2B^3 + 6A^2B + 6AB^2 + 2AB + 4A^3B + 4A^2B^2 + 4AB^3)\rho(1)E[X^2] +$$

$$(2A^3B + 2AB^3 + 2AB^2 + 6A^2B + 4A^2B^2)\rho(2)E[X^2] +$$

$$(2A^3 + 4A^2B^2)\rho(3)E[X^2] +$$

$$2A^3B\rho(4)E[X^2] =$$

$$\left(\frac{1}{2}\right)^{\frac{2}{3}}(2A^2 + 2B^2 - 1)E[X^2] +$$

$$\left(\frac{1}{2}\right)^{\frac{2}{3}}(2B^2 + 4AB)\rho(1)E[X^2] +$$

$$\left(\frac{1}{2}\right)^{\frac{2}{3}}4AB\rho(2)E[X^2] +$$

$$\left(\frac{1}{2}\right)^{\frac{2}{3}}2A^2\rho(3)E[X^2]$$

$$\left(\frac{1}{2}\right)^{\frac{2}{3}} = 0.63$$

$\rho(1), p(2), p(3), \rho(4)$ can be obtained from $E[X^2]\rho(\tau) = E(X_i X_{i+\tau})$ by using radar data to calculate out $E[X^2], E(X_i X_{i+\tau})$.

$\rho(1) = 0.9923$

$\rho(2) = 0.9890$

$\rho(3) = 0.9861$

$\rho(4) = 0.9835$

Then:

$A = 0.079 \qquad B = 0.421 \qquad \sigma_0 = 0.4211$

APPENDIX B

TWO DIMENSIONAL INTERPOLATION SCHEMES

A stochastic, numerical method to interpolate point rain rate time-series to shorter sampling periods based on 2D interpolation (ray) and 3D interpolation (square area), while conserving the expected first and second order statistics is described in this section.

Consider a two-dimensional array of log rain rate samples $X = \{X_i = X(j\Delta x, k\Delta t)\}$ sampled at spatial intervals of Δx along the ray (initially $\Delta x = 300m$) and with a temporal sampling period of Δt, initially $\Delta t = 10$ minutes. The single index i mapping onto the multi-index (j,k) in 2D, is a notational convenience that makes algorithm development independent of the number of dimensions. The new interpolates for a set $Y = \{Y_i\}$ via the Voss process $Y = S(X) + \varepsilon$. Here S represents smooth interpolation and ε is the random noise process yielding Gaussian samples $\varepsilon \in N(0, \sigma_n^2)$.

```
X    X    X    X

X    X    X    X
        Y
X    X    X    X

X    X    X    X
```

Figure B.1 2D interpolation by using 16 points in the neighborhood of Y_i.

The following three conditions are required.

First, $E(Y) = E(X)$.

Second, $E(Y^2) = E(X^2)$.

Third, $S(\omega) =\propto \omega^{-\beta}$, $\beta = D^{-2/3}$, D stands for dimension.

If $S(X)=\sum_{i=1}^{n} a_i X_i$, where $a_i \neq 0$ only in neighborhood of Y.

Assume in the neighborhood, $X_i = \overline{X} + \xi$, $\xi \in N(0,\sigma_s^2)$.

$$E(Y)=E[\sum a_i(\overline{X}+\xi)+\varepsilon]=\overline{X}\sum a_i$$

To satisfy first condition $E(Y)=E(X)$,

$$\sum a_i = 1. \qquad \text{(B1)}$$

$$E(Y^2)=E[(\sum a_i(\overline{X}+\xi)+\varepsilon)^2]$$

$$=E[(\sum a_i(\overline{X}+\xi))^2+2\varepsilon\sum a_i(\overline{X}+\xi)+\varepsilon^2]$$

$$=E[\sum\sum a_i a_j(\overline{X}+\xi_i)(\overline{X}+\xi_j)+2\varepsilon\sum a_i(\overline{X}+\xi)+\varepsilon^2]$$

$$=E[\overline{X}^2\sum\sum a_i a_j+\sigma_s^2\sum a_i^2]+0+E[\varepsilon^2]$$

$$=\overline{X}^2\sum\sum a_i a_j+\sigma_s^2\sum a_i^2+\sigma_n^2$$

$$=\overline{X}^2+\sigma_s^2\sum a_i^2+\sigma_n^2$$

To satisfy second condition $E(Y^2)=E(X^2)$, which means $E[(\overline{X}+\xi_i)^2]=\overline{X}^2+\sigma_s^2$.

Thus, $\sigma_s^2\sum a_i^2+\sigma_n^2=\sigma_s^2$.

Then, $\sigma_n^2=\sigma_s^2(1-\sum a_i^2)$,

$$\sum a_i^2 = 1-\frac{\sigma_n^2}{\sigma_s^2}. \qquad \text{(B2)}$$

According Voss algorithm, $\sigma_n^2=\sigma_{n-1}^2 2^{-2H}$, where H is the Hurst coefficient, $H=1/3$. (B3)

During interpolation, a function is build as following before adding noise.

$F=\alpha * F1+(1-\alpha)F2$, $F1$ coefficients come from 2D or 3D sinc filter, $F2$ has constant coefficients.

In the case of 2D interpolation, 16 points are in use. During the first iteration,

$Y = \frac{1}{16}\sum_{i=0}^{16} X_i^0 + N(0,\sigma_0)$, where X_i^0 is the value of the average of 16 points. Thus,

$\sigma_Y^2 = \frac{1}{256}\sum_{i=1}^{16}\sigma_X^2 + \sigma_0^2$. In order to conserve variance, i.e. $\sigma_Y^2 = \sigma_X^2$, require $\sigma_0^2 = \frac{15}{16}\sigma_X^2$.

BX	CX	CX	BX
CX	AX	AX	CX
	Y		
CX	AX	AX	CX
BX	CX	CX	BX

Figure B.2 2D interpolation by using 16 points in the neighborhood of Y_i (with coefficients A, B and C)

A, B and C are coefficients a_i of F1 function illustrated in figure 2.2.

F1=[B C C B; C A A C; C A A C; B C C B], where A=9/16, B=1/16, C=-3/16.

F2=16/1[1 1 1 1; 1 1 1 1; 1 1 1 1; 1 1 1 1].

The filter coefficients for 2D interpolation are listed in Table B.1.

Filter Coefficients	**AX**	**BX**	**CX**
F1	9/16	1/16	-3/16
F2	1/16	1/16	1/16

Table B.1 Filter coefficients for 2D interpolation.

It is necessary to find the linear weighting factor *a* that satisfies the variance constraint. The target filter coefficient sum-of-squares can be estimated from the data and a then calculated using:

$$\alpha = \sqrt{\frac{16\sum a_i^2 - 1}{24}}$$

REFERENCES

Atlas D. and Williams. C. R, The anatomy of a continental tropical convective storm, *J. of Atmos. Sci.*, 60(1), p3-15, 2003.

Atlas D. and Ulbrich C. W.. The physical basis for attenuation-rainfall relationships and the measurement of rainfall parameters by combined attenuation and radar method, In: *J. Rech. Atmos.*, vol. 8, pp. 275-298, Jan.-Jun., 1974.

Barclay L.. *Propagation of Radiowaves*, 2nd Edition, MPG Books Ltd, UK, 2003.

Bec J., Celani A., Cencini M. and Musacchio S., Clustering and collisions of heavy particles in random smooth flows, *Phys. Fluids*, 17(7), art. no. 073301, 2005.

Bell T. L.. A space-time stochastic model of rainfall for satellite remote sensing studies, *J. Geophys. Res.*, 92, pp9631-9643, 1987.

Bolea-Alamanac A. and Bousquet M.. Millimeter-wave radio systems: guidelines on propagation modeling and impairment mitigation techniques research needs. In: *First COST 280 workshop*, Malvern, UK, July, 2002.

Bringi V. N. and Chandrasekar V.. *Polarimetric Doppler Weather Radar: Principles and Applications.* Cambridge University Press, pp.636, 2001.

Brussaard G.. A meteorological model for rain-induced cross-polarization, In: *IEEE Trans. Antennas Propag.*, 24, (1), pp. 5-11, 1976

Callaghan S. A. *et al*, *Impact of Introducing Automatic Transmit Power Control in P-P Fixed Service Systems operating in bands above 13GHz*, CCLRC Rutherford Appleton Laboratory Report, December 2005.

Callaghan S. A. *et al*, Improving Spectrum Efficiency of Fixed Links Services, *CCLRC Rutherford Appleton Laboratory Report*, September 2006.

Callaghan S. A., *Fractal analysis and synthesis of rain field for radio communication systems.* Ph.D. dissertation, University of Portsmouth, UK, March, 2004.

Callaghan S. A., Model to generate synthetic rain intensity fields for any given area, *ITU-R Document 3J/181-E*, *Document 3M/205-E*, 10th April 2007a.

Callaghan S. A., Vilar, E., Fractal Generation of Rain Fields: Synthetic realisation for radio communication systems, *IET Microwaves, Antennas and Propagation*, 1 (6), 1204-1211, December 2007b.

Capsoni C., Fedi F. and Paraboni A., "A comprehensive attenuation time series generator and comparison with Olympus data meteorologically oriented methodology for the prediction of wave propagation parameters in telecommunication applications beyond 10 GHz", *Radio Science*, vol. 22, no. 3, pp. 387-393, 1987.

Castanet L., Lemorton J., Konefal T., Shukla A., Watson P., Wrench C.. Comparison of combined propagation models for predicting loss in low-availability systems that operate in the 20 GHz to 50 GHz frequency range, In: *Int.J. Satell. Commun.*, Vol. 19, n3, pp. 317-334, May-June 2001.

Castanet L., Bousquet M., Filip M., Gallois P., Gremont B., Haro L. De, Lemorton J., Paraboni A., Schnell M.. Impairment mitigation and performance restoration, In: *COST 255 Final Report*, Chap 5.3, ESA Publ. Div., SP-1252, March 2002.

Celani A., Falkovich G., Mazzino A., Seminara A., Droplet condensation in turbulent flows, *Europhys. Lett.*, 70 (6): 775-781, 2005.

Chilbolton radar website. In: www.chilbolton.rl.ac.uk, Accessed: Sep-Dec.2005.

Cho H. K., Bowman K. P., North G. R., A comparison of gamma and lognormal distributions for characterizing satellite rain rates from the tropical rainfall measuring mission , *J. of Appl. Meteorology*, 43 (11): 1586-1597 Nov. 2004.

COST 235 Management Committee, *COST 235 Radiowave propagation effects on next-generation fixed-services terrestrial telecommunications systems*, ISBN 9282780236, European Commission, 1996.

COST 235 Management Committee, *COST210. Influence of the atmosphere on interference between radio communications systems at frequencies above 1GHz.*, ISBN 9282780236, EUR 13407 EN, 1991.

COST 280. *Propagation Impairment Mitigation for Millimetre Wave Radio Systems*. [www.cost280.rl.ac.uk/], 2005.

Cowpertwait P. S. P., Kilsby C. G. and O'Connell P. E.. A space-time Neyman-Scott model of rainfall: Empirical analysis of extremes. *Water Resources Research*, VOL. 38, NO. 8, 1131, doi:10.1029/2001WR000709, 2002.

Crane R. K. and Shieh Horng-Chung, "A two component rain model for the prediction of site diversity performance," *Radio Science*, vol. 24, no. 6, pp. 641-665, Sept.-Oct. 1989.

Crane R. K., *Electromagnetic wave propagation through rain*, John Wiley&Sons, Inc., 1996.

Crane R. K.. Space-time structure of rain rate fields. *Journal of Geophysical Research*, vol. 95, pp.2011-20, 1990.

Davis A., Marshak A., Wiscombe W. and Cahalan R.. Multifractal characterization of nonstationarity and intermittency in geophysical fields: observed, retrieved, or simulated, *J. Geophys. Res.*, 99, PP8055-8072, 1994.

Deidda R., Multifractal analysis and simulation of rainfall fields in space. *Physics and Chemistry of the Earth Part B – Hydrology, Oceans and Atmosphere*, 24(1-2), pp73-78, 1999.

Deidda R., Benzi R. and Siccardi F., Multifractal Modeling of Anomalous Scaling Laws in rainfall. *Water Resour. Res.*,, 35(6), pp1853-1867, 1999.

Deidda R., Rainfall downscaling in a space-time multifractal framework. In: *Water Resources Research*. Vol. 36, No. 7, pp 1779-1794, Jul. 2000.

Eagleson P. S., Fenessey N. M., Quiliang W. E., and Grodriguez-Iturbe I., Application of Spatial Poisson Models to Airmass Thunderstorm Rainfall, *J Geophys. Res*., 92, pp9961-9978, 1987.

Easterbrook B. J. and Turner D., Prediction of attenuation by rainfall in the 10.7 to 11.7 GHz communication band. *Pro. Inst. Elec. Eng.*, vol 114, pp557-565, May 1967.

Fabry. F. On the determination of scale ranges for precipitation fields. In: *J. Geophys. Res.*, 101(D8), Vol. 12, pp.819-826, 1996.

Falconer K.. *Fractal Geometry: Mathematical Foundations and Applications.* John Wiley & Sons. UK. 1990

Falkovich G., Weinberg A., Denissenko P., Lukaschuk S., Floater clustering in a standing wave, *Nature*, 435 (7045): 1045-1046, 2005.

Fenton G. A. and Vanmarcke E., Simulation of Random Fields via Local Average Subdivision, *ASCE Journal of Engineering Mechanics*, 116(8), 1733-1749, 1990.

Feral L. and Sauvageot H., Fractal identification of supercell storms, *Geophysical Res. Lett.*, 29(14), 2002.

Feral L., Mesnard F., Sauvageot H., Castanet L., Lemorton J.. Rain cells shape and orientation distribution in South-West of France, In: *Phys. Chem. Earth (B)*, Vol. 25 n 10-12, pp. 1073-1078, 2000.

Feral L., Lemorton J., Castanet L. and Sauvageot H.. *HYCELL: a new model of rain fields and rain cells structure*, Electro-Magnetism and Radar Department, University of Paul Sabatier, France, 2003.

Ferraris L., Rudari R., and Siccardi F., The uncertainty in the prediction of flash floods in the northern Mediterranean environment, *J. Hydrometeorol*., 3, pp714-727, 2002.

Ferraris L., Gabellani S. and Rebora N.. A comparison of stochastic models for spatial rainfall downscaling. *Water Resources Research*. Vol. 39, No. 12, pp1368. Dec. 2003.

Foufoula-Georgiou E. and Krajewski W., Recent advances in rainfall modeling, estimation, and forecasting, In: *Rev. Geophys.*, Vol. 33, pp. 1125-1137, 1995.

Gerald Edgar, *Classics on Fractals*, Addison-Wesley 1993.

Goddard J. W. F. and Thurai M., Radar-derived path reduction factors for terrestrial systems, in *"Tenth International Conference on Antennas and Propagation",* vol. 436, pp. xxxiii+553+396. Edinburgh, UK: IEE, 1997.

Goddard J. W. F. and Thurai M.. Modeling of attenuation due to rain on terrestrial paths using Chilbolton radar data. In: *NRPP Research Note.* No.159. 1996.

Goddard J. W. F. and Cherry S. M., The ability of dual-polarisation radar (copolar linear) to predict rainfall rate and microwave attenuation, *Radio Science*, volume 19(1), pp. 201–208, 1984.

Guillot G. and Lebel T., Disaggregation of Sahelian mesoscale convective system rain fields: Further developments and validation, *J. Geophys. Res*., 104, pp31533-31551, 1999.

Gupta V. K. and Waymire E. C.. A Statistical Analysis of Mesoscale Rainfall as a Random Cascade. *Journal of Applied Meteorology*. Vol. 32 pp251-267. 1993.

Harden B. N., Norbury J. R. and White W. J. K., Model of intense convective rain cells on estimating attenuation on terrestrial millimetric radio links, *Electron. Lett*., 10(23), 1974.

Harden B. N., Norbury J. R. and White W. J. K.. Use of a lognormal distribution of raindrop sizes in millimetric radio attenuation studies. In: *IEE Conf*. Publ. 169, Part 2, pp. 87-91, 1978.

Harris D., Menabde M., Seed A. W. and Austin G. L.. Multifractal characterization of rain field with a strong orographic influence. *Jnl. Geophys. Res.* Vol. 101, D21, 1996.

Hendry A., Antar Y. M. M. and McCormick G. C.. On the relationship between the degree of preferred orientation in precipitation and dual polarization radar echo characteristics. In: *Radio Science*, 22. pp.37-50, 1987.

Hentschel H. G. E. and Procaccia I., The infinite number of generalized dimensions of fractals and strange attractors. *Physic D*, vol. 8, pp. 435-444, 1983.

Holt. A. R, Uzunoglu N.K. and Evans B. G.. An integral equation solution to scatteing of electromagnetic radiation by dielectric spheroids and ellipsoids. In: *IEEE Trans. Antenna and Propagation.* 26, pp706-712, 1978.

Hulst H. C. Van De. *Light scattering by small particles*, Dover Publications, Inc., New York, USA, 1981.

Hurst H. E., Black R. P., and Simaika Y. M.. *Long-Term Storage: An Experimental Study*. Constable, London, 1965.

Illingworth A. J. and Caylor I, J.. Polarization radar estimates of raindrop size spectra and rainfall rate. *Journal of Atmospheric and Oceanic Technology*. Vol.6, pp. 939-49, 1989.

Illingworth. A. J.. Improved precipitation rates and data quality by using polarimetric measurements. *Advanced Applications of Weather Radar*. Springer, in press edn., 2003. In: http://www.ucl.ac.uk/Stats/research/Resrprts/rr176/176.html. Accessed: Mar-May, 2006.

ITU-R. Characteristics of precipitation for propagation modeling, In: *Recommendations ITU-R P. 837-5*, Supplement 1 to Vol. 2000, P series, part 1 and 2, 2007.

ITU-R. Conversion of Annual Statistics to Worst-Month Statistics. In:

Recommendation ITU-R P.841-1, 1999.

ITU-R. Propagation data and prediction methods required for the design of terrestrial line-of-sight systems. In: *Recommendations ITU-R P.530-12*, 2007.

ITU-R. Propagation data and prediction methods required for the design of Earth-space telecommunication systems, In: *Recommendations ITU-R P.618-7*, 2001.

ITU-R. Propagation data and prediction methods required for the design of terrestrial broadband millimeter radio access systems operating in a frequency range of about 20-50 GHz in vegetation. In: *Recommendation ITU-R P.1410-2*, 2003.

ITU-R. Specific attenuation model for rain for use in prediction methods, In: *Recommendations ITU-R P.838-2*, 2003.

ITU-T Recommendation G.826*, Error performance parameters and objectives for international, constant bit rate digital paths at or above the primary rate*. 1999.

ITU-T Rec. G.828, *Error performance parameters and objectives for international, constant bit rate synchronous digital paths.* 2000.

Jensen J. R., *Remote Sensing of the Environment: An Earth Resource Perspectice, Upper Saddle River*, New Jersey: Prentice Hall, 2000.

Joss J., Thomas J. C. and Waldvogel A.. The variation of raindrop size distribution at Locarno, In: *Proc. of international conference on cloud physics*, pp. 369-373, 1967.

Kedem B., Pavlopoulos H., Guan X. D., Short D. A., A probability-distribution model for rain rate *, J. of Appl. Meteor*. 33 (12): 1486-1493 Dec. 1994.

Kedem B., Chiu L. S., Are Rain Rate-Processes Self-Similar, *Water Resourc. Res.*, 23 (10): 1816-1818, Oct. 1987.

Kolmogorov A. N., The local structure of turbulence in incompressible viscous fluid for very large Reynolds number. *Dokl. Akad. Nauk SSSR* 30 9–13, 1941.

Kolmogorov A. N.. A refinement of previous hypotheses concerning the local structure of turbulence in a viscous incompressible fluid at high Reynolds number. *J. Fluid Mech.*, 13, 82–85. 1962

Kolmogorov A. N., The local structure of turbulence in incompressible viscous fluid for very large Reynolds numbers, *Proc. R. Soc*. Lond. A, 434, 9-13, 1991.

Kraichnan R. H. and Montgomery D., "Two dimensional turbulence," *Rep. Prog. Phys*., Vol. 43, pp. 547-619, 1980.

Landsberg H. E., *The Urban Climate, International Geophysics Series*, Vol. 28, New York: Academic Press. 1981.

Laws J. O. and Parsons D. A.. The relation of rain-drop size to intensity, In: *Trans. Amer. Geophys*. Union, 24, pp. 432-460, 1943.

Lawson C. L. and Hanson R. J., *Solving Least Squares Problems*, Prentice-Hall, Chapter 23, p. 161. 1974.

Leijnse H., Uijlenhoet R. and Stricker J. N. M., Rainfall measurement using radio links from cellular communication networks, *Water Resource Research*, VOL. 43, W03201, doi:10.1029/2006WR005631, 2007.

Leitao M. J. and Watson P. A., Application of dual linearly polarized radar data to prediction of microwave path attenuation at 10-30 GHz. *Radio Sci.*, vol.19, pp. 209-221, 1984.

Lin S. H., Statistical behavior of rain attenuation. *Bell Syst. Tech. J.*, vol. 52, pp557-581, Apr. 1973.

Lin. S. H., Statistical Behavior of Rain Attenuation, In: *Bell Syst. Tech. J.*, vol 52, pp. 557-581, April 1973.

Lovejoy S. and Mandelbrot B., Fractal properties of rain and a fractal model, *Tellus, Ser. A*, 37, pp209-232, 1985.

Lovejoy S. and Schertzer D., Turbulent compound Poisson / multifractal processes for modeling precipitation and the nature of the zeroes, *Geophysical Research*, Vol. 9, 10275, 2007.

Lovejoy S., Area-Perimeter Relation for Rain and Cloud Areas, *Science*, 216, 185-187, 1982.

Lovejoy S., Schertzer D.. Generalised scale-invariance in the atmosphere and fractal models of rain, *Water Resources Research*, Vol. 21 Part 8, pp1233-1250, 1985.

Lovejoy S., Schertzer D.. Multifractals and rain. In: *New Uncertainty Concepts in Hydrology and Water Resources*, edited by Z. W. Kunzewicz, Unesco Ser. In Water Sci., Cambridge Univ. Press, New York, 1992.

Mandelbrot B. B. and Wallis J. W., Fractional Brownian motions, fractional noises, and applications. SIAM review. Vol. 10. pp422-437, 1968.

Mandelbrot B. B.. *Fractals: Form, Chance, and Dimension*. W. H. Freeman and Co., San Francisco, 1977.

Mandelbrot B. B.. *The Fractal Geometry of Nature*. Freeman, New York, 1982.

Marsan D, Schertzer D., Lovejoy S., Causal space-time multifractal processes: predictability and forecasting of rain fields. *Jnl. Geophys. Res.* Vol. 101, D21, Nov. 1996.

Marshall J. S. and Hitschfield W., Interpretation of the fluctuating echo from randomly distributed scatters, In: *Canadian Journal of Physics*, vol. 31, pp.962-943, 1953.

Marshall J. S. and Palmer W. McK., The distribution of raindrops with size, In: *J. Meteor.*, vol. 5, pp.165-166, 1948.

Maseng T., Bakken P. M.. A stochastic dynamic model of rain attenuation. IEEE *Transactions on Communications.* Vol. COM-29, No.5, May.1981.

Matricciani E. and Pawlina A.. Rain cell size statistics inferred from long term point rain rate: model and results. *Proc. Third Ka Band Utilization Conf.*, pp.299-304. Sep. Sorrento, Italy. 1997.

Matricciani E. and Pawlina A.. Statistical characterization of rainfall structure and occurrence for convective and stratiform rain inferred from long term point rain ratedata. In: *AP 2000 Millennium Conference on Antennas & Propagation*, URSI, Davos, Switzerland, 2000.

Matricciani E.. Physical-mathematical model of the dynamics of rain attenuation based on rain rate time series and a two-layer vertical structure of precipitation. *Radio Science*. Vol. 31, No. 2, pp.281-295, March-April, 1996.

Mejia J. and Rodriguez-Iturbe I., On the synthesis of random fields sampling from the spectrum: An application to the generation of hydrologic spatial processes, *Water Resour. Res.*, 10, pp705-711, 1974.

Menabde M., Seed A., Harris D. and Austin G., Multiaffine random field model of rainfall, *Water Resour. Res.*, pp35509-35514, 1999.

Menabde M., Seed A., Harris D. and Austin G., Self-similar random fields and rainfall simulations, *J. Geophys. Res.*, 102, pp13509-13515, 1997a.

Menabde M., Seed A., Harris D., Austin G. and Stow D., Multiscaling properties of rainfall and bounded random cascades, *Water Resour. Res.*, 33, pp2823-2830, 1997b.

Monin A. S. and Yaglom A. M., *Statistical Fluid Mechanics*, vol.1, MIT press, Cambridge, Mass., 1971.

Monin A. S. and Yaglom A. M., *Statistical Fluid Mechanics*, vol.2, MIT press, Cambridge, Mass., 1975.

Myers W., Comparison of Propagation Models, In: *IEEE transaction* P802.16cc-99/13, 31 Aug. 1999.

Northrop P. A., A clustered spatial-temporal model of rainfall. *Proc. R. Soc. London, Ser. A.* 454, pp1875-1888, 1998.

Oguchi T., Attenuation of electromagnetic wave due to rain with distorted raindrops, In: *Journal of the Radio Research Laboratories*, vol. 7, no. 33, pp. 467-485, Sep. 1960.

Oguchi T.. Attenuation of electromagnetic wave due to rain with distorted raindrops (Part 2), In: *Journal of the Radio Research Laboratories*, vol. 11, no. 53, pp. 19-44, Jan. 1964.

Oguchi T.. Scattering from hydrometeors: A survey. In: *Radio Science*, vol. 16, n 5, pp. 691-730, Sep.-Oct., 1981.

Oguchi T.. Scattering properties of Pruppacher-and-Pitter form raindrops and cross polarization due to rain: Calculations at 11, 13, 19.3 and 34.8GHz. In: *Radio Science*, vol. 12, n.1, pp. 41-51, Jan.-Feb., 1977.

Olsen R. L., Rogers D. V. and Hodge D. B., The aR^b relation in the calculation of rain attenuation. In: *IEEE Transactions on Antennas and Propagation*. Vol. 26, n. 2, pp. 318-329, Mar. 1978.

Olsson J., and Niemczynowicz J., Fractal analysis of high resolution rainfall time series. *Journal of Geophysical Research-Atmospheres*, Vol. 98, D12, 1993.

Olsson J., and Niemczynowicz J., Multifractal analysis of daily spatial rainfall distributions, *Journal of Hydrology*, 187, 29-43, 1996.

Onof, C., Changing rectangular pulses to series of rain pulses and thus adapting the Poisson-cluster models to finer time-scales, *RAINMAP*, 2007.

Ossiander M. and Waymire E., Statistical Estimation For Multiplicative Cascades, *The Annals of Statistics*, Vol. 28, No. 6, pp.1533–1560, 2000.

Over T. M. and Gupta V. K., A space-time theory of mesoscale rainfall using random cascades, *J. Geophys. Res.*, 101, pp26319-26331, 1996.

Paraboni A., Capsoni C. and Riva C.. Spatial rain distribution models for the prediction of attenuation in point-to-multipoint and resource-sharing systems in the Ka and V frequency bands. In: *Proceedings of URSI Commission F Meeting, Open Symposium on Propagation and Remote Sensing*, Germany, 2002.

Parsons A. J. and Stone P. M., Effects of inter-storm variations in rainfall intensity on the interrill runoff and erosion, *CATENA*, 67 (1): 68-78, Aug 15, 2006.

Patra K. C.. *Hydrology and Water Resources Engineering*, Alpha Science International Ltd., India, 2001.

Paulson K. S. and Baxter, Downscaling of rain gauge time series by multiplicative beta cascade, *J. Geophys. Res.*, 112, D09105, doi:10.1029/2006JD007333, 2007.

Paulson K. S. and Gibbins C. J., Rain models for the prediction of fade durations at millimetre wavelengths, *Microwaves, Antennas and Propagation, IEE Proceedings* -Volume 147, Issue 6, 431 – 436, Dec 2000.

Paulson K. S. and Zhang X., Estimating the scaling of rain rate moments from radar and rain gauge, *Geophys. Res. – Atmos*, 112, doi:10.1029/2007JD008547, 2007.

Paulson K. S., Fractal Interpolation of Rain Rate Time-Series, J. Geophys Res-Atmos 109 (D22): art. No. D22102. 2004.

Paulson K. S., Watson R. J. and Usman I. S., Diversity Improvement Estimation from Rain Radar Databases Using Maximum Likelihood Estimation. IEEE transactions on antennas and propagation, vol. 54, No.1, Jan. 2006.

Paulson K. S., The Effect of Variation in Atmospheric Absorption on Millimetric, Terrestrial, Telecommunications Links, *Radio Science*, 40, RS6004, 2005.

Paulson K. S., The Prediction Of Diversity Statistics On Terrestrial Microwave Links, *Radio Science,* Vol. 38, No. 3, art. No. 1047, June 2003a.

Paulson K. S., The second order statistics of the spatial-temporal rain rate random fields, Radio Science, 37, 5, 21-1 : 21-8. 2002.

Paulson K. S., *The simulation of rain effects on millimeter wave networks by the fractal disaggregation of radar data*. Didcot, UK. 2003b.

Paulson K.S., The Spatial-Temporal Statistics Of Rain Rate Random Fields, *Radio Science*, Vol. 37, No. 5, art. No. 1088, Sept. 2002.

Pavlopoulos H. and Gupta V. K., Scale invariance of regional wet and dry durations of rain fields: A diagnostic study, *J. of Geophys. Res.-Atmospheres* 108 (D8): Art. No. 8387 APR 15 2003.

Pavlopoulos H.. Scale invariance of regional wet and dry duration of rain fields: A diagnostic study. *Journal of Geophysical Research.* Vol. 108. No. D8. pp8387. 2003.

Pawlina A.. No Rain Intervals with Rain Events: Some Statistics Based on Milano Radar and Rain-gauge Data. *COST 280 1st International Workshop.* July, 2002.

Pawlina Bonati A., Rain areas on horizontal radar rain maps: new insight into spatial intensity distribution. *CLIMPARA 94-URSI Symp. on Climatic Parameters in Radiowave Propagation Prediction*. Moscow, pp.5.10.1-5. June. 1994.

Pech P., Bousquet M., Castanet L. and Radzik J.. Insight into architecture of Ka-band OBP satellite system involving FMTs, In: *AIAA Conference*, Montreal, Canada, April 2002.

Perica S. and Foufoula-Georgiou E., Model for multiscale disaggregation of spatial rainfall based on coupling meteorological and scaling descriptions, *J Geophys. Res.,* 101, pp26347-26361, 1996.

Peters O., Hertlein C. and Christensen K., A complexity view of rainfall, *Physical Rev. Lett*., 88(1), 018701-1, 2002.

Pruppacher H. R. and Beard K. V.. A wind tunnel investigation of the internal circulation and shape of water drops falling at terminal velocity in air. In: *Quart. J. Roy. Meteor. Soc.,* 96, pp. 247-256, 1970.

Puigcerver M., Alonso S., Lorente J., Llasat M. C., Redano A., Burgueno A. and Vilar E., Preliminary aspects of rainfall rates in the north east of Spain, *Theoretical and Applied Climatology*, Issue Volume 37, Numbers 1-2 PP.97-109,March, 1986.

Purdy J. C., Harrs D., Austin G. L., Seed A. W., Gray W.. A case study of orographic processes incorporating multiscaling characterization techniques, *Jnl. Geophys. Res.* Vol. 106, D8, 2001.

Ramachandran V., Nand N. R. and Northcott R. L., Effect of thunderclouds on space wave propagation at 10 GHz. In: *S. Pac. J. Nat. Sci.*, Issue 19, pp. 49-50, 2001.

Rhys F. S. and Waldvogel A., Fractal Shape of Hail Clouds, *Physical Rev. Lett.,* 56(7), 784-787, 1986.

Rodriguez-Iturbe I., Cox D. R., and Eagleson P. S., Spatial Modelling of Total Storm Rainfall. *Proc R. Soc. London, Ser. A*, 403, pp27-50, 1986.

Schertzer D., Lovejoy S., From scalar cascades to Lie cascades: joint multifractal analysis of rain and cloud processes, in *'Space/Time Variability and Interdependence for Various Hydrological Processes'*, ed. R.A. Feddes, Cambridge University Press, 153-173, 1995.

Schertzer D., Lovejoy S., Physical modelling and analysis of rain and clouds by anisotropic scaling multiplicative processes, *J. Geophys. Res*., 92, pp9693-9714, 1987.

Seed A. W., Srikanthan R. and Menabde M.. A space and time model for design storm rainfall. In: *Journal of Geophysical research*. Vol. 104 No.D24, pp. 31,623-31,630. 27. Dec. 1999.

She Z.-S and Waymire E. C., Quantised energy cascade and log-Poisson statistics in fully developed turbulence, *Phys. Rev. Lett.*, 72, 336-339, 1994 and 1996.

Sinclair P. C., Severe storm turbulent velocity and temperature structure, *6th Conference on Aerospace and Aeronautical Meteorology*, AMS, Boston, 1974.

Smith E. K.. Centimeter and Millimeter Wave Attenuation and Brightness Temperature due to Atmospheric Oxygen and Water Vapor, In: *Radio Science*, Vol 17, pp. 1455-1464, Nov.-Dec. 1982.

Svensson C., Olsson J., and Berndtsson R.. Multifractal properties of daily rainfall in two different climates. *Water Resour. Res*., Vol. 32, pp2463-2472, 1996.

Tan J. and Pedersen L., Study of Simultaneous Coverage and Route Diversity Improvement Under Rainy Periods for LMDS Systems at 42 GHz, *Millenium Conference on Antennas and Propagation*, AP2000, European Space Agency, Davos, Switzerland, April 9-14, 2000.

Taylor G. I., Statistical theory of turbulence, *Proc. Roy. Soc*. London A164, 476, 1938.

Tessier Y., S. Lovejoy, D. Schertzer. Universal multifractals – theory and observations for rain and clouds. *Jn1. Appl. Meteorol*. Vol. 32(2), 22-150, 1993.

Turner D. J. W. and Turner D., Attenuation due to rainfall on a 24-km microwave link working at 11, 18 and 36GHz. *Electron. Lett*., vol6, pp297-298, May 14, 1970.

Ulbrich C. W.. A review of the different reflectivity technique of measuring rainfall, In: *IEEE Transactions on Geoscience and Remote Sensing*, vol. GE-24, pp. 955-965, 1986.

Ulbrich C. W.. Natural variations in the analytical form of the raindrop size distribution, In: *J. Clim. Appl. Meteorol.*, 22, pp. 1764-1775, 1983.

Usman I. S., *Development of point to multipoint models for availability and fade mitigation in the millimeter wave frequency range*. Ph.D. dissertation, University of Bath, UK, 2005.

Veneziano D., Furcolo P. and Iacobellis V., Imperfect scaling of time and space-time rainfall, *J. of Hydrology*, 322(1-4), pp. 105-119, 2006.

Veneziano D., Bras R. L. and Niemann J. D., Nonlinearity and self-similarity of rainfall in time and a stochastic model, *J. of Geophys. Res*., vol. 101, no. D21, pp. 26371-26392, Nov. 27, 1996.

Veneziano D., Bras R. L. and Niemann J. D.. Nonlinearity and self-similarity of rainfall in time and a stochastic model. *Journal of Geophys. Research*. Vol. 101, D21, pp26371-26392. Nov. 1996.

Voss R. F., Random fractal forgeries, in *Fundamental Algorithms for Computer Graphics*, editor Earnshaw R. A., NATO ASI Series F, Computer and System Sciences, Vol 17, 1985.

Wainwright J. and Parsons A., The effect of temporal variations in rainfall on the scale dependency in runoff coefficients, *Water Resourc. Res*., 38(12), art no1271, 2002.

Waymire E. C., Gupta V. K., and Rodriguez-Iturbe I., A spectral theory of rainfall intensity at the meso-beta scale, *Water Resour. Res.*, 20, pp1465-1483, 1984.

Wheater H. S., Isham V. S., Onof C., Chandler R. E., Northrop P. J. Guiblin P., Bate S. M., Cox D. and Koutsoyiannis D., *Generation of Spatially Consistent Rainfall Data*, Research Report number 204, department of Statistical Science, University College London, Feb. 2000.

Wheater H. S., Isham V. S., Cox D. R., Chandler R. E., Kakou A., Northrop P.J., Oh L., Onof C. and Rodriguez-Iturbe I.. *Spatial-temporal rainfall fields: modelling and statistical aspects*. 1997.

Willems P., A spatial rainfall generator for small spatial scales, *J. Hydrol*., 252, pp126-144, 2001.

Xu H.. Terrestrial *Radio Wave Propagation at Millimetre-Wave Frequencies*, Dissertation, Virginia Polytechnic Institute and State University, 2000.

Yaglom. A. M., Effect of Fluctuations in Energy Dissipation Rate on the Form of Turbulence Characteristics in the Inertial Subrange, *Dokl. Akad. Nauk SSSR*, 166, pp49-52, 1966.

Zawadski, I.I. Statistical properties of precipitation patterns. *J. Appl. Meteor.*, 12, 459-72., 1973.

Zawadzki I., Statistical properties of precipitation patterns. J.Appl. Meteorology, vol. 12, pp. 459-472, 1973.